2017

A Neuronal Circuit Architecture for Angular Integration in Drosophila

Jonathan Green

A NEURONAL CIRCUIT ARCHITECTURE FOR ANGULAR INTEGRATION IN *DROSOPHILA*

A Thesis Presented to the Faculty of

The Rockefeller University

in Partial Fulfillment of the Requirements for

the degree of Doctor of Philosophy

by

Jonathan Green

June 2017

A NEURONAL CIRCUIT ARCHITECTURE FOR ANGULAR INTEGRATION IN *DROSOPHILA*

Jonathan Green, Ph.D.

The Rockefeller University 2017

While navigating their environment, many animals keep track of their angular heading over time. However, a neuronal-circuit architecture for computing heading remains unknown in any species. In this thesis, I describe a set of neurons in the *Drosophila* central complex whose wiring and physiology provide a means to shift an angular heading estimate when the fly turns. I show that these clockwise- and counterclockwise-*shifting neurons* each exist in two subtypes, with spatiotemporal activity profiles that suggest opposing roles for each subtype at the start and end of a turn. Shifting neurons are required for the heading system to properly track the fly's heading in the dark, and their stimulation induces a shift in the heading signal in the expected direction. I also provide evidence that the angular position of visual landmarks is flexibly associated with the fly's internal heading estimate as it explores its environment. A specific circuit-level model based on known cell types is proposed to account for this flexible association. The central features of the biological circuits described here are analogous to computational models proposed for head-

direction cells in rodents and may inform how neural systems, in general, perform angular calculations.

Acknowledgments

I wish to thank Gaby Maimon, my supervisor, for teaching me most of what I know in neuroscience, for his willingness to grant perhaps unwarranted freedom, and most importantly, for his unwavering support over many years without success. It would be an understatement to say that this project would not have been possible without his guidance.

I wish to thank Atsuko Adachi, who tirelessly dissected, stained and imaged a seemingly endless list of fly brains. All immunohistochemistry experiments, as well as the comprehensive tracing of P-EN neurons, were entirely her work. Atsuko also helped with fly genetics.

I wish to thank Kunal Shah for his skill and patience in fine tuning the fabrication of new fly holders down to the last (50) micron, as well as designing and machining various parts for the experimental rig. Thanks to Pablo Magani, who tested various sphere-tracking methods, and finally discovered and set up FicTrac to operate in closed loop in our system. Thanks to Jonathan Hirokawa for, among many things, developing a pipeline for registering imaging data.

I wish to thank Christoph Kirst, who introduced me to the world of neuronal network models; Vikram Vijayan, who had the initial idea of using Gal4 lines from the Flood et al. 2013 TrpA1 screen as a starting point for a $P2X_2$ screen; and all members of the Maimon Lab for thoughtful discussions and general help over the years.

I wish to thank the members of my committee: Sandy Simon, Cori Bargmann and Vanessa Ruta, for helpful feedback and their support and interest over the years.

Thanks to the Ruta and Rubin labs for fly stocks, and the DiAntonio and Krantz labs for antibodies.

Finally, I wish to thank Saša Jereb, my other half, and my friends and family, for making a lopsided person slightly less lopsided.

Table of Contents

List of Figures

List of Tables

Chapter 1 | Introduction

Animals everywhere are navigating. The arctic tern migrates from the south to the north pole (Egevang et al. 2010), sea turtles swim across the Atlantic Ocean (Fuxjager, Eastwood, and Lohmann 2011), and monarch butterflies fly between Canada and Mexico (Reppert, Gegear, and Merlin 2010). Humbler animals navigate over shorter distances, but with no less importance to their survival. For example, honeybees direct each other towards a source of nectar (von Frisch 1967). After finding food during a meandering outbound search from the nest, ants can walk directly back home (Wehner and Srinivasan 2003). At the heart of each of these complex navigational routes is the basic computation of "where am I heading?". The first step towards a neurobiological understanding of this computation came with the discovery of head direction cells in rats (Taube, Muller, and Ranck 1990a). More recently, evidence for heading-sensitive cells has emerged in other species (Varga and Ritzmann 2016; Heinze and Homberg 2007; Finkelstein et al. 2015), including *Drosophila* (Seelig and Jayaraman 2015) (*heading* is used here to refer more ambiguously to the animal's orientation, without specifying *head* direction or *body* direction, since in some cases – as in when the animal's head and body are tethered - the two cannot be distinguished). However, the neuronal mechanisms that build these heading signals remain unknown in any species. This thesis characterizes how a neuronal circuit in the fruit fly, *Drosophila melanogaster,* computes the fly's heading.

To frame these results within the broader context of spatial navigation, I first review the behavioral evidence for the existence of an internal sense of heading and space in animals. Second, I review the physiology of neuronal systems that respond specifically to navigational variables, including head-direction. Finally, I review the neural network models that have been proposed to explain how the physiological properties of head-direction cells and other spatially-responsive neurons are constructed from more basic inputs.

Behavioral evidence for spatial navigation in animals

We first consider the behavioral evidence for animals having a sense of heading (i.e. an internal representation of one's heading in the world) and a sense of 2D space (i.e. an internal representation of one's location in the world) and, if so, how these senses might be used during spatial navigation.

It is instructive to first note what sorts of navigational behaviors do not require an explicit sense of heading or space, as described above. One can travel in specific directions and end up in specific locations without storing any explicit information related to which way one is heading or where one is located in 2D space. For example, a bacterium can navigate towards higher concentrations of a nutrient by changing its rate of turning, such that the bacterium makes fewer turns when the nutrient concentration increases over time (Berg and Brown 1972). What is stored in the bacterium is the change in the concentration of the nutrient over *time* (the last few seconds) (Block, Segall, and

Berg 1982), rather than an internal map of the concentrations of nutrients over space. Larger cells and organisms can navigate gradients by also measuring concentration changes over *space*, by comparing concentration differences across their length (Swaney, Huang, and Devreotes 2010). These cells, however, also do not maintain any internal record of their heading or position in space, but rather navigate by always measuring the direction in which higher concentrations are present in their immediate vicinity. Thus, an organism's ability to statistically move in a specific direction (e.g. towards increasing nutrient concentrations) or even to a specific position (e.g. to the location with maximum nutrient concentration) is not necessarily evidence for an explicit internal sense of heading or 2D space.

In contrast to chemotaxis, the ability to navigate certain types of mazes is more likely to require a sense of heading or space, as in the maze learning example in Figure 1.1 (Tolman, Ritchie, and Kalish 1946). Rats were trained to find food at the end of the training maze in Figure 1.1a. After starting at point A, the rats had to enter the circular arena, and then navigate through the indirect path shown towards the food box at point G. Rats learned to reliably run to the food box along the only available path after several training sessions. After training, the rats were placed in the test maze in Figure 1.1b. In this test maze, the initial path that led to the food box was purposefully blocked. In addition, 18 new paths exited radially from the circular arena, without leading to any food. The trained rats were placed at the usual starting point A and their behavior was

monitored. The rats ran straight ahead into the original arm that would have led them to the food box in the training maze. After hitting the road block, the rats returned to the circular arena and started to explore different options. After exploring for some time, the rats eventually committed to follow one of the radial paths to its end, after which the trial was ended. The distribution of rats choosing each radial path is shown in Figure 1.1c, and is re-plotted in polar coordinates in Figure 1.1d. The rats chose path #6 most commonly. This path is highlighted with the red arrow in Figure 1.1b-d, and corresponds to the path pointing directly towards the original food box in the training maze.

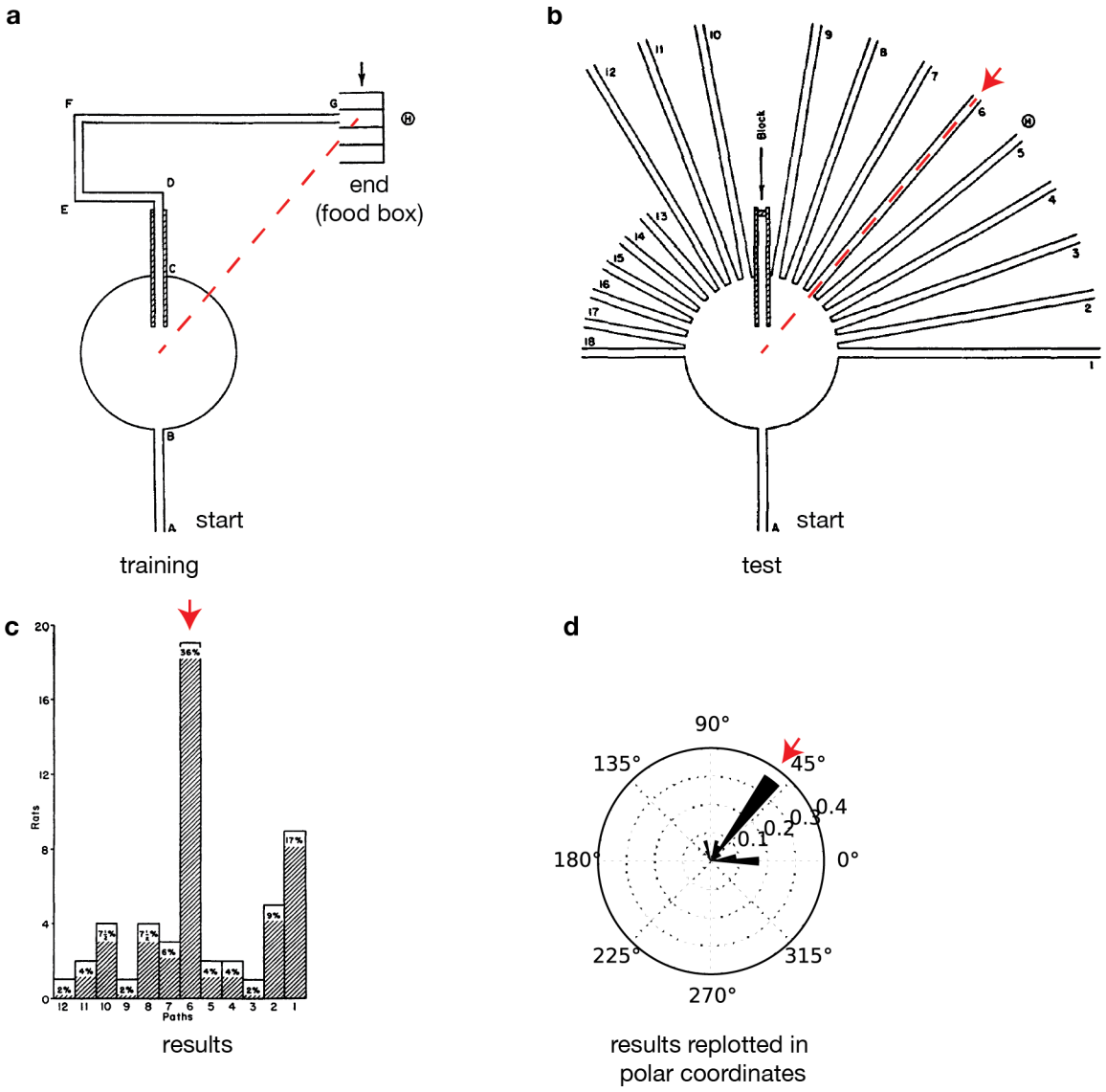

Figure 1.1 | Rats flexibly navigate towards their goal.

a, Training maze in which rats were trained for 4 days to reach the food box (G) after starting from the bottom of the maze (A). **b**, Test maze in which rats were tested on the 5th day. Rats were placed at the bottom of the maze (A) and allowed to enter the alley that would normally lead them to the food box (CD in **a**). Since this alley was blocked, the rats returned to the main chamber and then chose an alternative alley, after which the trial was ended. The dotted red line in **a** and **b** was added as a visual aid to highlight the best path. **c**, Distribution of alternative alleys chosen in the test trial. Numbered paths on the x-axis correspond to the alleys in **b**. **d**, Data in **c** replotted in circular coordinates. The red arrows in **b-d** highlight the same "best" path in each representation of the maze. Adapted from Tolman et al. 1946.

This experiment provided evidence for an abstract, internal sense of heading and space. In contrast to the chemotaxis example, the rat could not directly sense its target (e.g. the food) in the test maze (indeed it was not even present) and therefore could not find it by navigating a gradient (e.g. by following increasing food odor concentrations). The rat also could not memorize a series of associations between sensory inputs and navigational decisions for each point along the maze, since it had to execute an alternate path (with new sensory inputs) for the first time in the test maze. In addition, the choice of which alternate path to take required the rat to store spatial relationships in its environment. These results strongly suggested that the rat had to store its current position, the position of its target, the heading angle that would achieve the shortest path between these two positions, and its current heading angle. The rat would then be able to determine the shortest path that pointed most directly towards its target.

The maze learning example also highlights the advantages of having a sense of heading and 2D space. Indeed, if chemotaxis is such a successful method for navigating gradients, why would one need a sense of space in the first place? The first reason is that a sense of space endows an organism with a memory of how to reach a target that cannot be directly sensed (for example, if a pizza shop is too far away to see or smell). The rat does not immediately sense the food in Figure 1.1, and must therefore remember the location of the food to

navigate towards it. The rat would not be able to accomplish this task if it were relying solely on chemotaxis (indeed the food is absent in Figure 1.1b). A second reason is that a sense of space is more flexible in that, by building a map, one can use many more environmental cues along with their spatial relationships to successfully navigate towards one's target, even if those environmental cues are not of any interest in themselves. For example, one might use landmarks to help orient one towards a target (for example, the 66th street and 1st Ave street signs), even if the landmarks themselves are not intrinsically rewarding, or even near the target. A sense of space is also flexible in that one can use spatial relationships in order to execute alternative paths to reach the same goal. For example, if a barrier is placed in between one's current position and one's target position (as in Figure 1.1b), a sense of space provides flexibility in choosing alternative routes that will still lead to the same target destination.

The maze learning example in Figure 1.1 also highlights one framework for how a sense of angular heading might be used; the rat likely used its sense of heading to choose the path that pointed towards a previously visited location. This maze learning example is also somewhat complicated in that the rats needed to have a sense of their position, as well as their target location, in 2D space, from which they could extract the angular heading to optimally reach their destination. A second framework for how a sense of heading might be used is for an animal to simply navigate in a specific direction – i.e., keep a fixed bearing relative to a distant landmark like the sun for many minutes or hours. In this case,

the animal matches its *current* internal sense of heading with its *desired* heading angle, without requiring any knowledge of where it is located in 2D space. Animals might keep a fixed bearing for extended periods when navigating to a 2D target location for the first time, like a migratory animal performing its first migration. It may be that a sense of 2D space is used in this scenario, and that the target location is innately stored in a spatial map from birth, guiding a fixed bearing trajectory from the starting location. On the other hand, the animal may simply have an innate target angle that it wishes to travel in rather than a 2D goal location that it aims to reach. As an example, newborn loggerhead turtles migrate across the North Atlantic Ocean. These newborn turtles orient in response to experimentally-induced magnetic fields in a direction that is consistent with the direction the turtle would take given the magnetic field at each point along its route (Fuxjager, Eastwood, and Lohmann 2011). A second example is the migration of newborn monarch butterflies, which migrate from Canada to Mexico each fall. Newly eclosed monarch butterflies normally migrate in a southwesterly direction from eastern Canada to Mexico. If these butterflies are displaced to western Canada, they still navigate southwest, even though their new starting location would require them to travel in a southeasterly direction (Mouritsen et al. 2013). In these cases, navigation might require a sense of heading, but not necessarily a sense of 2D space.

It is interesting to consider from an evolutionary standpoint whether a sense of heading and a sense of 2D space evolved together, or if one came first.

One might expect that a sense of heading is more primitive, since a sense of heading is more directly tied to the immediate behavioral decision of which direction to go in at every point along a trajectory. A sense of space, on the other hand, is one additional step removed from immediate behavioral decisions because the direction in which the animal should head must be calculated from information about one's current position and one's target position. Indeed, a sense of 2D space might have no use without a sense of heading, whereas the converse is not necessarily true, as the migratory examples above might indicate. A sense of space might then be built in addition to a sense of heading to endow an animal with greater flexibility in navigating its environment. Empirically, however, it is not known (to my knowledge), whether any animal has a sense of heading without also having a sense of space.

In this thesis, I will discuss how a sense of heading is computed in the fruit fly, *Drosophila melanogaster*. The navigational capabilities of this species have, unfortunately, been less well documented. One of the best examples, in a laboratory setting, was the demonstration that freely walking flies can find a cold spot in an otherwise hot arena by making use of panoramic visual cues (Ofstad, Zuker, and Reiser 2011). After 10 training trials, flies reliably walk along directed trajectories towards the cold spot by making use of its fixed location in reference to the visual environment. If flies perform this task using a similar algorithm to the one described above for Figure 1.1, then this would suggest that flies have a sense of heading that they use to direct themselves towards their target.

Interestingly, this task requires a class of neurons that innervate the ellipsoid body, a donut-shaped structure at the center of the fly brain, and the same structure found to be involved in tracking the fly's heading in this work (see Chapter 3, page 43) and in a recent study (Seelig and Jayaraman 2015). A second example that points to the existence of an internal sense of heading in flies is in a task where the fly was shown to be able to navigate towards the position of a landmark that had recently disappeared (Strauss and Pichler 1998). In this task, a freely walking fly is placed in a circular arena with two vertical stripes displayed 180º apart on a panoramic, cylindrical display (one at 0º and one at 180º). The fly tends to be attracted to the vertical stripes and walks back and forth between the two (after reaching one stripe, the fly turns around and walks back towards the other stripe, and so on). During the middle of the fly's trajectory between the two stripes, say as it moves from 0º to 180º, the two original stripes are removed, and a new stripe is displayed at 90º for a few seconds. The fly becomes temporarily attracted to the new stripe at 90º and turns in its direction until the 90º stripe disappears, a few seconds into the fly's trajectory toward it. After the 90º stripe disappears, the fly is left with no visual landmarks, but nevertheless tends to resume its original trajectory (or at least makes a directed turn) towards where the original 180º stripe was displayed. Since the arena contains no visual cues to guide the turn toward the original stripe, this result implies that the fly had a memory of which way to go. Interestingly, flies cannot effectively perform this task if one silences the same

class of neurons that innervate the ellipsoid body and are essential for the heat maze task described above (Neuser et al. 2008).

The physiology of heading- and position-sensitive neurons

Whereas behavioral experiments have suggested a sense of 2D space and heading in a wide variety of animals, neurophysiological experiments have provided more direct evidence for such navigational systems in the brains of several species. Here I focus on the neurophysiology of rodent navigational systems, since these are the best studied at the neural level. I also highlight some studies in insects to provide a context for the work presented in this thesis.

Heading-sensitive neurons

In 1984, James Ranck provided the first neurophysiological evidence for a sense of heading with the discovery of head-direction cells in the rat postsubiculum (Ranck 1984). These initial observations were then followed up quantitatively by Jeffrey Taube (Taube, Muller, and Ranck 1990b; Taube, Muller, and Ranck 1990a) working in Ranck's laboratory. Head-direction cells are aptly named: each cell fires maximally when the rat's head points in a specific direction (called the cell's *preferred direction*). This head direction response is quite specific: it is minimally affected by the animal's movements, its body orientation or its position in space (Taube, Muller, and Ranck 1990a). Different head-

direction cells fire maximally at different head directions, and are roughly equally distributed across head directions (Taube, Muller, and Ranck 1990a).

Through systematic environmental perturbations, Ranck and colleagues demonstrated that the head-direction signal, while influenced by sensory inputs, is not a sensory signal itself, but rather reflects an abstract head-direction signal built from sensory inputs and internal calculations. First, the head-direction signal is strongly influenced by visual cues. If a rat is placed in a cylindrical arena with a single cue card and the card is rotated by 180º (the rat is temporarily removed from the arena during this rotation), then the preferred direction of head-direction cells also rotates by 180º. When the cue is rotated back to its original position, the preferred direction of head-direction cells also rotates back to its original position. Furthermore, the preferred direction vectors for a given head direction cell are parallel for different positions in the arena, and do not converge towards a single point in space, indicating that these cells do not track the orientation of an object relative to the rat's head, but rather the rat's head's allocentric orientation in the world (Taube, Muller, and Ranck 1990a). Second, when the lights are turned off, the head-direction signal persists and continues to integrate the animal's movements in the dark (McNaughton and Chen 1991; Mizumori and Williams 1993). The cell's directional response (i.e. its ability to fire when the head points in a particular direction) tends to degrade over several minutes in the dark, as expected if the rat's internal sense of head direction drifts relative to its actual head direction in the world (Mizumori and Williams 1993). Moreover, the

head direction signal is abolished (even when the lights are turned on) if the vestibular system is impaired (Muir et al. 2009; Stackman and Taube 1997), indicating a strong dependence of the head direction signal on the rat's ability to sense head rotations. That head-direction cells continue to fire and integrate the rat's head rotations in complete darkness suggests that these cells' directional properties are primarily driven by an intrinsic network property that integrates the rat's head movements rather than being a direct function of sensory signals, since the rat has no external directional cues to use when the lights are off. (The only other directional signal remaining is the earth's magnetic field, but head direction cells do not follow a consistent north-south coordinate system when a rat is moved to a different room (Mizumori and Williams 1993).) Visual landmarks, when available, likely play a role in correcting for accumulating errors in the angular integration process driven by this intrinsic network.

Head-direction cells as a population operate within the same frame of reference. For example, the preferred directions of two head direction cells recorded simultaneously rotate together by the same amount if a cue is rotated by 180^{o}, or if the cue is removed and the preferred firing directions reset to a different reference angle (Taube, Muller, and Ranck 1990b). These results indicate that the relative offset between the preferred directions of different head direction cells is maintained across environments – an important property when considering the underlying circuit mechanism for generating the head direction signal.

Head direction cells are found across multiple regions in the mammalian brain, including the postsubiculum, where they were originally discovered (Ranck 1984; Taube, Muller, and Ranck 1990a), the entorhinal cortex, the anterodorsal thalamic nucleus (ADN) and the lateral mammillary nucleus (LMN), among others (Taube 2007). The head direction cells in each of these areas are not identical, with different peak firing rates and tuning curve shapes (Taube 2007). Notably, the head-direction cells in the lateral mammillary nucleus (LMN) show modulations of their head-direction signal as a function of the rat's angular head velocity, with cells in the left and right hemispheres being modulated in opposite directions for clockwise and counterclockwise rotations of the head (Stackman and Taube 1998; Blair, Cho, and Sharp 1998). These LMN cells may be particularly important in combining angular head velocity and head direction signals to integrate the rat's head direction over time. Indeed, if the LMN is lesioned, the head-direction signal in the ADN is abolished (Blair, Cho, and Sharp 1998). In turn, if the ADN is lesioned, the head-direction signal in the postsubiculum is abolished (Goodridge and Taube 1997). If the postsubiculum is lesioned, however, the head-direction signal in the ADN remains largely intact (Goodridge and Taube 1997). These sequential lesion effects are consistent with the general flow of anatomical projections from the LMN → ADN → postsubiculum (Taube 2007), and with the generation of the head-direction signal being upstream in this pathway, particularly in the LMN, where head-direction and angular head velocity signals are carried in the same cell (Taube 2007). It is

important to note, however, that lesioning the postsubiculum and other areas did produce some milder impairments in the properties of ADN head direction cells. For example, the ADN head direction cells no longer rotated with a cue by the correct amount if the postsubiculum was lesioned (Goodridge and Taube 1997), indicating that the postsubiculum might play a role in landmark orientation. Although not comprehensive, these results suggest that different properties of the head direction signal are generated in different brain regions.

Position-sensitive neurons

Although the work in this thesis focuses on heading-sensitive neurons, I also wish to highlight the properties of position-sensitive neurons in rodents, in particular grid cells, because (1) head-direction cells share some physiological properties with grid cells, suggesting that similar circuit mechanisms might generate both signals in one- and two-dimensions, respectively, and (2) one function of head-direction cells may be to aid in building the activity profiles of grid cells.

In 1971, John O'Keefe and Jonathan Dostrovsky provided the first neurophysiological evidence for a sense of space with the discovery of *place cells* in the rat hippocampus (O'Keefe and Dostrovsky 1971). Place cells fire when the rat occupies specific locations (typically one, or a few) within an experimental arena. Hippocampal place cells are also modulated by other factors, including non-spatial stimuli and the animal's own behavior (M.-B. Moser,

Rowland, and Moser 2015). The hippocampus receives major inputs from the lateral entorhinal cortex (LEC) and the medial entorhinal cortex (MEC) (Witter et al. 1989; Lavenex and Amaral 2000; Oh et al. 2014). Whereas cells in the LEC are only weakly spatially responsive (Hargreaves et al. 2005), some cells in the MEC respond to the rat's location as strongly as hippocampal place cells (Fyhn et al. 2004). One type of spatially-responsive MEC cell, the *grid cell*, responds periodically at multiple locations in a hexagonal grid over space (Hafting et al. 2005). (A second type, not discussed further here, is the border cell, which fires when the animal is close to a wall (Solstad et al. 2008).) Grid cells are organized into discrete modules, with each module increasing in grid scale (the spacing between firing peaks) by a factor of ~1.4 going from the dorsal to ventral MEC (Stensola et al. 2012). Whereas the location of the rat is ambiguous for a given grid cell, it can be unambiguously defined if the entire grid cell system is considered as a whole for sufficiently small environments (Rowland, Roudi, and Moser 2016).

Like head direction cells, the spatial firing patterns of place cells and grid cells rotate with a landmark cue (Bostock, Muller, and Kubie 1991; Hafting et al. 2005). Also like head direction cells, grid cells from the same module maintain their spatial firing patterns relative to each other when the rat is placed in a new environment, even though the spatial phase or orientation of the grid may change relative to the borders of the arena (Fyhn et al. 2007; Stensola et al. 2012). Place cells, however, do not preserve their spatial firing patterns relative to each other

across environments, a process known as remapping (Muller and Kubie 1987; Leutgeb et al. 2005). Indeed, a place cell that fired in one environment may not even fire in the next (Leutgeb et al. 2005). These results show that, like head direction cells, all grid cells within the same module shift or rotate by the same amount, whereas this is not true of place cells.

Although grid cells were discovered in the medial entorhinal cortex (MEC), and head direction cells were discovered in the postsubiculum, these two cell types are now known to be anatomically intermingled in these regions. Head direction cells are also present in deeper layers of the MEC (Sargolini et al. 2006), and grid cells are also present in the dorsal pre- and para-subiculum (Boccara et al. 2010) (confusingly, the dorsal pre-subiculum is also called the postsubiculum in Taube et al. 1990 based on anatomical characterizations by van Groen and Wyss 1990). Moreover, cells that respond to the rat's speed, called *speed cells*, were also recently identified as a fourth cell type (after including border cells). That these cell types are anatomically intermingled is consistent with the possibility that head direction and speed cells contribute to generating grid cells, by integrating the animal's direction and speed (i.e. its 2D velocity vector) to calculate its current position. It is also worth noting that head-direction cells do not necessarily encode the rat's direction of travel, which can differ from the rat's head direction. This discrepancy would somehow have to be resolved if this head direction signal is used to properly integrate the rat's position in space.

Although many studies have focused on the role of the hippocampus and medial entorhinal cortex in spatial navigation, other studies have argued that these structures play a role in memory more generally, with spatial variables (i.e. one's location) being one of many components in these memories (Eichenbaum and Cohen 2014). For example, patient HM, whose hippocampus and medial temporal lobe were surgically removed, could not remember spatial as well as non-spatial facts or events beyond several minutes (Squire, Stark, and Clark 2004; Eichenbaum and Cohen 2014). Moreover, in rats, place cells in the hippocampus and grid cells in medial entorhinal cortex can also map to non-spatial variables like sound frequencies (Aronov, Nevers, and Tank 2017). These studies, among others (Eichenbaum and Cohen 2014), suggest that the hippocampus and entorhinal cortex are involved in multiple processes, including, but not exclusive to, spatial navigation.

Orientation maps in insects

Well before the work I will describe in this thesis, some indirect neurophysiological evidence existed that insects might carry a heading signal. These lines of evidence centered around the fact that many insects sense polarized light to aid in their navigation. Because light scatters with a predictable polarization angle as a function of the angle at which it hits the atmosphere, the pattern of polarized light across the blue sky is yoked to the sun in a systematic fashion and thus this celestial cue can act as a proxy for the position of the sun

(when the sun is obscured by clouds, for example). Many insects use the pattern of polarized light in the sky as an absolute reference signal to estimate their orientation in relation to the sun (Rossel and Wehner 1982). For example, ants and bees use the sky's pattern of polarized light as a compass cue to help direct them back to their nest or hive after finding food (Wehner 1989). Neurons that respond to polarized light, with a tuning curve that peaks at a specific polarization angle, were discovered and characterized in insects (Homberg et al. 2011), with a focus on locusts (Homberg 2004). These polarization-sensitive neurons form a pathway from the dorsal rim of the eye (which contains photoreceptors specialized to detect polarized light) to the central complex, a group of central neuropil conserved across insect brains (Homberg 2008), also see Chapter 2. The key finding was that polarization-sensitive neurons innervate one component of the central complex, the protocerebral bridge (or *bridge)*, in such a way that neurons with similar preferred polarization angles were near each other in the bridge and the preferred angle rotated systematically as one moved across the structure from left to right.(Heinze and Homberg 2007). The sequential ordering of different polarization-orientation sensitivities across the bridge suggested that when the insect was oriented in one direction, a certain pattern of activity would exist in the bridge and this activity pattern would slide around the bridge when the animal turned clockwise or counterclockwise in the world, thus forming some sort of mapping between the activity of the bridge and the animal's orientation in the world. These studies, however, only involved measuring polarized-light tuning

curves in identified cells in non-behaving locusts; the authors could not measure neurophysiological responses in the bridge in behaving locusts due to experimental limitations, which meant that the activity of neurons during an actual navigational task could only be indirectly inferred.

More recently (during the course of my thesis), Seelig and Jayaraman 2015 showed that the activity in a set of cells that tile the ellipsoid body (and other structures) in the fly central complex (see Figure 3.1 page 46) collectively tracks the fly's orientation as it walks on a ball in a virtual environment (Seelig and Jayaraman 2015). The properties of these neurons closely resemble those of head direction cells in mammals in that the ellipsoid body heading signal is updated by the angular position of visual cues, but it also persists in complete darkness, where its angular value must be updated by integrating the fly's clockwise and counterclockwise turns. The interaction between these cells and a second heading-related cell type described in this thesis is the subject of Chapter 3.

Neuronal models for building a heading and position signal

One year after the publication of head direction cells in 1990 (Taube, Muller, and Ranck 1990a), McNaughton et al. proposed the first circuit mechanism for a sense of heading based on these neurophysiological results (McNaughton and Chen 1991). This model was then refined in Skaggs et al. into

the predominant model for head direction cells in the field to this day (Skaggs et al. 1995).

In this model, head direction cells are arranged in a circular circuit as in Figure 1.2. Head direction cells excite each other locally and inhibit each other distally (i.e. everywhere else) along the ring. These two features produce a single activity peak along the ring, given properly tuned synaptic weights. Within a certain range of synaptic weight parameters, at least one activity peak is guaranteed to exist because recurrent local excitation produces a positive feedback loop that continues to increase the strength of a local activity peak that starts out very weak. On the other hand, only one peak is stable because two or more peaks will compete via their distal inhibitory interactions until one peak wins and inhibits all the others.

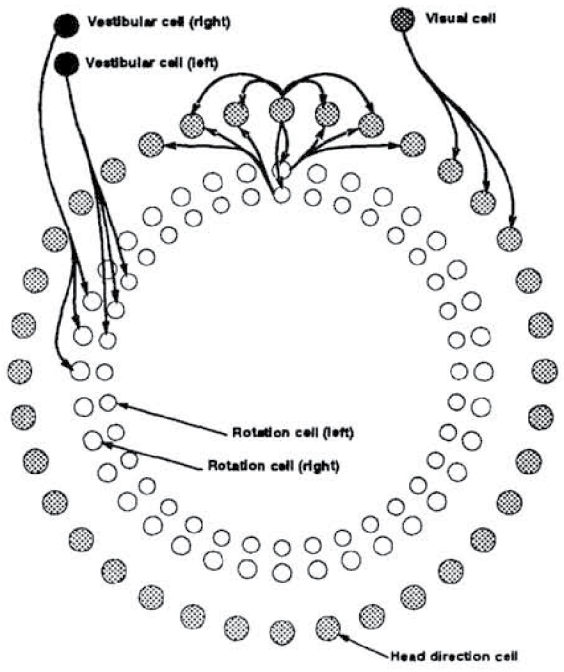

Figure 1.2 l Neuronal model proposed for head direction cells in Skaggs et al. 1995.

See text for a description of the model.

To rotate the activity peak around the ring as a function of the animal's turning behavior, a set of rotation neurons is added: two for each head-direction cell in the ring. One rotation cell projects clockwise, and the other projects counterclockwise to excite the neighboring head direction cells in the ring. Rotation cells in turn receive two inputs: one is an excitatory input from head direction cells, the second is an excitatory input from a third cell type that senses the animal's turning velocity, called vestibular neurons in Figure 1.2. These vestibular neurons come in two subtypes: one is active when the animal turns

right, and the other is active when the animal turns left. The “right turn” vestibular neuron excites all clockwise-projecting rotation neurons and the “left turn” vestibular neuron excites all counterclockwise-projecting rotation neurons. In this way, all clockwise-projecting rotation neurons receive excitatory inputs when the animal turns right, whereas counterclockwise-projecting rotation neurons receive excitatory inputs when the animal turns left. A given rotation cell, however, only *fires* if it receives inputs from both a head direction cell and a vestibular cell. The result of this interaction is that when the animal turns right while its head direction cells are maximally active at 0º along the ring, the only rotation cells that *fire* are those projecting from 0º in the ring in the clockwise direction (although all clockwise-projecting rotation neurons receive excitatory inputs from the vestibular cells, these inputs, without the added input from the head-direction cells, are not strong enough to trigger action potentials). The rotation cells near 0˚ excite the head direction cells at +10º along the ring. Through the same inhibitory interactions that produce a single activity peak (see description above), the head direction cells at 10º inhibit the head direction cells at 0º, maintaining the width of the head direction cell activity peak along the ring such that the activity peak *shifts* clockwise rather than simply expanding in the clockwise direction. Finally, the head direction cells at +10º now excite the rotation cells at +10º, while the now inactive head direction cells at 0º no longer excite the rotation cells at 0º, returning the system to its original state, except shifted 10º clockwise. The same process of rotating the activity peak along the ring can then continue from its

current position, given the current angular velocity of the animal's head, as signaled by the vestibular neurons. This neuronal model for angular integration is further discussed in Chapter 3.

A key feature of this circuit is that its inputs, in the form of the vestibular neurons, hold no information concerning the animal's head direction – only its angular head *velocity*. The animal's current head direction is then computed using the internal dynamics of the circuitry, as described above. A second important point is that, the "vestibular neurons" may be better thought of as signaling the animal's angular head velocity through many sensory modalities or internal signals including, but not exclusive to, vestibular signals, proprioceptive signals from the animal's legs, efference copy signals of the animal's motor command to turn, and visual motion cues informative on the rate of rotation of the animal. Regardless of their origin, these signals can be combined into one "angular head velocity" signal that is then mathematically integrated into the animal's current head position. A third point is that this model is susceptible to noise in that fluctuations in the balance between clockwise- and counterclockwise-projecting neurons tends to lead to drift in the head direction signal. While important, this concern is not specific to this model, since any integration process will lead to drift if there is noise in the system. How this drift might be mitigated is further discussed in Chapter 3, page 89. When it is not pitch black, one way to correct for drift is to use visual landmarks as absolute

reference points to anchor the system's orientation estimate, which I discuss next.

It is also known that head direction cells can make use of landmarks in the environment (such as a cue card in the head direction experiments described above) as reference points to correct errors made by the angular integration process. To implement this property in the model, Skaggs et al. 1995 introduce a fifth class of neurons, called visual feature detectors, or visual cells in Figure 1.2 (Skaggs et al. 1995). These visual cells were hypothesized to respond to specific visual features (like a small oriented edge) at specific retinal positions. Different visual cells were hypothesized to respond to different azimuthal positions of a given feature, or to different visual features. Each single visual cell was proposed to have weak synaptic connections to every head direction cell in the ring, with the key property that these weak connections increase in strength as a function of coincident activity between the visual cell and downstream head direction cells. This learning rule has the following effect. Suppose that a landmark is very far away, such that every time the animal's head points North, the landmark appears at the same position on the animal's retina, and the same "landmark" detector is active. Other "landmark" detectors are active when the animal's head points northeast, east, etc. Looking at the animals' compass, the same head direction cells are also active whenever the animal's head points North, at least for some time before errors in the angular integration process begin to accumulate. During this process, connections between this specific landmark

detector visual cell and “North” encoding head direction cells potentiate relative to the connections between the same visual cell and other head direction cells because the North head-direction cells tend to be coactive with this visual neuron. Similarly, other detector cells that respond to the same landmark at other retinal positions become associated with other head direction cells around the ring. In this way, the system can learn the positions of static landmarks to correct for errors in angular integration over time. This model also has the useful property that if an object is not static, for example if the object is another animal that moves around, the feature detectors that recognize that object will not associate with any head direction cell because the two are not co-active enough. The system would thus pick out only static landmarks – which are useful for orienting the heading signal – to associate with the head-direction cells. How a landmark association process of this sort might take place in the fly brain is discussed in Chapter 4 (page 106).

Chapter 2 | Identifying turning-related neurons

This project started with the goal of identifying neurons whose activity could be clearly linked to a behavior (broadly defined, at the outset), which I could reliably observe in tethered flies. I constrained myself to behaviors exhibited on a tether because I knew that such behaviors may allow me to ultimately record the activity of identified neurons while the behavior unfolded (Maimon, Straw, and Dickinson 2010; Seelig et al. 2010). Specifically, I performed a screen for cells that, when experimentally activated, would elicit a reproducible action or sequence of actions from the fly. To repeatedly access the same neurons from fly to fly, I stimulated genetically-defined neurons by expressing the ATP-gated cation channel $P2X_2$ (Zemelman et al. 2003; Ruta et al. 2010) under the control of different Gal4 driver lines and applying ATP through a pipette on the neurites of the relevant cells while the fly was tethered and walking on a floating, air supported ball (see Methods). These initial walking experiments were performed without tracking the ball; we added the ability to perform real-time ball tracking in later experiments in Chapter 3. Because this screening method is low-throughput and labor intensive, I only tested Gal4 lines that had already produced an effect in freely walking flies in a previously published screen of 835 Gal4 lines from the NP collection (Hayashi et al. 2002) that used the cold-activated TRPM8 channel and the heat-activated TrpA1 channel to stimulate neurons (Flood et al. 2013). The ATP-$P2X_2$ screen was not simply a repeat of the TRPM8/TrpA1 screen because by applying ATP to specific

neuropils (rather than heating or cooling the whole animal), (1) I could activate specific subsets of neurons within Gal4 lines that drove expression promiscuously, in many different cell classes, thus potentially identifying which specific neurons were actually driving the behavior, (2) I could activate neurons on one side of the brain and (3) I could ensure that the stimulated behavior was measurable in tethered flies.

Although the initial search was broad in that I was open to studying a wide range of behaviors, I was particularly interested in finding neurons whose activation would lead to turning left or right, since this behavior could be reasonably tied to spatial navigation in freely moving insects. I got lucky. Of the 30 Gal4 lines that I screened, I found two that elicited behavioral effects: one line reliably elicited abdomen bending (NP0351-Gal4), and one line reliably elicited turning (NP0212-Gal4). The characterization of this turn-inducing line (NP0212-Gal4) is the focus of this chapter, and the specific subset of cells that I stimulated in this line are the major focus of this thesis (Chapter 3). The data presented in this chapter are anecdotal because my goal is to simply describe the path by which I arrived to studying the cells of interest. I characterize the function of these neurons more rigorously and comprehensively in Chapter 3.

Anatomy of NP0212 expression

NP0212-Gal4 drives strong expression in a set of neurons that innervate the central complex, a group of centrally located structures that span the midline

in insect brains (Figure 2.2a-c). The NP0212-driven neurons that I stimulated specifically innervate three of these structures: the protocerebral bridge, the ellipsoid body, and noduli (Figure 2.2d-f). These neurons are called P-ENs, with each letter in the three-letter acronym representing one structure that these cells innervate in the central complex. P-ENs are the focus of this chapter and Chapter 3. Other neurons in the NP0212 Gal4 line also innervate a fourth central complex structure, the fan-shaped body. NP0212-Gal4 also drives expression in many other neurons in the brain and thoracic ganglion.

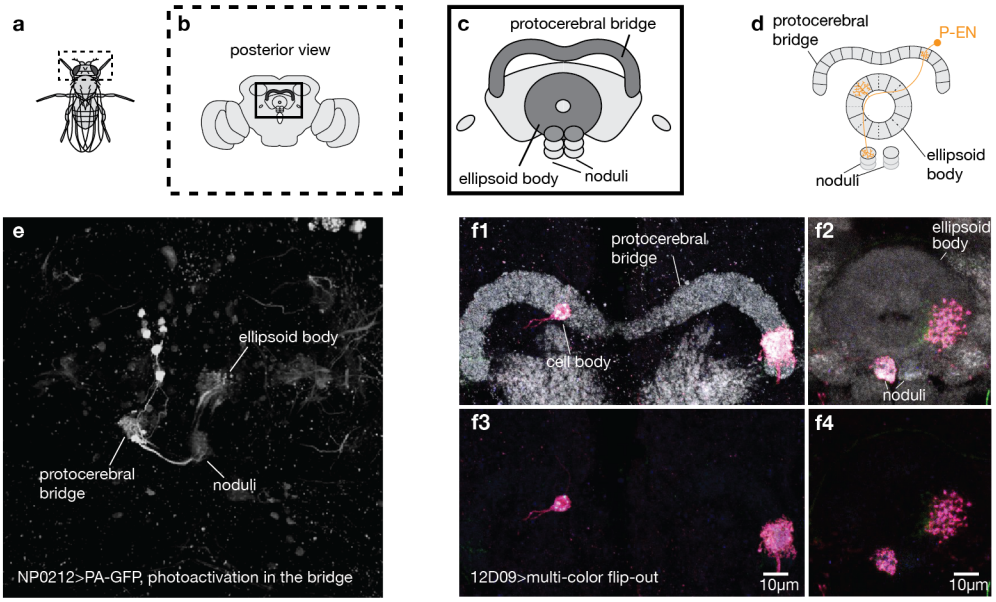

Figure 2.1 | P-ENs are a main component of NP0212-labeled neurons in the protocerebral bridge.

a, Schematic of a fly. **b**, Posterior view of fly brain, enlarged from the dotted rectangle in **a**. **c**, Central complex, enlarged from the solid rectangle in **b**. The protocerebral bridge, ellipsoid body and noduli are highlighted in dark grey. **d**, Schematic of a P-EN neuron, the main component of NP0212-labeled neurons in the protocerebral bridge. P-EN stands for protocerebral bridge, ellipsoid body and noduli. **e**, Maximum z-projection of central brain in which PA-GFP driven by NP0212 was photoactivated in 1-2 glomeruli in the protocerebral bridge. The protocerebral bridge-innervating neurons in NP0212-Gal4 also innervate the ellipsoid body and the noduli. **f**, Labeling of 1-2 P-EN neurons with the multicolor flipout method (pink, see Methods) and neuropil (grey) highlighting the protocerebral bridge, ellipsoid body and noduli. P-ENs are labeled from a different Gal4 line (12D09-Gal4). Gal4 lines other than NP0212-Gal4 (like 12D09-Gal4) that are selective for P-ENs in the bridge and ellipsoid body are used in Chapter 3.

Stimulating one side of the bridge in NP0212 elicits a turn towards the opposite side

In my first experiments, I stimulated the left or right protocerebral bridge in NP0212 as the fly was walking on a ball (Figure 2.2a-f, see Methods). When I stimulated the left side of the protocerebral bridge, the fly turned to the right on the ball, and vice versa when I stimulated the right side of the bridge (Figure 2.2e-f). To test whether this turning was due to a motor program that was specifically tied to the legs, I repeated the experiment in a flying fly (see Methods). Again, when I stimulated the left protocerebral bridge, the fly turned to the right as it was flying, and vice versa when I stimulated the right bridge (Figure 2.2g-k). Since the NP0212 driver line induced Gal4 expression in several neuron classes in the bridge, it was formally possible that activating one set of neurons drove turning while walking and activating a different set of neurons drove turning while flying. However, under the parsimonious assumption that the same neurons elicited the same sign of turning under two completely different modes of locomotion, then the underlying neurons could drive turning independent of the specifics of the motor program (i.e., flying vs. walking). In principle, activating a sensory percept could have driven a common turning response in both flight and walking, but these neurons were located at the center of the fly brain, several synapses removed from any primary sense organ, suggesting that the activated neurons may not be pure sensory neurons. I reasoned, therefore, that these cells might be involved in some abstract process related to spatial navigation.

Discovering an abstract, internal system related to spatial navigation was particularly interesting because animals across phyla navigate using completely different modes of locomotion (e.g., walking, flying, swimming, crawling, etc.), but internal calculations related to one's orientation might have more shared features across animals and might therefore be of broader interest to the neurobiological community, beyond the study of *Drosophila*.

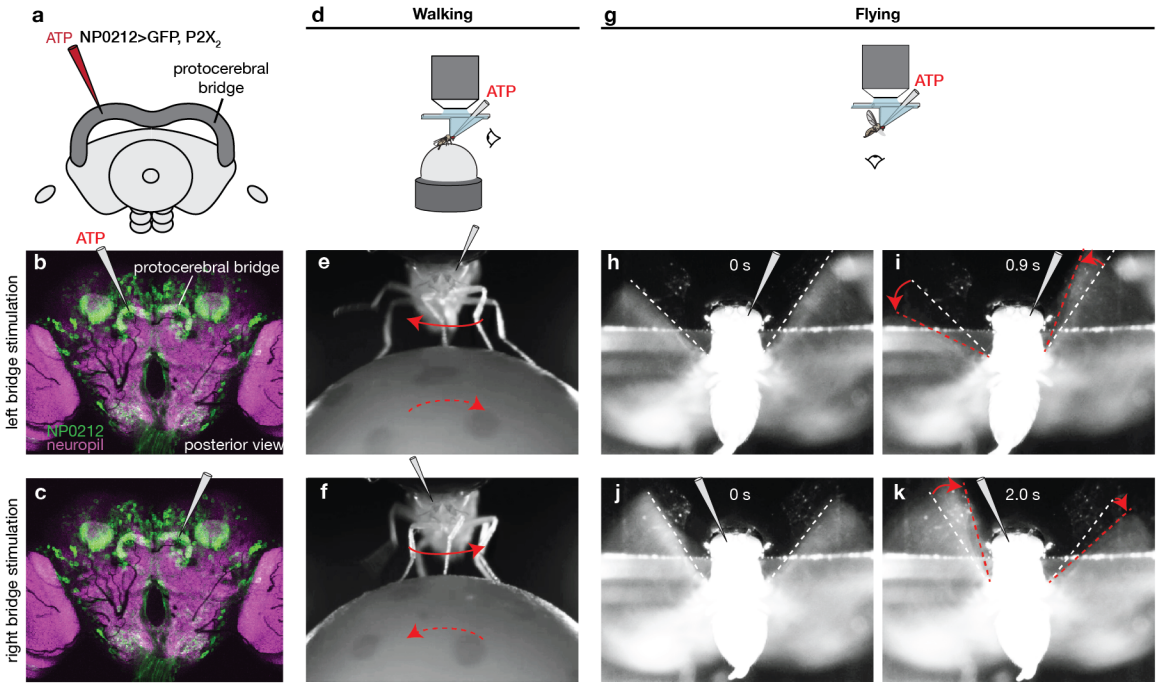

Figure 2.2 | Finding turning-related neurons through a stimulation screen.

a, Schematic of central complex with stimulation pipette. **b**, Posterior view of NP0212>mCD8-GFP brain with schematized stimulation pipette in the left protocerebral bridge. GFP is in green. Neuropil is in magenta. **c**, Same as **b**, for stimulation of the right protocerebral bridge. **d**, Schematic of stimulating neurons in a walking fly. The pipette is loaded with ATP in order to stimulate $P2X_2$-expressing neurons. The fly is viewed from the front. **e**, The fly turns right after stimulating the left protocerebral bridge (the pipette is on the right side in the image because the camera is facing the fly). **f**, The fly turns left after stimulating the right protocerebral bridge. The motion of the fly's legs and the ball are difficult to convey in sequential images, and ball tracking was not implemented at this stage in the project, and therefore no quantification of these walking experiments are available (only the raw movies). Extensive quantification of walking behavior in relation to protocerebral bridge activity and stimulation is presented in Chapter 3. **g**, Schematic of stimulating neurons in a flying fly. The fly is viewed from below. **h**, Image of fly flying before stimulation. White dashed lines highlight the angle of its wings. **i**, Image of fly turning after stimulating the left protocerebral bridge. The white dashed lines are reproduced from **h**. The red dashed lines highlight the new angles of the wings as the fly turns to the right. **j-k**, Same as **h-i**, for stimulating the right protocerebral bridge. The fly turns left, in the opposite direction compared to **h-i**.

A second set of neurons in NP0212 is required for spontaneous turning

To corroborate the stimulation effect, I inhibited synaptic transmission in the same NP0212-Gal4 line using the temperature-sensitive dynamin mutant, *shibire*^{ts} (Poodry and Edgar 1979). In flies expressing *shibire*^{ts}, synaptic transmission should be abrogated in the targeted cells when the animal is held above 29˚C, but should be normal at room temperature. To determine if inhibiting NP0212 neurons would inhibit turning (i.e. produce the opposite result of stimulation), I expressed *shibire*^{ts} driven by NP0212-Gal4 and measured flight behavior at elevated bath temperatures. When I performed this experiment in flying flies, I observed a drastic reduction in the flies' rate of spontaneous turning, which was initially a promising result. However, this inhibitory effect was not likely due to the same neurons that I had stimulated in the protocerebral bridge for the following reasons. First, I could not reproduce the *shibire*^{ts} effect on turning in other Gal4 lines that drove expression in the same protocerebral bridge neurons. Second, the effect of reduced turning persisted after I eliminated (or greatly minimized) NP0212-driven expression of the relevant protocerebral bridge neurons by expressing in those neurons (using a different enhancer that targets the same cells) a Gal4 transcriptional repressor, Gal80. These results pointed to a second cell type within NP0212-Gal4 that was required for the fly to perform spontaneous turns. Another student in the Maimon laboratory has continued to

investigate which neurons in the NP0212 driver line are required for spontaneous turning in *Drosophila*.

Asymmetric activity in the protocerebral bridge during turning

The behavioral effects of stimulating neurons can be difficult to interpret functionally without knowing the normal physiological patterns of activity in the circuit. I therefore measured neuronal activity in the protocerebral bridge in NP0212-Gal4 during natural turns in flight using the genetically-encoded calcium indicator GCaMP6f (Figure 2.3, see Methods). In these initial imaging experiments, I only analyzed raw imaging frames, which do not lend themselves easily to averaging across flies, since the protocerebral bridge does not have exactly the same shape nor does it occupy exactly the same position in each fly; thus, only analyses from sample flies are shown in this chapter (the other flies in the dataset showed similar results). In Chapter 3, I parse the protocerebral bridge into its individual glomeruli, allowing me to "align" the data across flies, and systematically analyze all flies together. The initial analyses presented in this chapter are included to describe the path by which I arrived at the interpretations presented in Chapter 3. Each conclusion presented here from this initial imaging dataset is analyzed more rigorously and comprehensively in Chapter 3.

In these initial imaging experiments, I elicited turning via a more naturalistic approach. Rather than stimulating neurons in the brain, I presented an expanding visual disc on an LED arena, which simulates an object looming

towards the fly (like a fly swatter, see Methods). Tethered, flying flies routinely and reliably turn away from such looming stimuli. These imaging experiments produced two important insights. The first insight was that when the fly turned left due to the looming stimulus approaching from the right, the left bridge became more active than the right (Figure 2.3a). Likewise, when the fly turned right due to the looming stimulus approaching from the left, the right bridge became more active than the left (Figure 2.3b). To dissociate whether this effect was due to the position of the visual stimulus or to the direction of the turn, I presented looming stimuli directly in front of the fly. With such central looms, flies turned either to the left or to the right on any given trial, with the direction chosen seemingly at random, even though the visual stimulus was identical across trials. In these conditions, the protocerebral bridge activity clearly followed the direction of the fly's turns even though the visual stimulus was the same (Figure 2.3c-e). Only one sample fly out of four is shown because the raw imaging frames do not lend themselves easily to averaging across flies; the other three flies showed similar results (data not shown).

Note that this measured right-left asymmetry during natural turning was opposite in sign to the direction of turning driven by stimulating one side of the bridge. One interpretation of this sign mismatch is that in the ATP/$P2X_2$ stimulation experiments, flies might interpret the artificial activation of one side of the bridge as an indication that they are turning in a specific direction, and then compensated for this undesired turning percept (induced by ATP) by producing a

behavioral turn in the opposite direction. However, a concern for any rigorous interpretation of the ATP/ $P2X_2$ stimulation experiments described here is the fact that the stimulation protocol I initially used for discovering the P-ENs produced an activation of these cells that was very strong in comparison to physiological levels, as assessed by simultaneous stimulation and $[Ca^{2+}]$ imaging from P-ENs (data not shown). It is for these reasons that I did not comprehensively analyze or extensively repeat the experiments described in Figures 2.2. Rather, I used these initial results to motivate a few more first-pass analyses of the physiological activity in these cells (see immediately below) and, ultimately, a much more comprehensive examination of these cells in walking flies, with more physiological levels of stimulation (see Chapter 3).

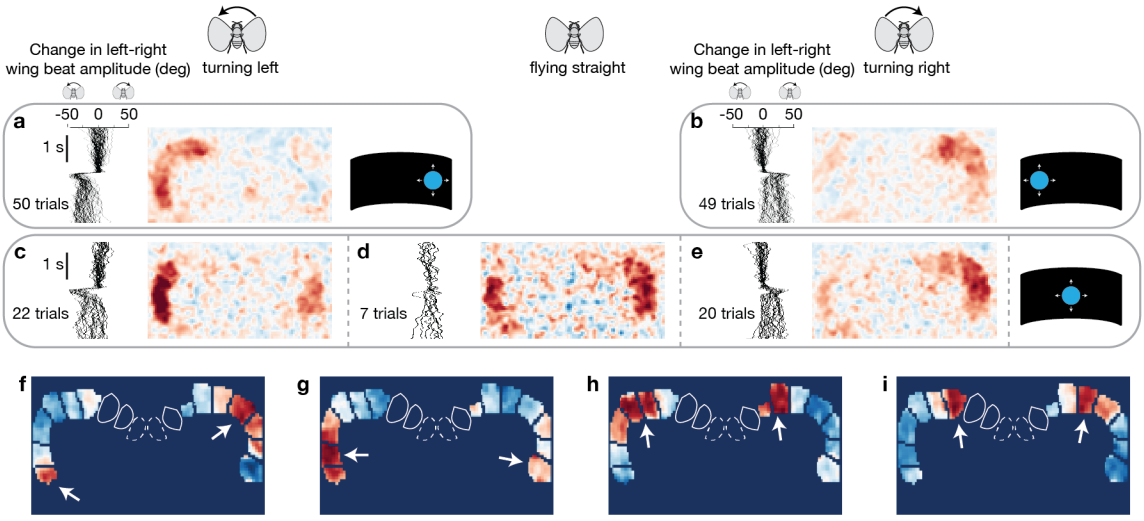

Figure 2.3 | Initial characterization of an asymmetric and periodic signal in the protocerebral bridge.

a, Change in bridge activity in NP0212>GCaMP6f for one of four flies (other flies not shown). The fly was presented with an expanding disk on its right, and in response turned left. (Left) Left-right wing beat amplitude for all trials. A leftward deviation indicates a left turn. (Center) The change in bridge activity across trials. The mean activity in the 0.1 s prior to the disc expanding was subtracted from the mean activity 0.3-1.4 s after (the time period during which the fly turned). (Right) Schematic of the expanding-disk stimulus presented on the right. **b**, Same as **a**, for an expanding disk presented on the left and the fly turning right. **c**, Same as **a**, for an expanding disk presented in the center, and where the fly turned left. **d**, Same as **c**, for when the fly did not turn strongly in response to the central expanding disk. **e**, Same as **c**, for when the fly turned right in response to the central expanding disk. **f-i**, Centroids from k-means clustering (k=8) of the change in bridge activity (as defined for **a-e**) in each trial for one fly. The bridge was masked in order to only cluster information from the bridge. 4/8 centroids are shown. The other centroids are either very similar to **f-i**, or show relatively little activity across the bridge. The centroids are reordered by hand to highlight the activity peaks gradually shifting clockwise, or to the right, in the protocerebral bridge. Note that I only imaged one plane for these initial experiments. The expected number of missing glomeruli are outlined in white (their positions are not known exactly, these are drawn only as a visual aid). Solid-outlined glomeruli highlight the remaining glomeruli innervated by P-ENs (and NP0212). Dashed-outlined glomeruli highlight the remaining glomeruli not innervated by P-ENs (or NP0212). The activity peaks are separated by approximately 8 glomeruli, counting the absent, outlined glomeruli in the middle. Also note that the exact position of a peak that borders on un-sampled glomeruli is less well defined. White arrows designate the positions of activity peaks observable within the imaging plane.

Periodic activity in the protocerebral bridge

The above analysis of the NP0212 GCaMP signal in the bridge in flying flies considered the *average* activity in the bridge across left turns and across right turns. However, when I analyzed the same signals on a trial-by-trial basis, the GCaMP signals were more variable. Specifically, I never saw the whole left bridge or the whole right bridge activated on any given trial (like one sees in the averages of Fig. 2.3a-e). Rather, on single trials, I observed 2-3 peaks of activity—occupying different *glomeruli* or sectors of the bridge—that were active on each side of the bridge on any given trial, with the peaks occupying different positions along the bridge across trials, whether for left or right turns. Furthermore, whenever one set of 2-3 glomeruli was active on the left bridge, I observed the same associated set of 2-3 glomeruli being co-active on the right bridge, indicating that the left and right bridge are linked in their activity in some fashion, and not completely independent. To further analyze the GCaMP activity patterns, I performed a cluster analysis of the activity across trials, using k-means clustering of the imaging frames. The aim of this analysis is to isolate a relatively small number of representative frames from the dataset, starting from the anecdotal observation that many individual frames appear to have very similar patterns of activity. Specifically, for each trial, I computed the change in the GCaMP signal during disc expansion (i.e. I subtracted the mean signal -0.1 to 0 s from the mean signal 0.3 to 1.4 s relative to the start of the disc expansion). Pixels from surrounding regions outside the bridge were masked (set to zero) in

order to only analyze the bridge activity. I then treated each “change in GCaMP” frame from each trial as a 1D vector of pixel intensities (for example, with a length of 5100 if the original image dimensions were 51x100 pixels). Each trial, or 1D vector, was treated as one sample point (in 5100-dimensional space, in the example above) in the k-means clustering algorithm. This clustering algorithm attempts to find the positions of a given number (“k”) of centroids, or points, that minimize the total distance between each sample point and its nearest centroid by iteratively testing different centroid positions. Ultimately, this method isolated frames with similar activity patterns and allowed me to visualize the averages of those frames. This approach revealed the second central insight from these imaging experiments: the activity in the bridge appeared to consist of a set of activity peaks (smaller than the entire side of a bridge) whose position shifted by the same amount along the left and right side of the bridge (Figure 2.3f-i, putative activity peaks are highlighted with arrows). That is, the data were consistent with the peaks always being ~8 glomeruli apart, taking into account that some glomeruli in the middle of the bridge were beyond the imaging plane in these initial single-z-plane imaging experiments (subsequent experiments systematically imaged all glomeruli in the bridge, see Chapter 3). Finally, the activity pattern appeared periodic in that if one imagined the activity peaks systematically shifting along the bridge, they would eventually wrap around and return to the same position from which they started (Figure 2.3f-i). Only one

sample fly out of four is shown here; the other three flies showed similar results (data not shown).

Interpreting protocerebral bridge activity patterns

Considering that these bridge neurons were involved in turning, both from the stimulation-induced turning experiments and from the GCaMP signals described above, I reasoned that the most likely *periodic* signal that could be carried in these neurons was the fly's *orientation* (since turning velocity is not periodic). This interpretation was further bolstered by the discovery of an orientation signal in a different set of central complex neurons, which innervate the ellipsoid body. I first learned about these other neurons at a seminar given by Vivek Jayaraman (Columbia Workshop on Brain Circuits, Memory and Computation, March 16-17, 2015) and later read about them in the associated publication (Seelig and Jayaraman 2015). In addition to the ellipsoid body, the neurons in the Seelig and Jayaraman 2015 study also innervate the protocerebral bridge and the gall. These cells are called E-PG neurons, with the "E", "P" and "G", representing the three central complex structures that they innervate (see Chapter 3). I found that in my early experiments performed in flying flies, I could not reliably detect an orientation signal in the form of smoothly moving activity peaks in the bridge in real time. This was true both in the open-loop tethered-flight experiments with looming objects described above and even when I placed the fly in a simple virtual reality condition, where its own wing

movements controlled the angular velocity of a bar in closed-loop, simulating flight with a distant static landmark, like the sun. Given the failure to observe a reliable heading signal in tethered flight, I reasoned that these virtual reality experiments might be better suited to a fly walking on a ball, since here I could measure the *effect* of the fly's leg movements on the ball, rather than inferring the fly's intention to turn purely from the movements of its wings, as is done in flight. It is also possible that the fly receives more appropriate proprioceptive feedback from its legs when it is tethered and walking on a ball compared to the feedback from its wings when it is tethered and flying. These tethered walking experiments indeed revealed reliable heading signals in real time and these signals helped in determining the functional interactions between P-ENs and E-PGs, which is the focus of Chapter 3.

Chapter 3 | A neuronal circuit architecture for angular integration

This chapter describes the interaction between two sets of central complex neurons that function in a circuit to track the fly's heading. A neuronal shifting mechanism is proposed to account for the ability of this system to track the fly's heading without landmark cues. This mechanism is akin to models proposed for rodent head direction cells. The immunohistochemistry presented in this chapter was performed and analyzed by Atsuko Adachi.

Heading signals in the central complex

I focus on two cell types that make direct connections between the protocerebral bridge and the ellipsoid body in the fly central complex: **E-PGs** (ellipsoid body-protocerebral bridge-gall neurons, also $PB_{G1–8}$.b-EBw.s-D/Vgall.b (Wolff, Iyer, and Rubin 2015) or EIP (Lin et al. 2013), Figure 3.1a-b) and **P-ENs** (protocerebral bridge-ellipsoid body-noduli neurons*,* also $PB_{G2–9}$.s-EBt.b-NO_1.b (Wolff, Iyer, and Rubin 2015)*,* PEN (Lin et al. 2013), or *shifting neurons* herein, Figure 3.1a-b). The dash separates the structure(s) from which the neuron receives input (i.e. putative dendrites, as assessed by thinly shaped neurites) from the structures to which the neuron outputs (i.e. putative axonal terminals, as assessed by larger, bleb-shaped terminals). For example, P-ENs take inputs from the bridge and send outputs to the ellipsoid body and noduli,

based on the morphology of their arborizations (Wolff, Iyer, and Rubin 2015). Each cell type tiles both the protocerebral bridge and the ellipsoid body.

To assess the role of E-PGs and P-ENs in building an internal heading signal, I first measured calcium levels in each cell type separately using the genetically encoded calcium indicator, GCaMP6m (T.-W. Chen et al. 2013), under two-photon excitation (see Methods). I imaged P-ENs from two independent Gal4 driver fly lines, VT032906-Gal4, which I call P-EN1, and VT020739-Gal4, which I call P-EN2, since I observed differences in their physiology in later experiments (see below). In all figures, the fly brain is viewed from the posterior side, such that the left bridge is displayed on the left and the right bridge on the right. In all experiments, the fly was tethered (Maimon, Straw, and Dickinson 2010) and walking on an air-cushioned ball (Seelig et al. 2010; Moore et al. 2014) at the center of a cylindrical (270˚ panoramic) LED arena (Reiser and Dickinson 2008) (Figure 3.1c, see Methods). I presented the fly with either a dark screen or a bright vertical bar that rotated in closed loop with the fly's behavior, simulating a fixed, distant, landmark (Figure 3.1c, see Methods). In both conditions, I observed two or three periodic peaks of activity in the bridge for each cell type, with a periodicity of approximately 8 glomeruli (Figure 3.1d-i, Figure 3.2a-i, Figure 3.3, see Methods). In all cell types, these peaks moved in unison to the left or right along the bridge as the fly turned right or left, respectively. Since these bridge signals are periodic, their position can be estimated by taking a Fourier transform of the 18-element vector of bridge activity

from each time point and extracting the phase of the Fourier component at 8 glomeruli (Figure 3.2a-i, Figure 3.3, see Methods). This *phase* (i.e. the position of these peaks in the bridge) quantitatively tracks the virtual heading of the fly (Figure 3.1g-l). Given a bar in closed-loop, the phase tracks the bar's position with an offset that is typically constant for many minutes, but differs from fly to fly (Figure 3.2j-l). Put another way, the calcium activity of each glomerulus responds to the position of the bar with a tuning curve that peaks at a specific bar position on the arena (Figure 3.4). In the dark, however, the phase tracks the fly's heading with an error that accumulates over time, consistent with a system that integrates self-motion inputs (Figure 3.3). These properties, measured for three cell types in the bridge, are very similar to those previously observed for rodent head-direction cells (Taube, Muller, and Ranck 1990a; Taube, Muller, and Ranck 1990b) and E-PGs in the ellipsoid body (Seelig and Jayaraman 2015).

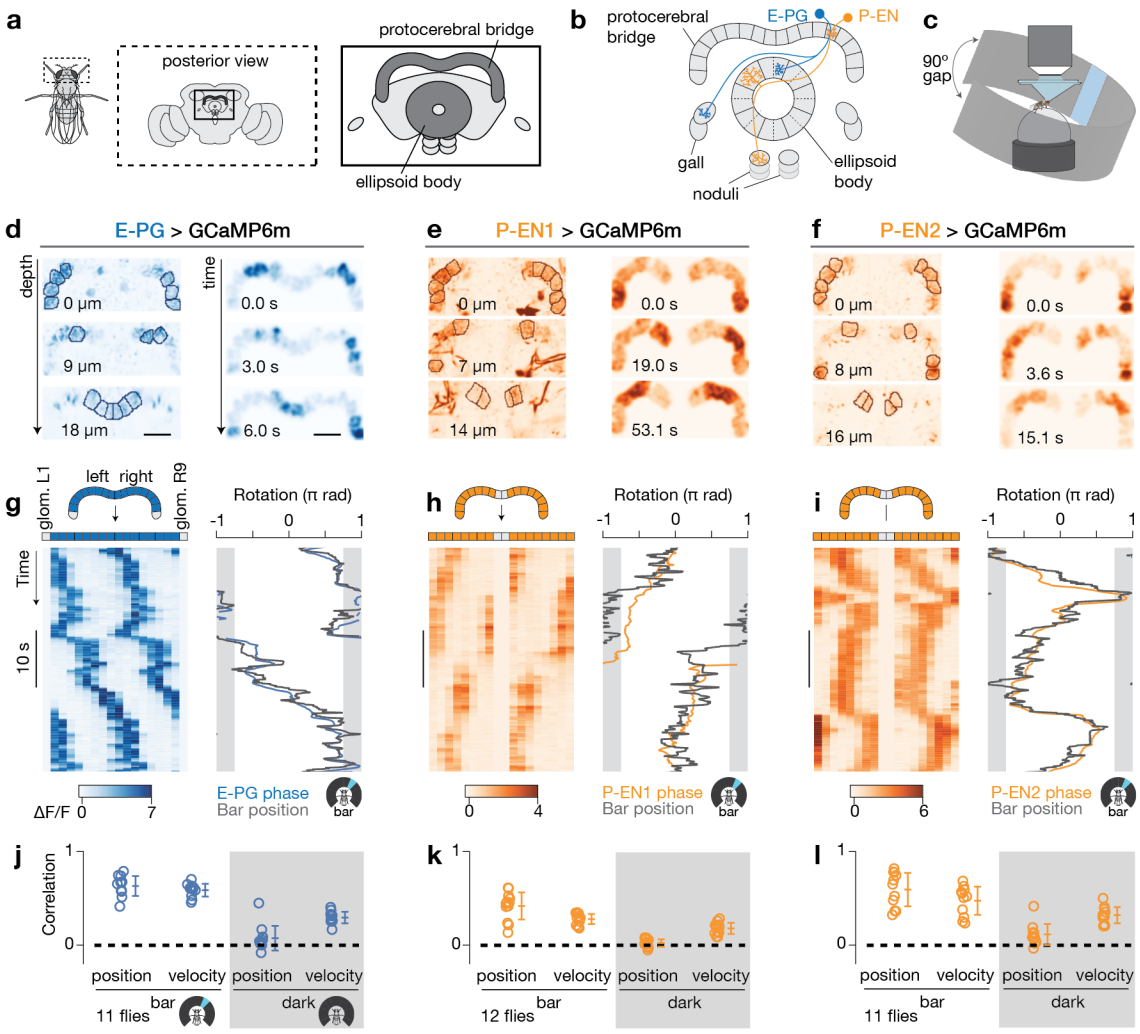

Figure 3.1 | The activity of three cell types in the bridge tracks the fly's heading.

a, Schematic of the bridge and ellipsoid body in the fly brain. **b**, Example E-PG and P-EN neurons. **c**, I imaged a tethered fly walking on a ball with an LED arena. **d-f**, GCaMP6m images for each cell type. (Left) Each z slice, outlining glomeruli. (Right) Z-projected bridge volumes over time. Scale bars, 20 μm. **g-i**, (Left) Bridge activity as the fly walks with a bar in closed-loop. (Right) Phase of the bridge activity and bar position. The 90º gap in the back of the arena is highlighted in gray. **j-l**, Correlations between phase and ball-position and phase- and ball-velocity. Each circle represents one fly. The mean and s.d. across flies are shown. P-ENs are in orange and E-PGs in blue throughout.

Figure 3.2 l Processing of protocerebral bridge signals from E-PG, P-EN1 and P-EN2 neurons in the presence of a closed-loop bar.

a, Processing of the EPG>GCaMP6m signal to generate the plot in Figure 3.1g. From left to right: raw mean signal in each glomerulus over time, z-score normalization for each glomerulus independently, ΔF/F normalization for each glomerulus independently, power spectrum of the ΔF/F signal computed for each time point (row) independently. The E-PG phase of the ΔF/F signal is overlaid on each GCaMP plot in black. **b**, E-PG phase (blue) shifted with a constant offset to best match the bar position (dark grey). **c-d**, Same as **a**, except for P-EN1, originally plotted in Figure 3.1h. The fact that P-EN cells do not innervate the middle two glomeruli of the bridge makes the power spectrum analysis slightly more complex. Specifically, black arrows highlight transient peaks in the power spectrum at approximately 16 glomeruli, which are artifacts of the P-EN GCaMP peaks crossing the center of the bridge. **d**, From left to right: P-EN1 ΔF/F signal with the middle two glomeruli filled in by averaging signals located one period (8 glomeruli) away, power spectrum of the 'filled in' ΔF/F bridge signal (note absence of artefactual peaks at 16 glomeruli), P-EN phase extracted from the Fourier component with a period of 8 glomeruli of the 'filled in' ΔF/F bridge signal (orange), shifted with a constant offset to best match the bar position (dark grey). **e-f**, Same as **c-d**, for P-EN2, originally plotted in Fig. 1i. In all plots showing bar position over time, the gap in the arena where the bar is not displayed is shown in grey. **g-i**, Periodicity of the bridge signal at peak power in the power spectrum for each cell type. Each circle represents one fly. The mean and s.d. are shown. **j-l**, Offsets that minimize the distance between GCaMP phase and bar position for all 50 s trials for each cell type. Only data where the bar was visible were included in computing the offsets. In **l**, fly 10 only had 3 bar trials. See Methods for details. a.u.: arbitrary units. DFT: discrete Fourier transform.

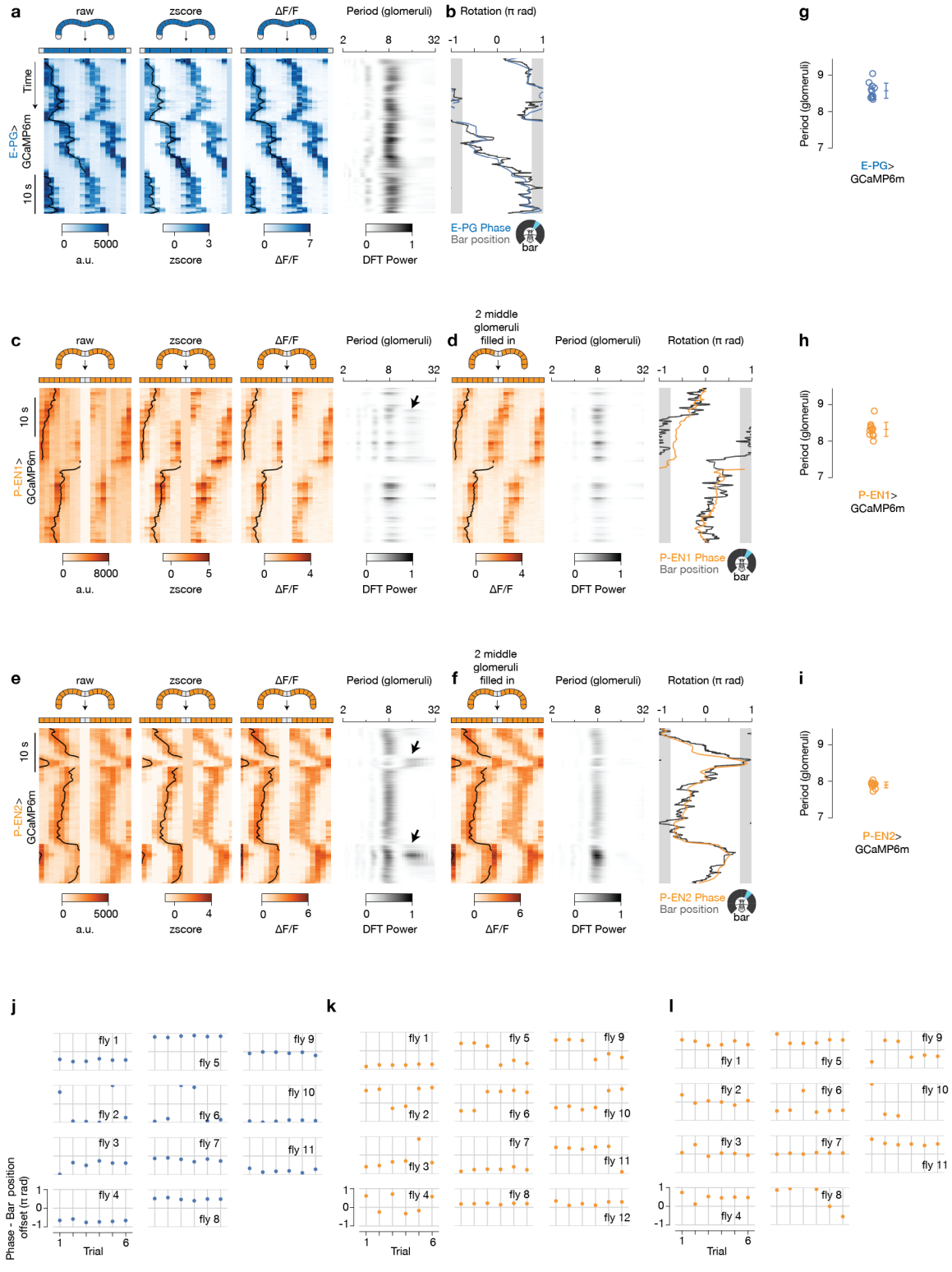
a
raw
zscore
ΔF/F
Period (glomeruli)
b Rotation (π rad)
Time
E-PG>
GCaMP6m
10 s
0 5000
a.u.
0 3
zscore
0 7
ΔF/F
0 1
DFT Power
E-PG Phase
Bar position
bar
g
Period (glomeruli)
E-PG>
GCaMP6m
c
d
2 middle
glomeruli
filled in
Rotation (π rad)
P-EN1>
GCaMP6m
0 8000
0 5
0 4
P-EN1 Phase
h
P-EN1>
GCaMP6m
e
f
P-EN2>
GCaMP6m
0 6
P-EN2 Phase
i
P-EN2>
GCaMP6m
j
k
l
fly 1
fly 2
fly 3
fly 4
fly 5
fly 6
fly 7
fly 8
fly 9
fly 10
fly 11
fly 12
Phase - Bar position offset (π rad)
Trial

Figure 3.3 | Processing of protocerebral bridge signals from E-PG, P-EN1 and P-EN2 neurons in the dark.

a, Processing of the E-PG>GCaMP6m signal to generate the plot in Figure 3.5g. Bridge signals are plotted over time as in **Figure 3.2**a, except in the dark. **b**, Phase from the ΔF/F signal and ball position. Because the phase and ball position drift over time in the dark, I did not align the two signals by finding the best offset over the entire trial; rather, I nulled the offset between the GCaMP phase and ball heading at time zero, letting the signals naturally drift over time. For display purposes, I applied a constant gain to the ball position signal, which I determined from the slope of a linear regression between the GCaMP phase- and ball-velocity. **c-d**, P-EN1 signals (originally plotted in Figure 3.13a) over time as in **Figure 3.2**c-d, except in the dark. **e-f**, Same as **c-d**, except for P-EN2 (originally plotted in Fig. 4b). The ball position gains are 0.75 for E-PG (**b**), 1.0 for P-EN1 (**d**), and 0.89 for P-EN2 (**f**). For P-EN1, the slope of the linear regression between phase- and ball-velocity was poorly estimated (see Discussion) and thus I hand-picked the gain (1.0) in this case. That these gains are not all equal does not mean that each cell type has its own gain (see Discussion). Note the different timescale compared to **Figure 3.2**. Also note the time window was expanded in **a-b**, compared to Figure 3.5g, to be the same length as **c-f**. **g-i**, Periodicity of the bridge signal at peak power in the power spectrum for each cell type. Each circle represents one fly. The mean and s.d. are shown. a.u.: arbitrary units. DFT: discrete Fourier transform.

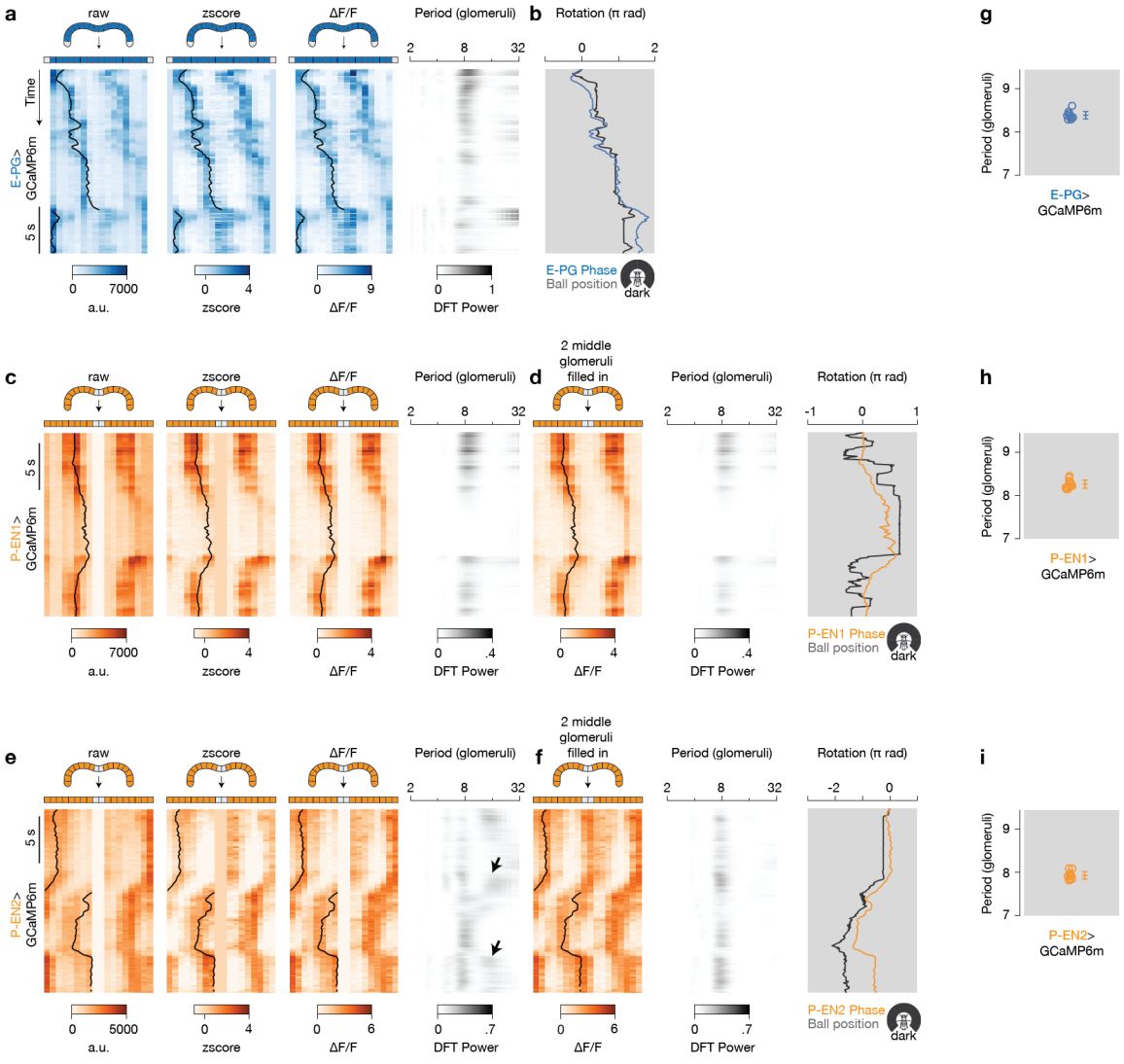
a
raw
zscore
ΔF/F
Period (glomeruli)
b
Rotation (π rad)
Time
E-PG>
GCaMP6m
5 s
0 7000
a.u.
0 4
zscore
0 9
ΔF/F
0 1
DFT Power
E-PG Phase
Ball position
dark
g
Period (glomeruli)
E-PG>
GCaMP6m
c
d
2 middle
glomeruli
filled in
P-EN1>
GCaMP6m
0 .4
DFT Power
P-EN1 Phase
h
P-EN1>
GCaMP6m
e
f
P-EN2>
GCaMP6m
0 5000
0 6
0 .7
P-EN2 Phase
i
P-EN2>
GCaMP6m

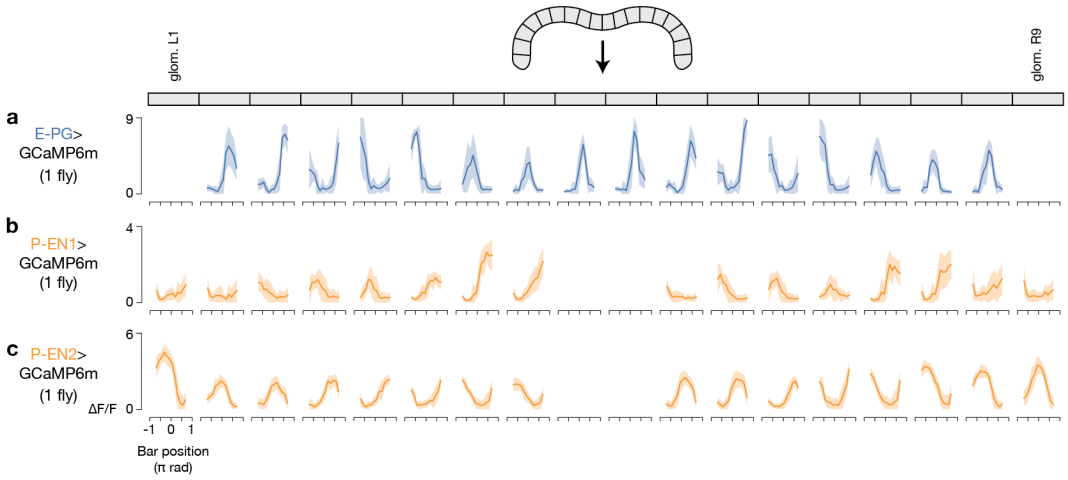

Figure 3.4 l Example visual tuning curves in E-PG, P-EN1 and P-EN2 neurons across glomeruli in the protocerebral bridge.

a-c, Tuning curves of GCaMP activity as a function of bar position for each glomerulus in a sample fly for E-PGs (**a**), P-EN1s (**b**) and P-EN2s (**c**). Data associated with bar positions in the 90º gap in the back of the arena (and are not visible) are not shown. The mean and s.d. across time points for each 22.5º bar position bin are shown.

A model for angular integration

Do P-ENs and E-PGs interact in a circuit to track the fly's heading? The first clue came from analyzing a previous anatomical study (Wolff, Iyer, and Rubin 2015) for how each cell type maps between the bridge, a linear array of 18 glomeruli, and the ellipsoid body, a circular array of 8 tiles (Wolff, Iyer, and Rubin 2015) (Figure 3.5a). This analysis revealed that left- and right-bridge P-ENs project clockwise and counterclockwise, respectively, to the ellipsoid body (Figure 3.5a, orange arrows, Figure 3.6a-l, Table 3.1). E-PGs, on the other hand, project without shifting from the ellipsoid body to the bridge (Figure 3.5a, blue arrows). While the full connectome for this circuit will surely reveal more complexity, this coarse level of description already suggests a path by which an activity peak could propagate clockwise or counterclockwise around this circuit when the fly turns. For example, supposing reciprocally excitatory interactions between E-PGs and P-ENs, E-PG activity in tile 5 of the ellipsoid body would activate P-EN cells in glomerulus 5 in both the left and right bridge (Figure 3.5a, using a slightly modified numbering scheme from the one used in Wolff, Iyer, and Rubin 2015, see Figure 3.6a-d). If, when the fly turns right, the right-bridge P-ENs were to become more active than their left-bridge counterparts (Figure 3.5b), these right-bridge P-ENs would drive the E-PGs in tile 4 in the ellipsoid body, shifting the E-PG activity peak by one tile counterclockwise (Figure 3.5c). The E-PG activity in tile 4 in the ellipsoid body would then reverberate back to activate P-ENs in glomerulus 4 in the bridge, shifting P-ENs to the left in the

bridge in unison with E-PGs (Figure 3.5d). If the fly continued to turn right, the E-PG and P-EN activities would continue propagating leftward in the bridge and counterclockwise in the ellipsoid body, with stronger turning driving larger asymmetries in P-EN activity and the E-PG peak to propagate faster. The opposite sequence of events would cause the E-PG peak to rotate clockwise in the ellipsoid body if the fly turned left. In this way, an asymmetry in the activity of the right versus left P-ENs could cause the E-PG signal to rotate in one direction or the other in response to the fly turning.

Figure 3.5 | P-EN neurons in the left and right bridge are asymmetrically active when the fly turns, consistent with an anatomically-inspired model for neural integration.

a-d, How an asymmetry in left and right P-EN neurons might rotate the E-PG phase (see text). Note that I use a revised numbering scheme. **e-g**, Bridge activity and accumulated phase in constant darkness for each cell type. Arrows highlight right-left asymmetries when the fly turns. **h-j**, Right - left bridge activity (bottom) triggered on the fly's turning velocity (top). The mean and s.e.m. across turns are shown. **k-m**, Right - left bridge activity vs turning velocity. Thin lines represent single flies. Thick lines represent the mean across flies. **h-m** are averaged over bar and dark conditions.

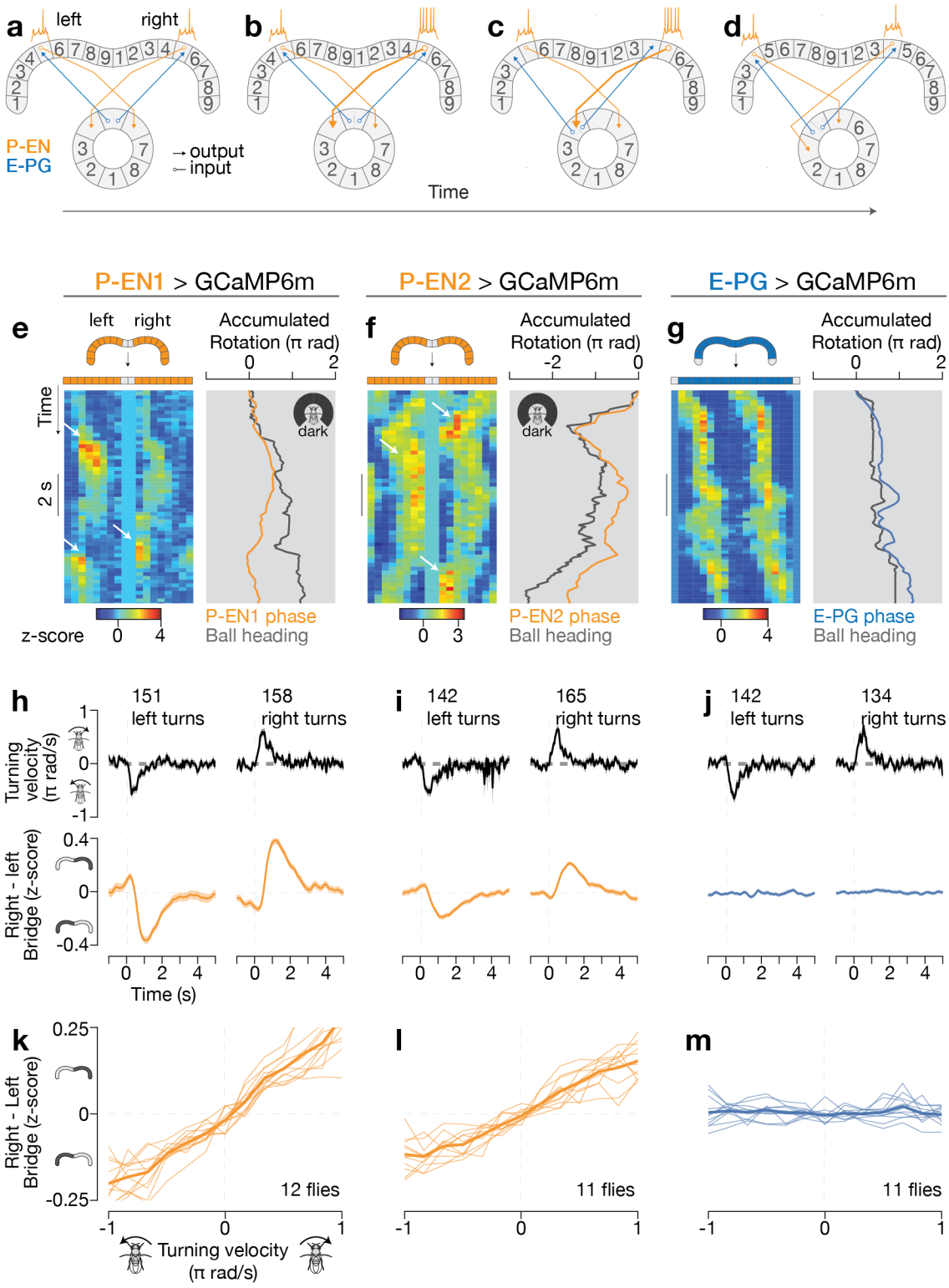
a
left
right
b
c
d
P-EN
E-PG
output
input
Time
P-EN1 > GCaMP6m
P-EN2 > GCaMP6m
E-PG > GCaMP6m
e
f
g
left
right
Accumulated Rotation (π rad)
Time
2 s
dark
z-score
P-EN1 phase
Ball heading
P-EN2 phase
E-PG phase
h
i
j
151 left turns
158 right turns
142 left turns
165 right turns
142 left turns
134 right turns
Turning velocity (π rad/s)
Right - left Bridge (z-score)
Time (s)
k
l
m
Right - Left Bridge (z-score)
12 flies
11 flies
11 flies
Turning velocity (π rad/s)

Figure 3.6 | P-EN neuroanatomy: explanation for the numbering scheme, sytGFP localization, and multicolor single cell labeling.

a, Numbering used in the literature for the protocerebral bridge and ellipsoid body. **b**, Rearrangement of the left- and right-bridge and a linearized ellipsoid body that highlights the pattern of anatomical projections for E-PGs and P-ENs. Arrows indicate the expected direction of signaling (dendrite to axon) for each cell (Wolff, Iyer, and Rubin 2015; Lin et al. 2013) (also see **e-f**). The dashed line in **a** shows where the ellipsoid body is opened to display it linearly. Tile 1 is repeated as a visual aid, since the ellipsoid body is circular. **c-d**, Same as **a-b**, except using our revised numbering. In **d**, the numbers are constant along each column (with the exception that glomerulus 9 from either side of the bridge matches up with ellipsoid body tile 1), highlighting the fact that E-PGs project within the same column, whereas left-bridge P-ENs project to the right (+1, or clockwise) and right-bridge P-ENs project to the left (-1, or counterclockwise). This mapping cannot be so easily summarized with the numbering scheme in **b**. **e-f**, Sample images of synaptotagmin-GFP (labeling putative axonal terminals) and tdTomato (labeling the entire cell) expressed in P-EN1 (**e**) and P-EN2 (**f**) neurons. These data are consistent with P-ENs having presynaptic terminals in the ellipsoid body and noduli, but few, if any, in the protocerebral bridge. **g-l**, Sample multicolor flip out images for P-EN neurons driven by VT032906-Gal4 (P-EN1, **g-h**), VT020739-Gal4 (P-EN2, **i-j**), and 12D09-Gal4 (P-EN2, **k-l**). The multicolor flip out method (Nern, Pfeiffer, and Rubin 2015) allows one to visualize single randomly selected cells from a Gal4 driver line (which might label a dense thicket of cells) in their entirety, like a multi-color Golgi stain. Neuropil is in grey. Single neurons are in color. Glomerulus numbers, including ‘L’ for left and ‘R’ for right, are shown in the bridge. After tracing each neuron from the bridge to the ellipsoid body, Atsuko labeled the terminals in the ellipsoid body with the bridge glomerulus from which they originated, using our revised numbering scheme (**c-d**). VT032906-Gal4 contains a neuron type that passes near the bridge, but does not innervate the bridge, ellipsoid body or noduli, for example the green neuron in **g**. VT020739-Gal4 contains a neuron type that innervates the noduli, but not the ellipsoid body or bridge, for example the blue neurons innervating the noduli from the sides in **j**. Virtually all neurons labeled in the bridge and ellipsoid body were consistent with being P-ENs (see Table 3.1). 12D09-Gal4 very rarely revealed flip-outs of protocerebral bridge local neurons, not shown here (seeTable 3.1). sytGFP: synaptotagmin-GFP, pb: protocerebral bridge, eb: ellipsoid body, no: noduli. These immunohistochemistry experiments were performed by Atsuko Adachi.

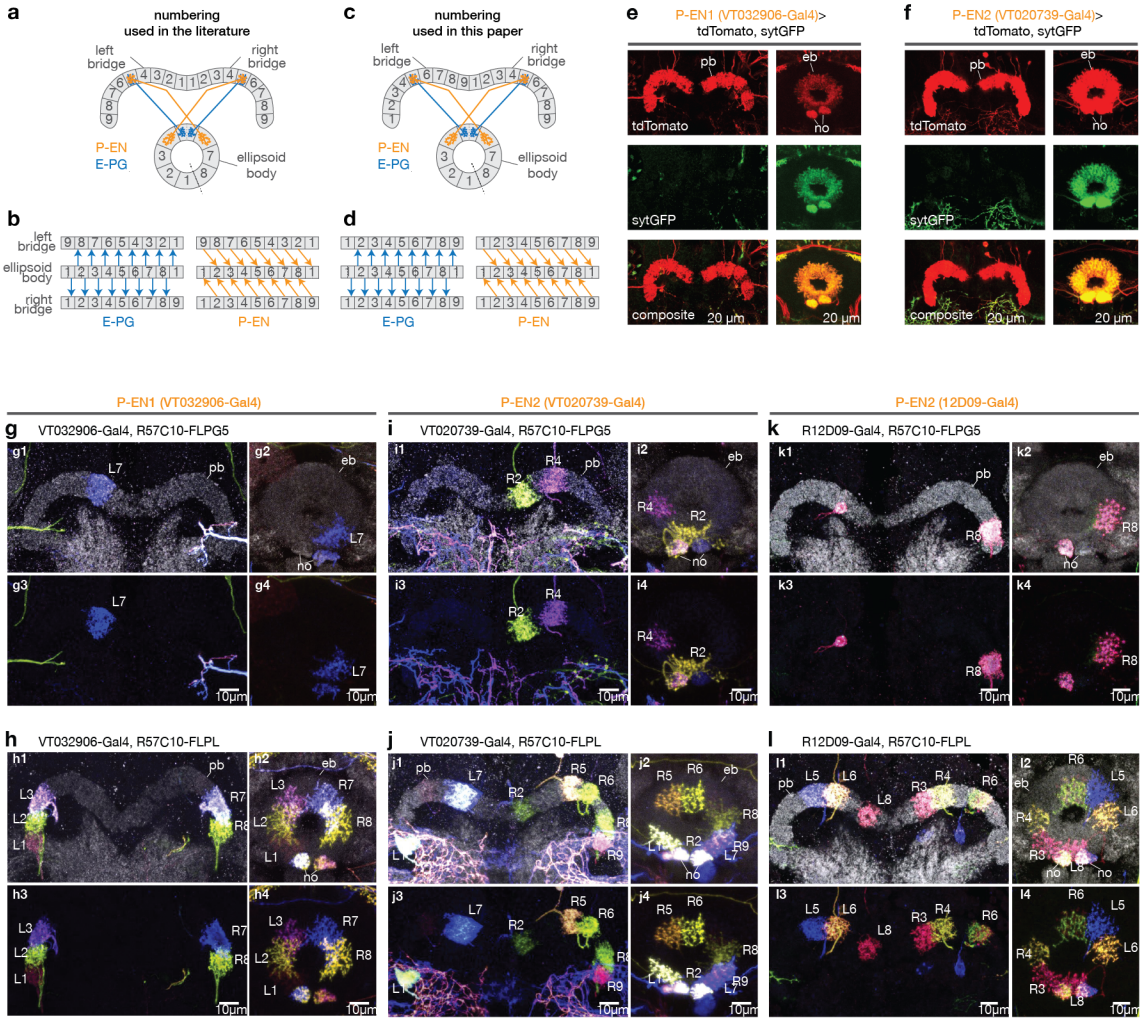
a
numbering
used in the literature
left bridge
right bridge
P-EN
E-PG
ellipsoid body
b
left bridge
ellipsoid body
right bridge
E-PG
P-EN
c
numbering
used in this paper
left bridge
right bridge
P-EN
E-PG
ellipsoid body
d
E-PG
P-EN
e
P-EN1 (VT032906-Gal4)>
tdTomato, sytGFP
pb
eb
tdTomato
no
sytGFP
composite
20 µm
f
P-EN2 (VT020739-Gal4)>
tdTomato, sytGFP
pb
eb
tdTomato
no
sytGFP
composite
20 µm
P-EN1 (VT032906-Gal4)
P-EN2 (VT020739-Gal4)
P-EN2 (12D09-Gal4)
g
VT032906-Gal4, R57C10-FLPG5
g1
L7
pb
g2
eb
L7
no
g3
L7
g4
L7
10µm
i
VT020739-Gal4, R57C10-FLPG5
i1
R4
pb
R2
i2
eb
R4
R2
no
i3
R4
R2
i4
R4
R2
10µm
k
R12D09-Gal4, R57C10-FLPG5
k1
pb
R8
k2
eb
R8
no
k3
R8
k4
R8
10µm
h
VT032906-Gal4, R57C10-FLPL
h1
pb
L3
R7
L2
R8
L1
h2
eb
L3
R7
L2
R8
L1
no
h3
L3
R7
L2
R8
L1
10µm
h4
L3
R7
L2
R8
L1
10µm
j
VT020739-Gal4, R57C10-FLPL
j1
pb
L7
R5
R6
R2
R9
j2
R5
R6
eb
R8
R2
R9
L7
no
j3
L7
R5
R6
R2
R9
j4
R5
R6
R8
R2
R9
L7
10µm
l
R12D09-Gal4, R57C10-FLPL
l1
pb
L5
L6
R4
R6
L8
R3
l2
R6
L5
eb
L6
R4
R3
L8
no
no
l3
L5
L6
R4
R6
L8
R3
10µm
l4
R6
L5
L6
R4
R3
L8
10µm

Turning velocity signals in P-ENs

Consistent with this model, in addition to the GCaMP peaks shifting along the bridge (Figure 3.1), I observed an asymmetry in the amplitude of the left and right P-EN peaks, but not E-PG peaks, when the fly turned (Figure 3.5e-g, white arrows). To quantify this asymmetry, I subtracted the GCaMP signal averaged across all glomeruli in the left bridge from that averaged across the right bridge, and computed the time course of this right – left GCaMP signal triggered on the start of left and right turns (Figure 3.5h-j, see Methods). When the fly turned right, I observed a transient increase in activity on the right bridge relative to the left (hereafter referred to as the *bridge asymmetry*) for both P-EN lines, and vice versa when the fly turned left (Figure 3.5h,i). I observed this asymmetry when the fly turned in the dark — or with a closed-loop bar — (Figure 3.7) indicating that the asymmetry does not require visual inputs.

In principle, a fly can know how fast it is turning based on vestibular, proprioceptive, efference copy, or visual-motion cues. Our tethered preparation, unfortunately, precludes testing the role of vestibular cues, which I do not consider further. The fact that the asymmetry persists in darkness argues that proprioceptive and/or efference copy inputs are sufficient to generate a rotation of the central-complex heading system. However, it is possible that visual motion cues also serve a role in angular integration (not just landmark based updating) when present. Consistent with a role for visual cues in angular integration, I also observed a P-EN asymmetry when the fly was not physically turning, but rather

was viewing panoramic visual motion (i.e. optic flow) that it would normally experience during a real turn (Figure 3.8). I designed the optic flow stimulus as an array of (1.875˚) dots, each of which appeared on the screen, moved four pixels (7.5˚) to the left or right, and then disappeared and reappeared elsewhere on the screen (Newsome and Pare 1988) (see Methods). Such a limited-lifetime-dots motion stimulus contains only visual motion (i.e. optic flow) information and no coherent landmark (positional) information to drive a P-EN asymmetry. The fact that the P-EN asymmetry could be driven by a pure motion stimulus of this sort indicates that this asymmetry is also sensitive to visual cues informative on the animal's angular velocity, not just proprioceptive or efference copy signals. Interestingly, I found that on trials in which the fly performed a locomotor turn in response to the visual motion (i.e., performed the classical optomotor response), the P-EN asymmetry was generally weaker than on trials in which the fly did not perform a behavioral turn in response to the motion, on average (Fig. 3.8 orange curves have a weaker deflection on the bottom eight panels compared to the top eight panels). The simplest interpretation of this result is that the P-EN bridge asymmetry is driven by a weighted interaction of visual motion inputs and proprioceptive/efference copy inputs onto P-ENs. In this view, on trials where the fly performed an optomotor response, the visual motion inputs informed the heading system that the fly was turning in one direction and proprioception/efference-copy inputs informed the system that the fly was turning

in the other direction, leading to a smaller net asymmetry in the P-ENs than in trials where the fly performed no optomotor response.

Independent of the exact origin of the asymmetry in P-ENs, the model in Figure 3.5a-d would suggest that the harder the fly turns the stronger the asymmetry should be in P-ENs, in order to drive a faster rotation of the heading system. Consistent with this prediction, I found a quantitative, positive relationship between right - left GCaMP and the fly's turning velocity for both P-EN lines (Figure 3.5k,l), but not E-PGs (Figure 3.5m) (see Methods). This bridge asymmetry between left and right P-ENs could therefore provide the quantitative signal necessary for integrating the fly's turns over time.

Figure 3.7 | P-EN1 and P-EN2 bridge asymmetry during turns in closed-loop bar and dark conditions, computed with z-score and ΔF/F normalizations.

a-c, Right - left bridge activity (bottom) and the fly's turning velocity (top), averaged over multiple turns, for P-EN1s (**a**), P-EN2s (**b**), and E-PGs (**c**), as in Figure 2h-j, in closed-loop bar conditions. The right – left GCaMP signal is computed from z-score normalized data. **d-f**, Same as **a-c**, except in constant darkness. **g-l**, Same as **a-f**, except the right – left GCaMP signal is computed from ΔF/F normalized data. The mean and s.e.m. across turns are shown. Only data where the bar was visible on the front 270º of the LED arenea were included for closed-loop bar plots. See Methods for details.

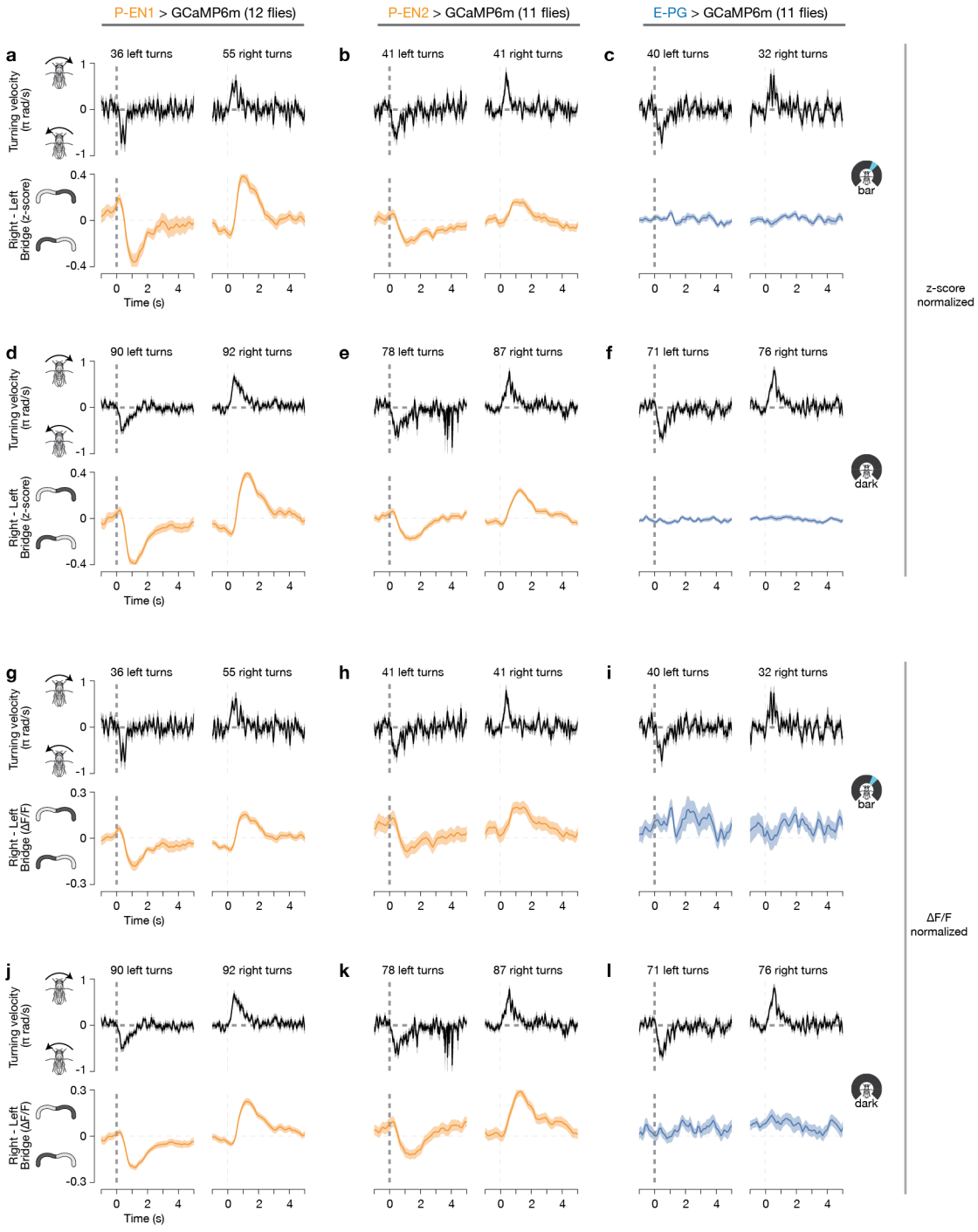
P-EN1 > GCaMP6m (12 flies)
P-EN2 > GCaMP6m (11 flies)
E-PG > GCaMP6m (11 flies)
a
36 left turns
55 right turns
b
41 left turns
41 right turns
c
40 left turns
32 right turns
d
90 left turns
92 right turns
e
78 left turns
87 right turns
f
71 left turns
76 right turns
g
36 left turns
55 right turns
h
41 left turns
41 right turns
i
40 left turns
32 right turns
j
90 left turns
92 right turns
k
78 left turns
87 right turns
l
71 left turns
76 right turns
Turning velocity (π rad/s)
Right - Left Bridge (z-score)
Right - Left Bridge (ΔF/F)
Time (s)
bar
dark
z-score normalized
ΔF/F normalized

Figure 3.8 | P-EN1 and P-EN2 asymmetries are driven in part by optic flow.

a, Sample trajectory of one of hundreds of dots used to create our optic flow stimulus. Each dot appeared at a random location, traveled 4 azimuthal pixels (7.5^o), and then disappeared. The dashed circle is drawn as a point of reference, and is not actually presented on the screen. **b-c**, Right - left P-EN1 bridge activity during open-loop optic flow to the left (**b**) and to the right (**c**) at 45^o/s (left column) and 90^o/s (right column) during trials where the fly did not, on average, turn (± 10^o/s) in response to the optic flow stimulus. **d-e**, Same as **b-c**, for P-EN2 neurons. **f-i**, Same as **b-e**, except trials were only included if the fly turned with the direction of optic flow (>10^o/s in the direction of optic flow). The mean and s.e.m. across trials are shown. For display, the stimulus position was nulled at time zero to highlight the movement of the stimulus. In trials where flies turned with the direction of optic flow, the direction of visual motion experienced on their retinas is opposite to that expected if the visual motion were in closed-loop. This condition would lead to visual and proprioceptive/efference copy inputs with opposite signs into the P-EN bridge asymmetry. That I observe a weaker asymmetry in **f-l** compared to **b-e** argues that these two inputs (likely alongside vestibular inputs) are somehow combined to generate the P-EN bridge asymmetry.

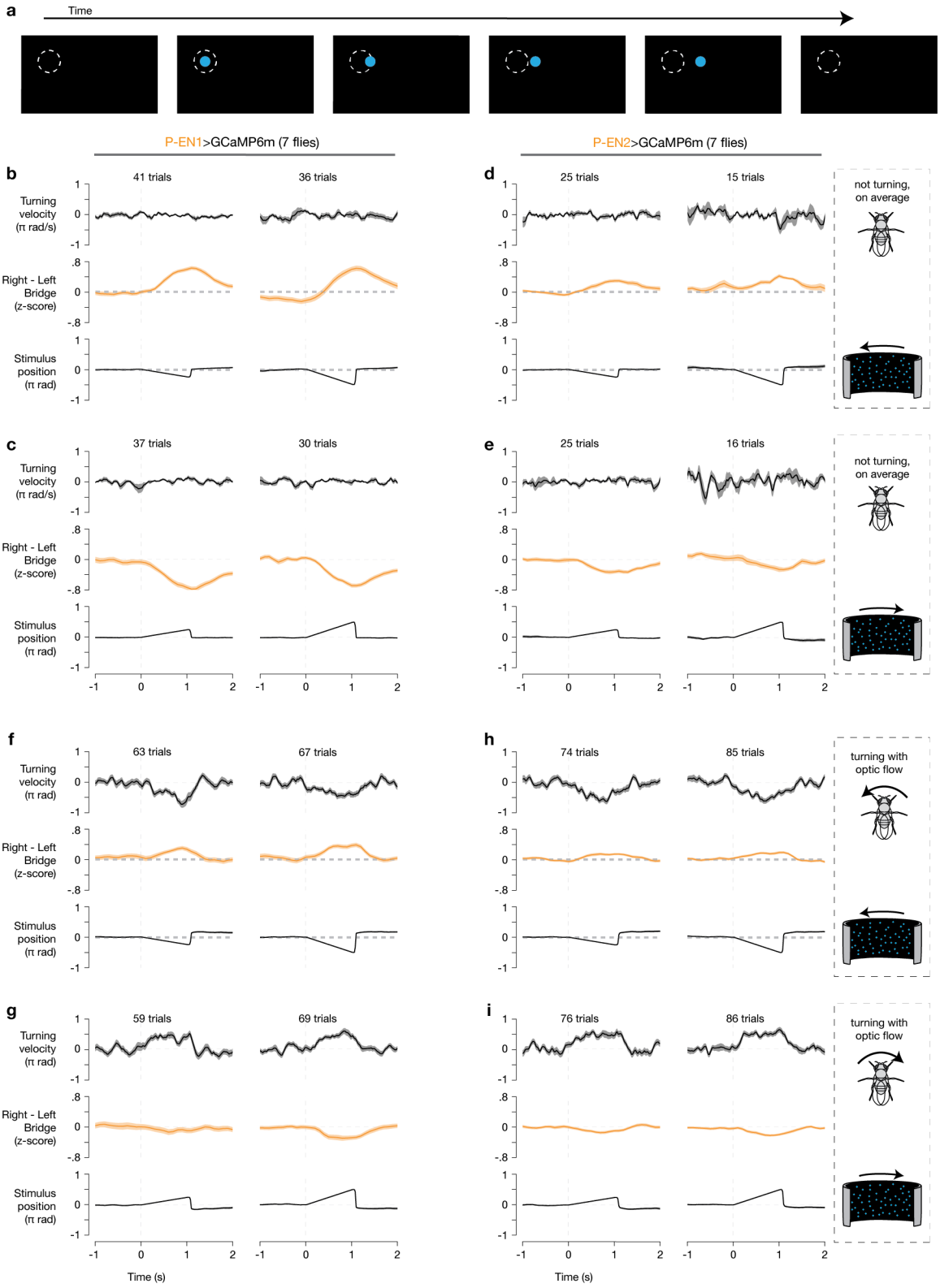
a
Time
P-EN1>GCaMP6m (7 flies)
P-EN2>GCaMP6m (7 flies)
b
41 trials
36 trials
d
25 trials
15 trials
not turning, on average
c
37 trials
30 trials
e
25 trials
16 trials
not turning, on average
f
63 trials
67 trials
h
74 trials
85 trials
turning with optic flow
g
59 trials
69 trials
i
76 trials
86 trials
turning with optic flow
Turning velocity (π rad/s)
Turning velocity (π rad)
Right - Left Bridge (z-score)
Stimulus position (π rad)
Time (s)

Spatiotemporal relationships across cells

A second prediction of the anatomical model in Figure 3.5a-d is that E-PG and P-EN activity peaks should occupy similar positions in the bridge. I therefore imaged E-PGs simultaneously with either P-EN1s or P-EN2s, with E-PGs expressing GCaMP6f (T.-W. Chen et al. 2013), and P-ENs expressing jRGECO1a, a red-shifted calcium indicator (Dana et al. 2016) (Figure 3.9, see Methods). In the bridge, I observed that the calcium peaks from both P-EN lines shift in unison with E-PGs (Figure 3.9a-d). However, the two P-EN lines differed greatly in that P-EN1 and E-PG peaks are in phase with each other (Figure 3.9a,c), whereas, surprisingly, the P-EN2 and E-PG peaks are nearly in antiphase (Figure 3.9b,d) (see Methods for averaging bridge signals after phase nulling). Anatomical experiments argued that I imaged genuine P-ENs in both Gal4 lines (Figure 3.6g-l , Table 3.1), but that the P-EN1 and P-EN2 Gal4 lines target different subsets of P-ENs (Figure 3.10). It is due to these physiological and anatomical differences that I operationally defined two P-EN subtypes: P-EN1 and P-EN2.

What are the implications of these in-phase and nearly antiphase activity peaks in the bridge on the interactions between P-ENs and E-PGs? Since P-ENs likely output (directly or indirectly) onto E-PGs in the ellipsoid body (Wolff, Iyer, and Rubin 2015; Lin et al. 2013) (Figure 3.6e-f), I replotted the mean GCaMP signal measured from each bridge glomerulus (Figure 3.9c-d) over the appropriate tile in the ellipsoid body (Figure 3.9e-f), using the anatomical

mappings described above (Wolff, Iyer, and Rubin 2015) (Figure 3.6a-d). For E-PGs, the two peaks in the bridge map to a single peak in the ellipsoid body (Figure 3.9e,f, blue curves), as expected (Seelig and Jayaraman 2015). However, the two P-EN peaks in the bridge map to either side of the single E-PG peak in the ellipsoid body (Figure 3.9e,f, orange curves) because of their offset anatomy (Figure 3.5a). Furthermore, the positions of these P-EN peaks are inverted across the two P-EN subtypes: the right bridge peak maps to the left flank of the E-PG ellipsoid body-peak for P-EN1 (Figure 3.9e, dashed orange curve) but to the right flank for P-EN2 (Figure 3.9f, dashed orange curve). The reverse is true for the left bridge peak in each cell type.

To evaluate whether these projected activity patterns match the actual patterns in the ellipsoid body, I performed dual imaging from E-PGs and either P-EN1s or P-EN2s in the ellipsoid body. With E-PGs, I observed a single, sharp peak in the ellipsoid body (Figure 3.9i-l), as expected (Seelig and Jayaraman 2015). With P-ENs, I had the null expectation, based on summing the left and right bridge signals after projecting to the ellipsoid body, that I would observe a broad GCaMP peak for P-EN1 and a broad valley for P-EN2 at the position of the E-PG peak (Figure 3.9g,h). Surprisingly, however, P-ENs in both lines also showed a single sharp peak in the ellipsoid body, which overlapped with the E-PG peak (Figure 3.9i-l).

Since the E-PG and P-EN activity peaks looked so similar in dual imaging experiments in the ellipsoid-body, and also because the shape of the GCaMP

peaks in P-EN axonal terminals in the ellipsoid body did not match our expectations based on having imaged their dendrites in the protocerebral bridge, we were concerned that the P-EN signals in ellipsoid-body dual imaging experiments might have reflected a bleed through artefact of signals from the E-PG channel. I therefore performed control experiments where I imaged single cell classes in both the bridge and ellipsoid body at the same time, by capturing a larger imaging volume that encompassed both structures. These experiments revealed the same positions of peaks for E-PG, P-EN1 and P-EN2 cell classes in the bridge and ellipsoid body as predicted from the dual imaging experiments, thus arguing against our dual-imaging results being due to bleed through between indicator channels (Figure 3.11).

The results on Figure 3.9i-l thus argue that broad P-EN1 and P-EN2 calcium signals are reshaped by presynaptic modulation in the ellipsoid body, the mechanism for which should be investigated in future work. Despite this reshaping, I nevertheless observed an asymmetry in P-EN activity relative to the E-PG peak in the ellipsoid body (hereafter referred to as the *ellipsoid body asymmetry*) when the fly turned (Figure 3.9m-p, see Methods). Specifically, P-EN1 activity increased on the leading edge of the moving E-PG peak (Figure 3.9m,o) and P-EN2 activity increased on the trailing edge (Figure 3.9n,p), consistent with the sign of the bridge asymmetry during turns (Figure 3.5h-i,k-l), the relative phase of P-EN1 and P-EN2 to E-PG activity in the bridge (Figure

3.9c-d), and the known anatomical mappings of P-ENs and E-PGs between the bridge and ellipsoid body (Figure 3.9e-f).

Since GCaMP and jRGECO1a (the two calcium indicators used for dual imaging) have different kinetics, it was possible that the asymmetries observed in Figure 3.9m-p were artefacts of one indicator changing faster than the other—even if the changes in [Ca^{2+}] occurred at the same rate in all cell classes—when the heading signal rotated around the ellipsoid body. The fact that P-EN1s lead the E-PGs and P-EN2s trail the E-PGs, however, speaks against this sort of explanation, since in both cases P-ENs expressed jRGECO1a and E-PGs expressed GCaMP6f. Moreover, I performed control experiments where I imaged GCaMP6f and jRGECO1a both co-expressed in the same cells, E-PGs, and I did not observe an obvious lead or lag in the calcium signal measured from either indicator, arguing against these results being due to different indicator kinetics (Figure 3.11). Finally, I note that the ellipsoid body asymmetry is not specific to the lag times chosen for the data in Figure 3.9m-p, but is also present at other lag times relative to the fly behaviorally turning (Figure 3.12).

Figure 3.9 | The P-EN1 activity peak leads, and the P-EN2 peak trails, a rotating E-PG peak in the ellipsoid body, as predicted by their activity in the bridge.

a-b, Co-imaging E-PGs (GCaMP6f) with P-EN1s (**a**) or P-EN2s (**b**) (jRGECO1a) in the bridge in constant darkness. **c-d**, Phase-nulled signals in the bridge, averaged over time. **e-f**, Bridge data from **c-d** replotted onto the ellipsoid body using each cell type's anatomical projection pattern (Wolff, Iyer, and Rubin 2015). **g-h**, Sum of the left- and right-bridge curves in **e-f** (scales adjusted). **i-j**, Co-imaging E-PGs with P-EN1s or P-EN2s in the ellipsoid body. **k-p**, Phase-nulled signals in the ellipsoid body averaged over when the fly was walking straight (**k-l**), turning left (**m-n**) or turning right (**o-p**). Arrows indicate the velocity of the peaks. The P-EN ellipsoid body asymmetries were significantly different during turning and walking straight ($p<0.02$), and during turning left and right ($p<0.01$). The mean and s.e.m. across flies are shown. **c-h** and **k-p** are averaged over bar and dark conditions.

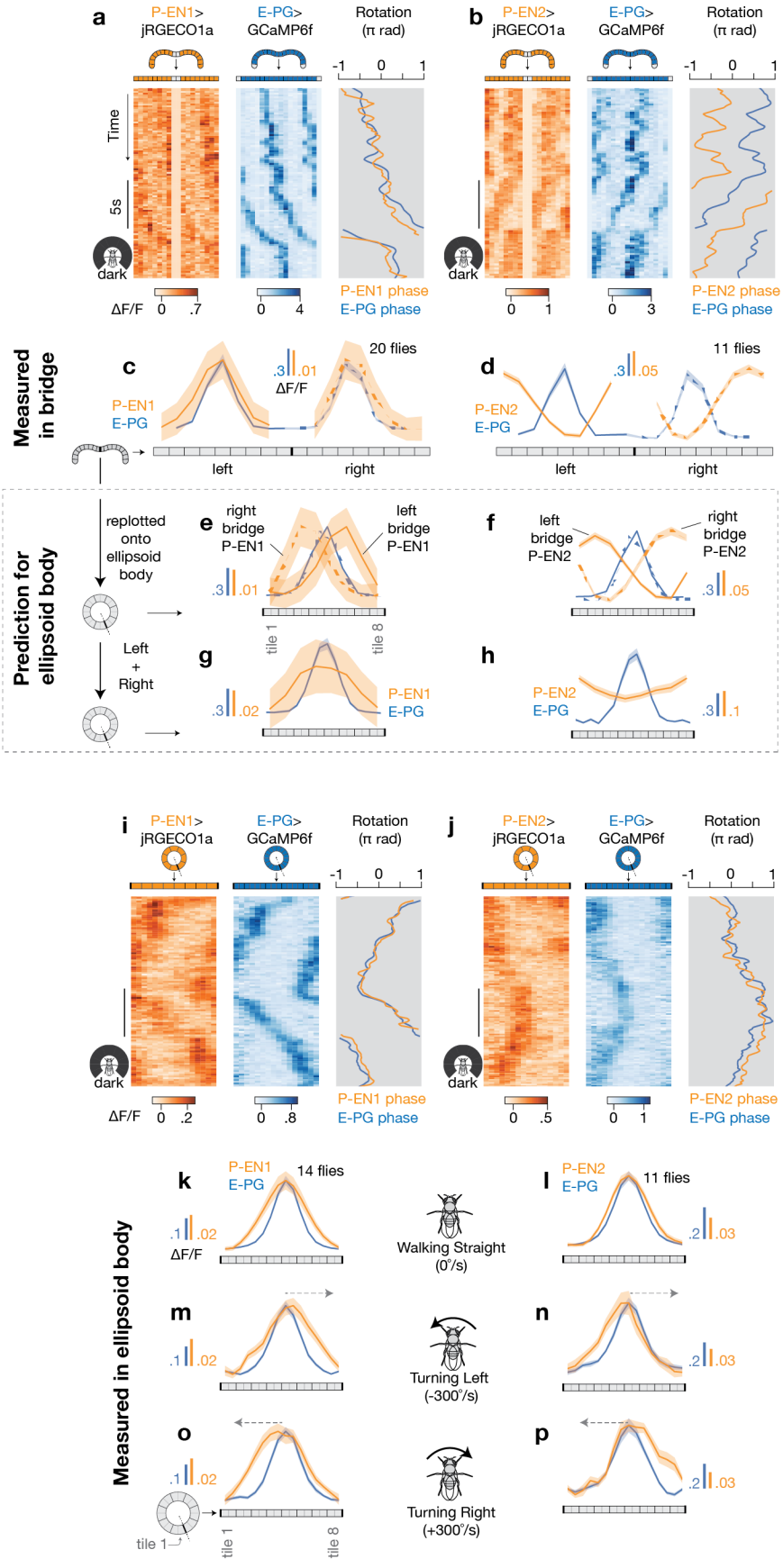
a
P-EN1>
jRGECO1a
E-PG>
GCaMP6f
Rotation
(π rad)
-1 0 1
Time
5s
dark
ΔF/F 0 .7
0 4
P-EN1 phase
E-PG phase
b
P-EN2>
jRGECO1a
E-PG>
GCaMP6f
Rotation
(π rad)
-1 0 1
dark
0 1
0 3
P-EN2 phase
E-PG phase
Measured in bridge
c
20 flies
.3 .01
ΔF/F
P-EN1
E-PG
left
right
d
11 flies
.3 .05
P-EN2
E-PG
left
right
Prediction for ellipsoid body
replotted onto ellipsoid body
e
right bridge P-EN1
left bridge P-EN1
.3 .01
tile 1
tile 8
f
left bridge P-EN2
right bridge P-EN2
.3 .05
Left + Right
g
.3 .02
P-EN1
E-PG
h
P-EN2
E-PG
.3 .1
i
P-EN1>
jRGECO1a
E-PG>
GCaMP6f
Rotation
(π rad)
-1 0 1
dark
ΔF/F 0 .2
0 .8
P-EN1 phase
E-PG phase
j
P-EN2>
jRGECO1a
E-PG>
GCaMP6f
Rotation
(π rad)
-1 0 1
dark
0 .5
0 1
P-EN2 phase
E-PG phase
Measured in ellipsoid body
k
P-EN1
E-PG
14 flies
.1 .02
ΔF/F
Walking Straight
(0°/s)
l
P-EN2
E-PG
11 flies
.2 .03
m
.1 .02
Turning Left
(-300°/s)
n
.2 .03
o
.1 .02
tile 1
tile 1
tile 8
Turning Right
(+300°/s)
p
.2 .03

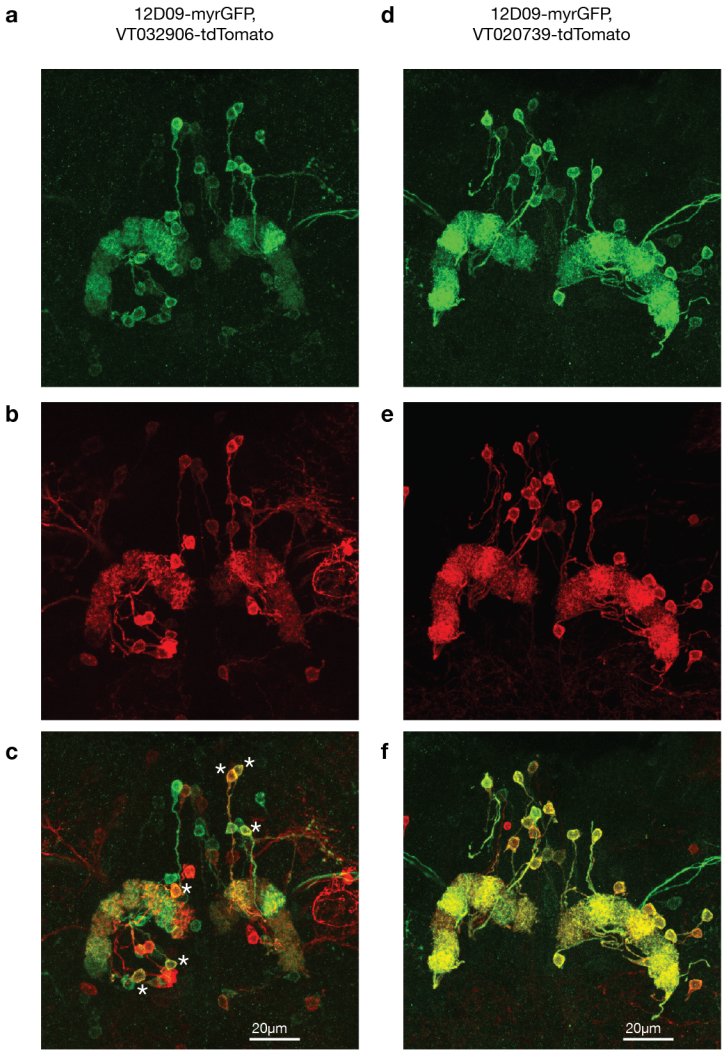

Figure 3.10 | Co-labeling of P-EN1 and P-EN2 driver lines.

a-c, Maximum z-projection of a brain with 12D09-driven neurons expressing GFP and VT032906-driven neurons expressing tdTomato. **a**, GFP (12D09) signal. **b**, tdTomato (VT032906) signal. **c**, Composite of **a** and **b**. Based on physiological experiments, VT032906 primarily labels P-EN1 neurons, whereas 12D09 primarily labels P-EN2 neurons (Figure 3.9, Figure 3.11b,d). As expected, most P-EN neurons are primarily labeled by one of the two drivers, however some neurons are labeled by both (examples denoted with asterisks). **d-f**, Same as **a-c**, except with VT020739-driven neurons expressing tdTomato. Based on physiological experiments, both 12D09 and VT020739 primarily label P-EN2 neurons (Figure 3.9, Figure 3.11c-d). As expected, almost all labeled P-EN neurons are labeled by both P-EN2 drivers.

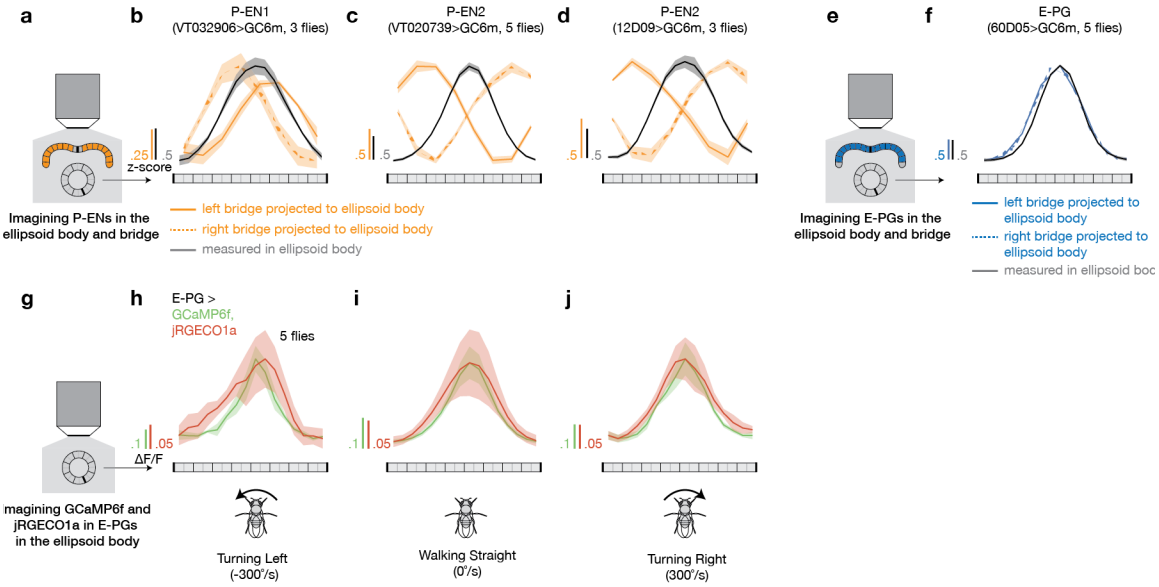

Figure 3.11 I Simultaneous imaging of the protocerebral bridge and ellipsoid body for each cell type separately and dual-color imaging of GCaMP6f and jRGECO1a in E-PGs in the ellipsoid body.

a, I imaged the bridge and ellipsoid body in the same fly, at the same time, using a tall z-stack that encompassed both structures, to determine the relationship between the signals measured in each structure. **b**, Phase-nulled P-EN1 signals measured in the bridge (orange) and ellipsoid body (grey). The signals measured in the bridge were replotted onto the ellipsoid body using the P-EN projection pattern. **c-d**, Same as **b**, for P-EN2 signals from VT020739-Gal4 (**c**) and 12D09-Gal4 (**d**). **e**, Diagram as in **a**, except for imaging E-PGs, with the bridge in blue. **f**, Same as in **b**, for E-PGs, with the left and right bridge in blue. In **b-d**, **f**, the mean and s.e.m. across flies are shown (in **f,** the s.e.m. for the bridge curves (blue) are omitted for clarity). Both the bridge and ellipsoid body signals are nulled using the ellipsoid body phase. Note that the positions of the left- and right-bridge peaks are inverted between P-EN1 and P-EN2. These results are consistent with the dual imaging experiments in Figure 3.9, and argue that the results in Figure 3.9 were not due to crosstalk between the red and green channels. **g**, Schematic illustrating imaging from the ellipsoid body. **h-j**, Phase-nulled ellipsoid body signals of GCaMP6f and jRGECO1a co-expressed in E-PGs, computed for when the fly turned left (**h**, -300°/s), walked straight (**i**, 0°/s) or turned right (**j**, +300°/s), 300 ms before the calcium signal, as in Figure 3.9k-p. The mean and s.e.m. across flies are shown. I observed no consistent, strong asymmetries in the jRGECO1a and GCaMP6f signals during left or right turns when both indicators are expressed in E-PGs. These data argue that the asymmetries I observed in dual imaging of P-ENs and E-PGs in the ellipsoid body (Figure 3.9m-p) were not an artifact of indicator kinetics. Data are averaged over bar and dark conditions.

Figure 3.12 | Analysis of the ellipsoid body asymmetry in P-EN1s and P-EN2s relative to E-PGs in the ellipsoid body.

a, Mean E-PG and P-EN1 activity in the ellipsoid body triggered on when the fly was turning to the left (-300 °/s, upper panel) or right (+300 °/s, lower panel), as in Figure 3.9m-p, except over time. The P-EN1 and E-PG signals were phase-nulled using the E-PG phase. **b**, Same as **a**, except for P-EN2 activity. **c-d**, Analyzing the two-color imaging experiments in Figure 3.9i-p, I calculated the cross correlation between the ellipsoid body asymmetry in P-EN1 (**c**) or P-EN2 (**d**) and the E-PG phase velocity in the ellipsoid body. A positive correlation indicates an increased P-EN signal in the direction where the E-PG peak is moving. A positive lag indicates that the P-EN asymmetry comes after the change in the E-PG phase. Thus, the P-EN1 peak tends to lead the E-PG peak whereas the P-EN2 peak tends to lag behind the E-PG peak. Note that I also observe a smaller negative, late peak in the signal driven by the P-EN1 Gal4 and a smaller positive, early peak in the signal driven by the P-EN2 Gal4, suggesting that each Gal4 line contains some number of both P-EN1 and P-EN2 cells, but with more of one than the other. **e-f**, Same as in **c-d**, except the P-EN ellipsoid body asymmetry is correlated with the fly's turning velocity. A positive lag indicates that the P-EN asymmetry comes after the fly turns. Arrows indicate the lag where the mean correlation was greatest. In **c-f**, thin lines represent single flies, thick lines represent the mean across flies. Data are averaged over bar and dark conditions.

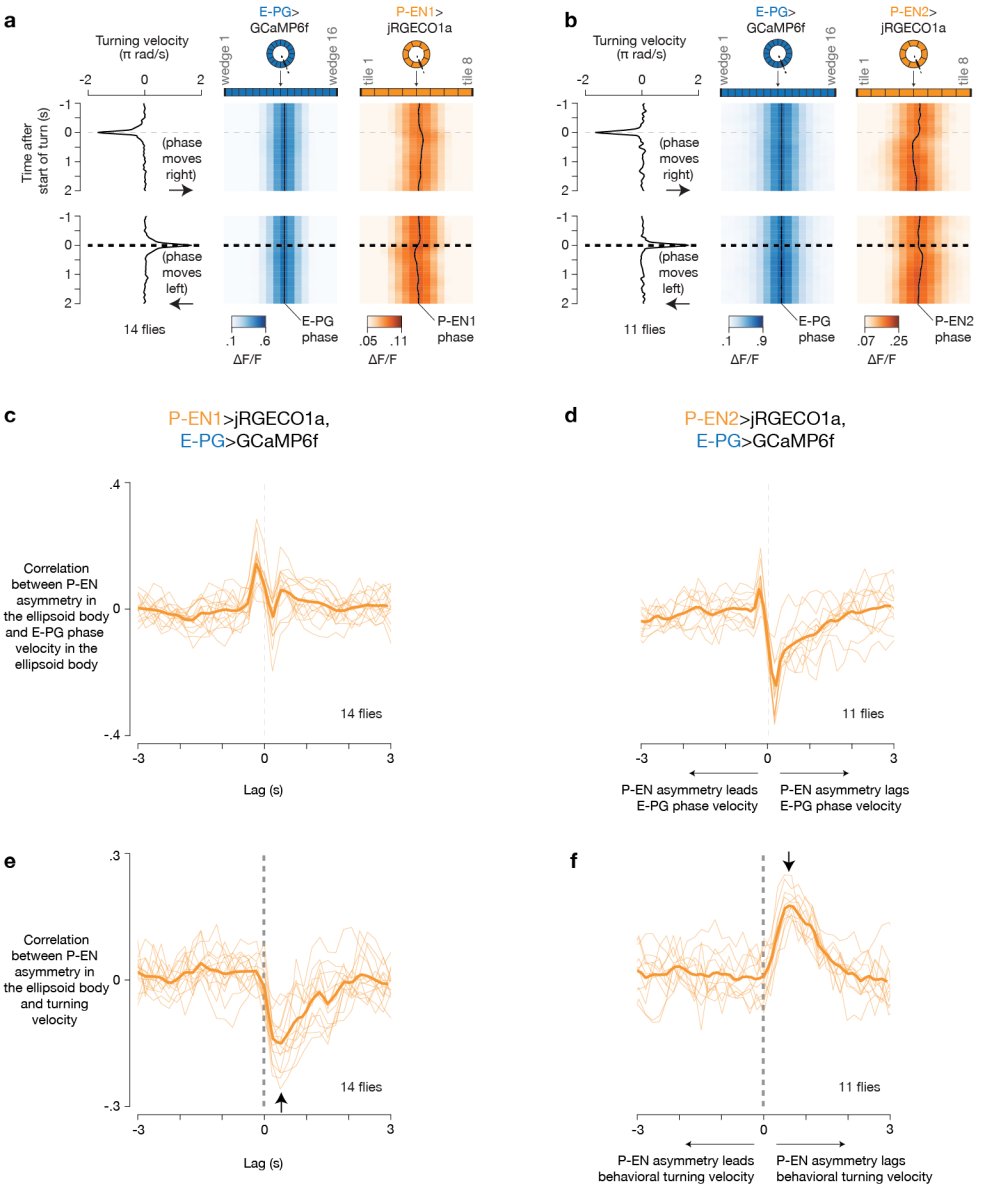
a
Turning velocity (π rad/s)
E-PG> GCaMP6f
P-EN1> jRGECO1a
wedge 1
wedge 16
tile 1
tile 8
Time after start of turn (s)
(phase moves right)
(phase moves left)
14 flies
E-PG phase
P-EN1 phase
ΔF/F
b
Turning velocity (π rad/s)
E-PG> GCaMP6f
P-EN2> jRGECO1a
11 flies
E-PG phase
P-EN2 phase
ΔF/F
c
P-EN1>jRGECO1a, E-PG>GCaMP6f
Correlation between P-EN asymmetry in the ellipsoid body and E-PG phase velocity in the ellipsoid body
14 flies
Lag (s)
d
P-EN2>jRGECO1a, E-PG>GCaMP6f
11 flies
P-EN asymmetry leads E-PG phase velocity
P-EN asymmetry lags E-PG phase velocity
e
Correlation between P-EN asymmetry in the ellipsoid body and turning velocity
14 flies
Lag (s)
f
11 flies
P-EN asymmetry leads behavioral turning velocity
P-EN asymmetry lags behavioral turning velocity

Given that P-EN1 and P-EN2 cells have inverted spatial activity patterns, how are they coordinated in time? I found that when the activity peaks moved in the bridge, the P-EN1 bridge asymmetry was evident early, prior to the onset of the peaks moving, whereas the P-EN2 bridge asymmetry came on late, after the peaks were already moving, as measured by averaging these signals triggered on movements of the peaks (Figure 3.13a-c, see Methods). A cross correlation analysis also showed this timing difference between P-EN1 and P-EN2 in the bridge (Figure 3.13d) and the ellipsoid body (Figure 3.12c-d). I will discuss possible interpretations of these different spatiotemporal activity profiles between P-EN1 and P-EN2 cells later in the chapter, but suffice it to say here that the early right-left asymmetry in P-EN1s and the locations where P-EN1 activity peaks reside in the bridge (overlapping the E-PG peaks) are both entirely consistent with the model proposed in Figure 3.5a-d.

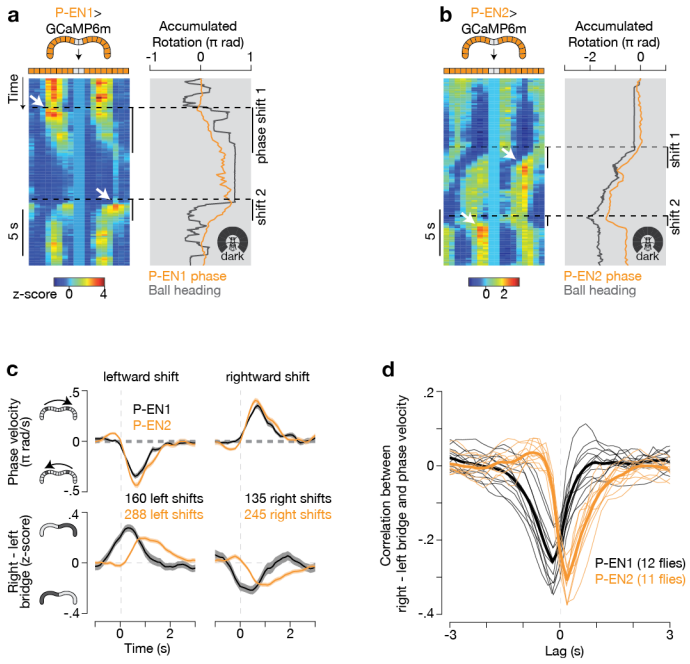

Figure 3.13 | Timing of P-EN1 and P-EN2 bridge asymmetries.

a-b, Bridge activity during phase shifts (vertical black lines) in constant darkness for P-EN1 (**a**) and P-EN2 (**b**). White arrows highlight right-left asymmetries. **c**, Right - left bridge activity (bottom) triggered on long phase changes (top). The mean and s.e.m. across phase shifts are shown. **d**, Correlation between right - left bridge activity and phase velocity vs time lag between the two signals. Thin lines represent single flies. Thick lines represent the mean across flies. **c-d** are averaged over bar and dark conditions. Note the different rotation scales in **a-b**.

Blocking P-ENs impairs integration

If P-EN neurons serve an important role in moving the E-PG peak, then impeding P-EN synaptic output should impair the ability of the E-PG peak to properly update its position when the fly turns. I expressed *shibire^{ts}*, which prevents synaptic vesicle recycling in a temperature dependent manner (Poodry and Edgar 1979), in each P-EN line, and measured E-PG activity in the bridge using GCaMP6f (Figure 3.14). When I impeded P-EN synaptic output by bringing the bath temperature to 32ºC (see Methods), the E-PG signal failed to consistently track the dynamics of the fly's heading in the dark (Figure 3.13b, black arrows, c-d, see Methods). Note that at 34ºC, the E-PG signal appeared dim or blurred, indicating a stronger effect, but which made it difficult to properly estimate the E-PG phase. I therefore performed the experiments at 32ºC, expecting that P-ENs are only partially impaired. Moreover, I did not measure a consistent impairment on the ability of the E-PG phase to track a closed-loop bar in the same flies (Figure 3.15a-d). These experiments argue that proper synaptic transmission in P-ENs is specifically necessary for this circuit's ability to integrate the fly's heading without a visual landmark (i.e., perform angular integration).

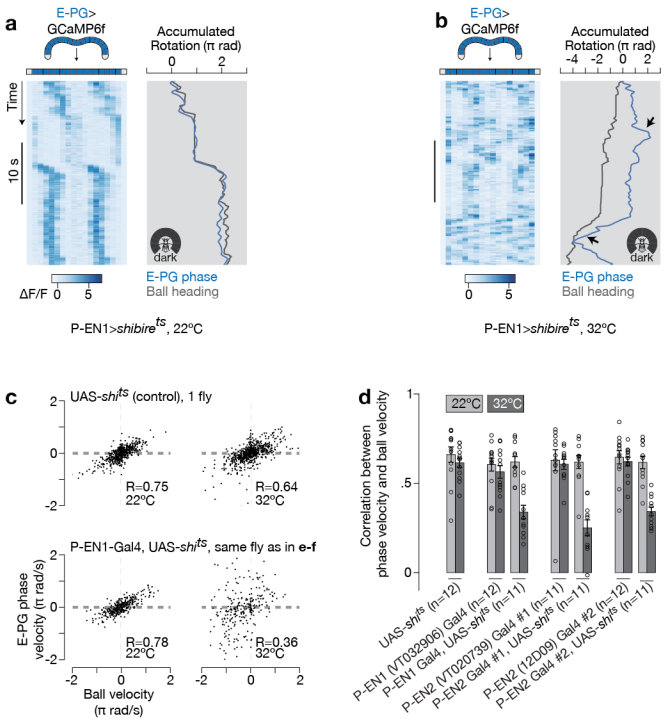

Figure 3.14 | The effect of blocking P-EN synaptic transmission on the E-PG phase in the dark.

a-b, E-PG activity in the bridge with P-EN1 cells expressing *shibire*^{ts} at 22ºC (**a**) and at 32ºC (**b**). Arrows highlight atypical deviations in the E-PG phase from the ball's heading at 32º. **c**, E-PG phase velocity vs ball velocity in a control and P-EN1>*shibire*^{ts} fly in constant darkness. R: Pearson correlation coefficient. **d**, Correlations of data in **c**, for three P-EN-Gal4 lines. Each circle represents one fly. The mean and s.e.m. across flies are shown. The cold-to-hot changes in correlation are significantly different between P-EN>*shibire*^{ts} and control groups ($p<0.01$). Note the different rotation scales in **a-b**.

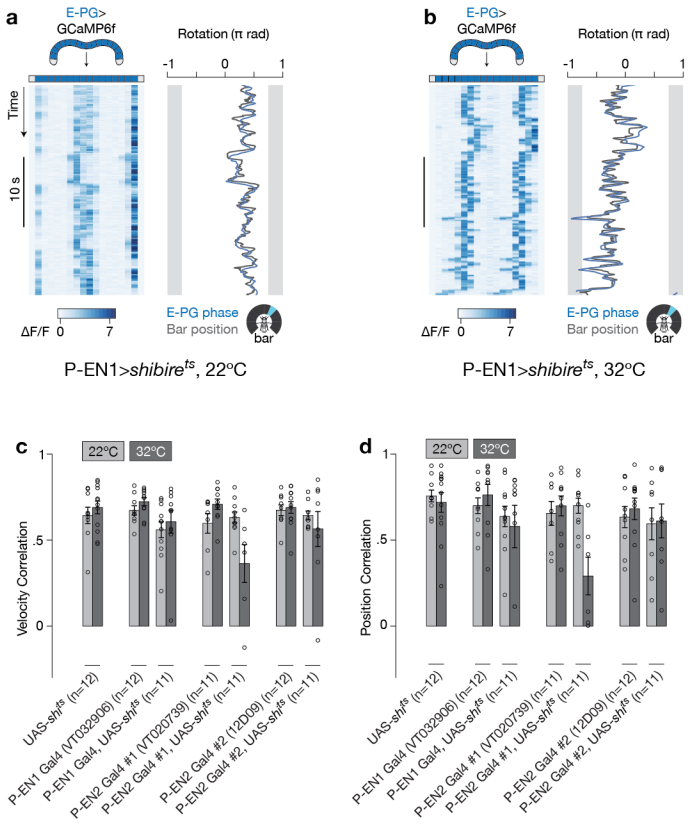

Figure 3.15 | The effects of blocking P-EN synaptic transmission on the ability of E-PGs to track a landmark.

a-b, E-PG activity in the bridge from the same fly as in Fig. 4e-f (P-EN1>*shibire*^{ts}), except with a closed-loop bar, at 22ºC (**a**) and at 32ºC (**b**). **c**, Correlations between phase- and bar-velocity, for three P-EN-Gal4 lines driving *shibire*^{ts}, with parental controls. Each circle represents one fly. The mean and s.e.m. across flies are shown. **d**, Same as **c**, except plotting circular correlations between phase and bar position. Only data where the bar was visible in the front 270º of the arena were used for calculating correlations. Trials where the bar was visible for less than 10 s were excluded, with some flies having no trials passing this criterion. The total number of flies (without excluding flies that did not pass the above criterion) for each genotype is shown. The mean and s.e.m. across included flies are shown. Only VT020739-Gal4 seems to affect the ability of the E-PG signal to track a visual landmark, suggesting that perhaps this effect is due to non-P-EN neurons targeted by this line, for example visual lobe neurons, or that this effect requires the stronger Gal4 expression in P-ENs in this line.

Activating P-ENs shifts E-PG activity

Is an experimentally induced asymmetry in P-ENs sufficient to shift the E-PG activity peak in the expected direction? I stimulated P-ENs, with 1-2 glomeruli resolution, on the left or right bridge by expressing the ATP-gated cation channel $P2X_2$ (Zemelman et al. 2003) and locally releasing ATP from a pipette (see Methods), while measuring E-PG activity in the bridge using GCaMP6f (Figure 3.16a-c). When I locally excited P-ENs in the left bridge, the E-PG peaks appeared (on both sides of the bridge) to the right of the stimulated glomerulus, and vice versa when P-ENs were excited on the right bridge (Figure 3.16d-i), for both P-EN1 and P-EN2 Gal4 lines. These stimulation data are consistent with an excitatory relationship (direct or indirect) between P-ENs and E-PGs, which is also consistent with P-ENs being immunoreactive for choline acetyltransferase (ChAT) (Figure 3.18) (acetylcholine is the primary excitatory transmitter in the central nervous system of flies). Given that P-EN2 activity is normally anti phase relative to P-EN1s, the same bridge asymmetry in P-EN1s and P-EN2s would thus be expected to produce opposing movements on the E-PG phase (Figure 3.16d-g). Control experiments without ATP and without Gal4 argue that I specifically stimulated P-ENs (Figure 3.17e-j). These experiments demonstrate that inducing a strong asymmetry in P-ENs shifts the E-PG activity peak in the expected direction relative to the stimulated glomerulus.

Remarkably, I noticed that the fly occasionally performed a behavioral turn immediately after the local release of ATP (e.g., Figure 3.16d-g, asterisks). To

quantify this effect, I parsed each stimulation event based on whether the phase moved left or right in the bridge (as measured 250 ms after the ATP pulse), and computed the average turning velocity of the fly in each case, time-locked to the time of stimulation (Figure 3.19a-c). Normally, the phase moves right when the fly turns left (Figure 3.19c, triggered on movements of the phase regardless of stimulation in the same flies, see Methods for Culling individual turns or phase shifts). However, during stimulation, as the phase moved right, the fly turned *right* (Figure 3.19), as if to return the E-PG phase to its original position just prior to stimulation (the E-PG phase was momentarily controlled by the stimulation and therefore could not return to its original position, see Figure 3.16 asterisks). This interpretation implies that the fly reacts to the change in phase. Indeed, the change in phase *precedes* the fly's turn during stimulation events, as measured by a cross-correlation (Figure 3.19d-e, using time points within a 0-1 s window after each ATP pulse), in contrast to the normal sequence of events where the phase updates after the fly's movements (Figure 3.19f, using time points outside the 0-1 s window after each ATP pulse). To compute the correlation at each time lag, the behavioral turning data was shifted by the appropriate time lag relative to the phase velocity imaging data (see Methods for Comparing data acquired at different sampling frequencies). These effects are not apparent with no ATP in the pipette, if the Gal4 transgene is not present, or if the same data are parsed based on whether the left or right bridge was stimulated (data not shown). This

analysis provides the first indication of how the fly's heading signal influences its turning behavior.

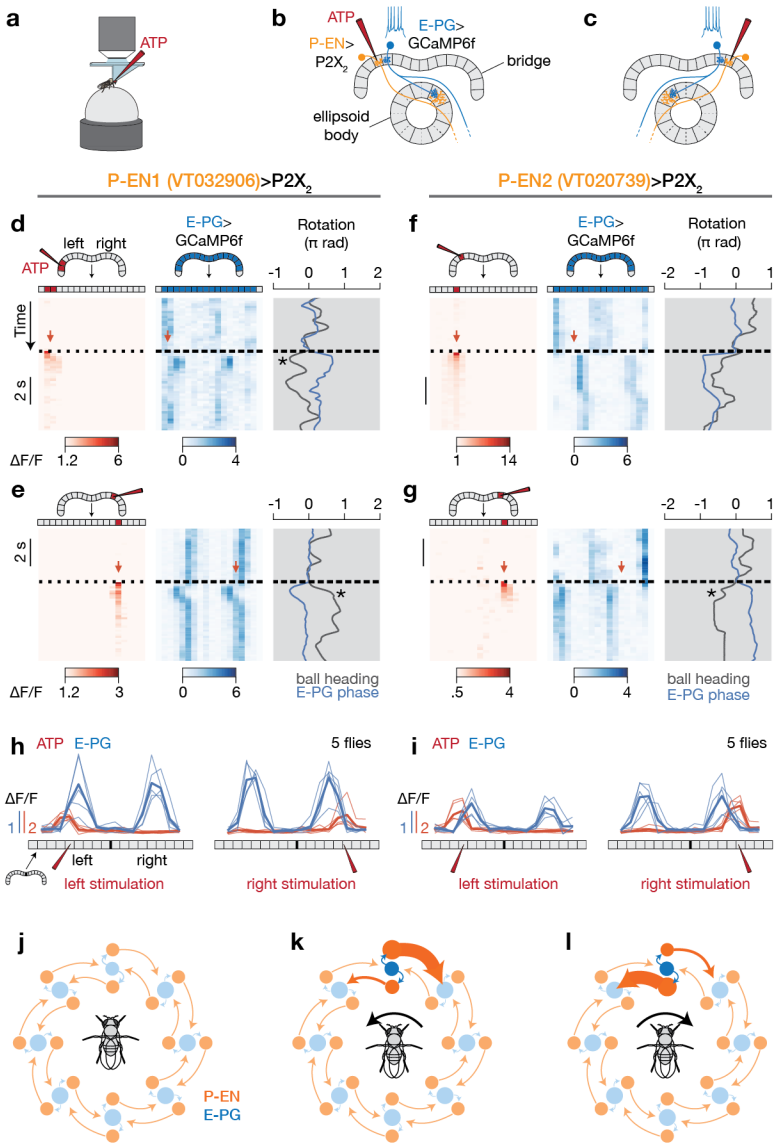

Figure 3.16 | P-EN neurons medially excite E-PG neurons in the bridge, consistent with a model for neural integration.

a, An ATP-filled pipette is inserted into the brain. **b-c**, Stimulating $P2X_2$-expressing P-ENs in the bridge is expected to excite E-PGs in the medial neighboring glomerulus. **d-e**, E-PG bridge activity while stimulating P-EN1 neurons in the left (**d**) or right (**e**) bridge. **f-g**, Same as **d-e**, for P-EN2 neurons. **h-i**, Phase-nulled E-PG activity after P-EN1 (**h**) or P-EN2 (**i**) stimulation. Thin lines represent the mean response in each fly. Thick lines represent the mean across flies. Asterisks highlight events when the fly turned against the movement of the E-PG phase. See Methods for details. **j**, Summary model: P-EN and E-PG interactions projected onto a single ring. Only ellipsoid body tiles are represented for clarity. **k-l**, Same as **j**, highlighting P-ENs that are active when the fly turns left (**k**), or right (**l**).

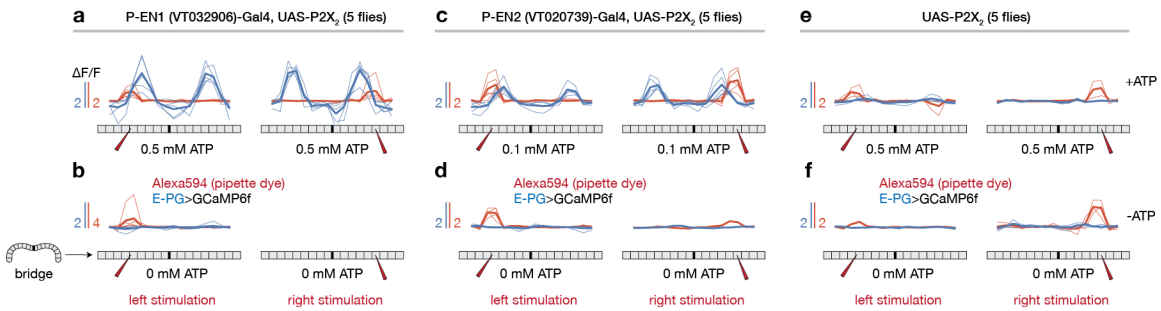

Figure 3.17 I Controls for the P2X$_2$ experiments.

a, The change in the phase-nulled E-PG>GCaMP6f and ATP (Alexa594) signals during an ATP pulse, with P-EN1s expressing P2X$_2$. I subtracted the average E-PG signal at -0.3 to 0.0s from the average at 0.7 to 1.0s with respect to the time of the pressure pulse, highlighting the effect of the stimulation. I subtracted the average Alexa594 (ATP) signal at -0.3 to 0.0 s from the average immediately (1 frame) after stimulation. The irregular dips in the E-PG signal are due to the fact that the E-PG phase was not uniformly distributed immediately before stimulation. Both signals were phase-nulled using the position of the pipette. **b**, Same as **a**, except without ATP in the same flies. **c-d**, Same as **a-b**, except with P-EN2s expressing P2X$_2$. **e-f**, Same as **a-b**, except with no Gal4 as a control for the specificity of P2X$_2$ expression. Thin lines represent single flies, and thick lines represent the mean across flies.

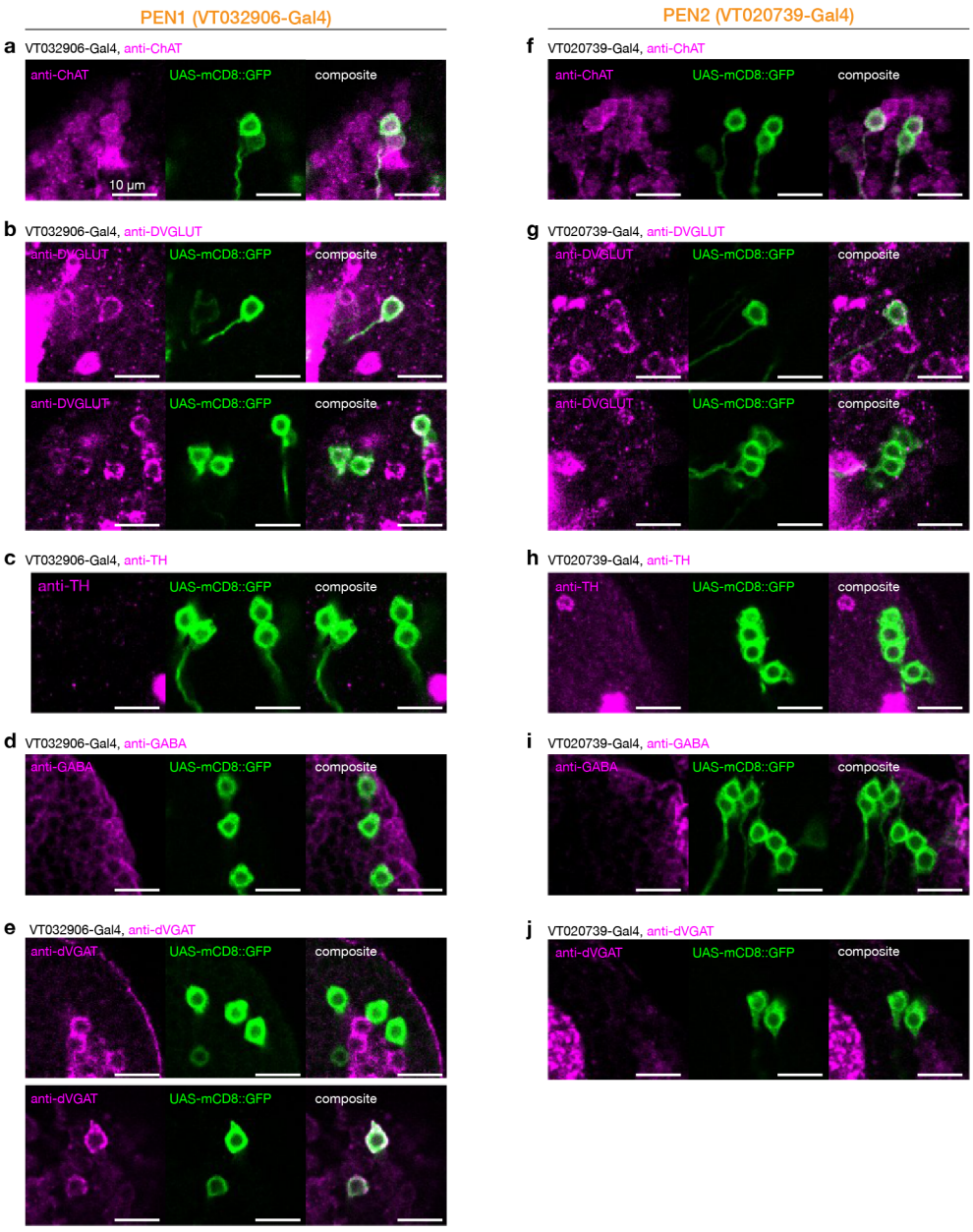

Figure 3.18 | Immunoreactivity for neurotransmitter markers in P-EN1 and P-EN2.

a-j, Co-labeling of VT032906-Gal4 (P-EN1, **a-e**) and VT020739-Gal4 (P-EN2, **f-j**) neurons in green with anti-ChAT (**a,f**), anti-DVGLUT (**b,g**), anti-tyrosine hydroxylase (anti-TH, **c,h**), anti-GABA (**d,i**) and anti-dVGAT (**e,j**) in magenta. Both P-EN lines are positive for ChAT. VT032906-Gal4 (P-EN1) seems to also have vGlut-positive P-ENs.

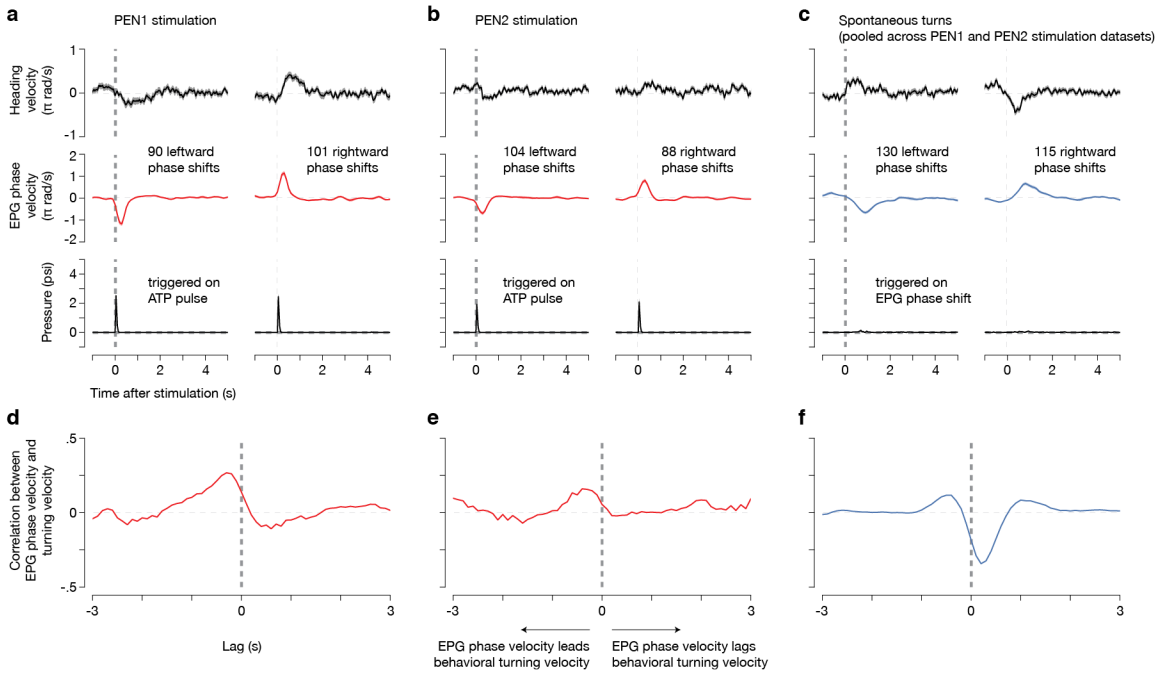

Figure 3.19 | Flies turn in response to a stimulated change in the heading signal.

a, Turning velocity and E-PG phase velocity triggered on P-EN1 focal stimulation, when the E-PG phase shifted left (left panel) or right (right panel) immediately after the ATP pulse. **b**, Same as **a**, for P-EN2 stimulation. **c**, Same as **a**, except triggered on the E-PG phase velocity, regardless of stimulation. Pooled from same recordings as P-EN1 and P-EN2 stimulation. Mean and s.e.m. across ATP pulses (**a-b**) or phase shifts (**c**) are shown. **d**, Cross-correlation between E-PG phase velocity and turning velocity during P-EN1 stimulation (1 s window after ATP pulse). **e**, Same as **d**, for P-EN2 stimulation. **f**, Same as **d**, except for all other time points (*not* within 1 s window after ATP pulse). Pooled from same recordings as P-EN1 and P-EN2 stimulation.

Discussion

Working Model

My working model for how the central complex heading system updates during a right turn in the dark is as follows (see Figure 3.5a-d, Figure 3.16j-l). The fly sends a motor command to the legs to turn right, causing the fly (or ball, as measured in our system) to start turning. A few hundred milliseconds later, turning-related signals arrive to the protocerebral bridge, driving higher activity in P-EN1 dendrites in the right bridge compared to the left. This elevated activity in right-bridge P-EN1 dendrites drives elevated activity in their axons, on the counterclockwise edge of the E-PG activity peak in the ellipsoid body, causing the E-PG peak to rotate counterclockwise. The opposite sequence of events rotates the E-PG peak clockwise during a left turn. This model also requires additional inhibitory circuitry to maintain the width of the E-PG peak in the face of spreading E-PG activity due to P-EN excitation.

Sources of the turning-related bridge asymmetry

The P-EN bridge asymmetry is likely driven by multiple signals informative of the fly rotating. For example, this asymmetry is evident when the fly turns in the dark (Figure 3.7), suggesting that it is driven by proprioceptive feedback or an efference copy of the motor command to turn. In addition, this asymmetry can also be driven by visual motion (Figure 3.8) and perhaps vestibular inputs, which were not present in our experiments since the fly never actually rotated. Neurons

that could bring asymmetric signals into the left and right bridge, to drive an asymmetry in P-ENs, have been anatomically identified (Figs. 3R & 18D-F and Figs. 3S & 18A in Wolff et al. 2015).

Potential roles for P-EN1s and P-EN2s

Whereas previous models for angular integration (Skaggs et al. 1995; K. Zhang 1996; Redish, Elga, and Touretzky 1996; Sharp, Blair, and Brown 1996; McNaughton et al. 2006) have only required P-EN1-like neurons, I observe a second set of asymmetrically active neurons (P-EN2) biased to the trailing edge of the ellipsoid body E-PG peak, typically expressing asymmetric activity a couple hundred milliseconds after the rotation of the heading signal. A parsimonious interpretation of this result is that, given their relative timing, the early, P-EN1 cells start the movement of the E-PG peak, like a gas pedal, and the late, P-EN2 cells stop its movement, like a brake. However, interpreting the P-EN2 asymmetry as a brake implies that a moving E-PG peak would otherwise continue rotating – a property not featured in models of the rodent head-direction system (Skaggs et al. 1995; K. Zhang 1996; Redish, Elga, and Touretzky 1996; Sharp, Blair, and Brown 1996; McNaughton et al. 2006). Another interpretation is that P-EN1s are the main drivers of angular integration, whereas P-EN2s serve a different role. Note that the shape of the P-EN1 peaks are relatively sharp, like that of the E-PG peaks, whereas the P-EN2 peak are broader. Indeed, the P-EN2 signal closely approximates a sinusoid along the bridge (Figure 3.9d). A

sinusoidal signal may contribute to trigonometric vector computations, for example if combined with the animal's speed. Finally, note that P-EN1 signals tended to be weak except when the flies were turning (leading to high variance in bridge signals when the flies walked straight, Figure 3.9c), whereas P-EN2 signals were more persistently active, even during straight-walking periods. Together, these observations may help pinpoint the functional differences between these cells classes (also see section below for how P-EN2s might participate during directed walking). Further work will be needed to rigorously test such functional hypotheses for P-EN1s and P-EN2s.

Limiting the effects of noise on integration

One limitation of integration models is that noise in the system leads to drift in the integrated signal over time. Experimentally, we observe drift in the E-PG heading signal when the fly walks in the dark (Figure 3.5). An interesting point related to this observation is that the situation may be qualitatively different when the fly is standing compared to when it is walking. When the fly is walking, E-PG and P-EN neurons receive a bilateral boost in activity compared to when the fly is standing (Figure 3.20, see Methods). This boost in activity saturates at low walking speeds, suggesting that it represents a binary standing or walking signal, as opposed to a quantitative signal for forward velocity (Figure 3.20b,f,j). The right – left bridge asymmetry, on the other hand, is relatively unaffected by forward walking speed (Figure 3.20d,h,l). The bilateral boost in signal strength

during walking compared to standing might be useful in the following way. P-EN1s require both a heading-related phase input (presumably from E-PGs) and an angular-velocity-related asymmetric input to be active (Figure 3.5). Noise in the angular-velocity-related asymmetric input will lead to drift in the E-PG phase, since the asymmetric input will drive variable spike rates in P-EN1s, which will likely lead to variable movements of the E-PG peak. However, if the E-PG input to P-EN1s is significantly decreased when the fly is not walking (as suggested by the data in Figure 3.20b), the same noise in the asymmetric input will drive fewer suprathreshold depolarizations, and therefore fewer action potentials in P-EN1s. Such a mechanism would limit the effect of any noise in the angular-velocity inputs on driving rotations of the heading signal during standing periods specifically. When the system needs to integrate angular heading velocity during walking, however, it seems to boost the P-EN1 activity level. I hypothesize that this boost acts to bring P-ENs closer to action potential threshold so that their synaptic output (driven by their spike rates) begins to match the asymmetric angular-velocity inputs and thus the fly's turning velocity. Put another way, when the fly is walking, its angular velocity is some quantitative value above or below zero and the P-EN1 asymmetry attempts to estimate this value as accurately as possible, with some unavoidable errors. When the fly is standing, however, the central complex heading system can, in principle, assume that the fly's angular velocity is *exactly zero*. By strongly reducing P-EN1 and E-PG activity levels (and presumably their spike rates) the system might achieve a much lower rate of drift

in the E-PG heading estimate. This idea is consistent with the bilateral boost in activity seen in both E-PG and P-EN1 neurons (Figure 3.20b,f). A similar mechanism may operate in P-EN2s (Figure 3.20j), however, their specific role within this circuit is less clear than that of P-EN1s.

Figure 3.20 | Total bridge activity increases during walking.
a, Total (right + left) E-PG bridge activity vs. turning velocity (22.5°/s, or π/8 rad/s bins). **b**, Total E-PG bridge activity vs. forward velocity (0.25 mm/s bins). **c-d**, Same as **a-b**, for right – left E-PG bridge activity. **e-h**, Same as **a-d**, for P-EN1. **i-l**, Same as **a-d**, for P-EN2. Thin lines represent one fly. Thick lines represent the mean across flies. Scales are identical across plots for each metric.

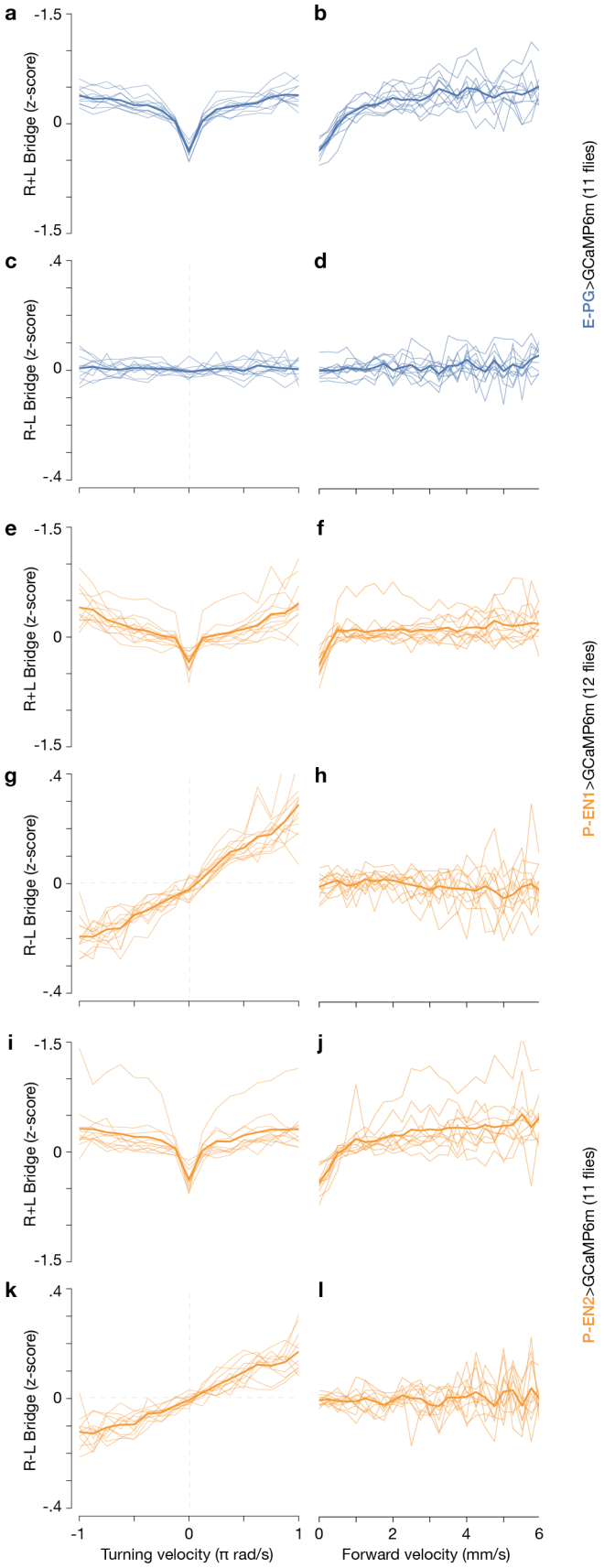
a
b
c
d
e
f
g
h
i
j
k
l
R+L Bridge (z-score)
R-L Bridge (z-score)
-1.5
0
.4
-.4
E-PG>GCaMP6m (11 flies)
P-EN1>GCaMP6m (12 flies)
P-EN2>GCaMP6m (11 flies)
-1
1
2
4
6
Turning velocity (π rad/s)
Forward velocity (mm/s)

The role of compass-like signals in the central complex in relation to behavior.

I observed relatively long (200 to 600 ms) latencies between the ball's rotation and the updating of the phase signal in the central complex in our experiments (see Methods for computing correlations). As a result, we favor the interpretation that the E-PG/P-EN phase, in these conditions, is updated by the flies' locomotor behavior, rather than this phase signal acting like a steering wheel to turn the fly. That said, even if the E-PG/P-EN phase does not directly induce the fly to turn left or right in these experiments, it is likely that flies build internal heading signals so that they can use them to guide navigational behavior under at least some conditions. Interestingly, when I experimentally shifted the E-PG phase in Figure 3.16a-i, the fly occasionally turned in response to this stimulation, and in a direction that would normally bring the E-PG phase back to its original position (in many cases, the E-PG phase remained yoked to a constant position for a few seconds due to the stimulation and therefore could not immediately return to its original position, Figure 3.19). These results suggest that the fly might attempt to maintain a desired heading, as estimated by its E-PG phase, and behaviorally turns to correct any deviation from this desired heading. Indeed, I commonly observed flies to maintain a constant heading angle (i.e. they kept the closed-loop bar near a single, apparently desired, angular position in the arena) for many seconds or minutes (Figure 3.15a-b) rather than perform seemingly random exploration. It is interesting to note that, while attempting to

maintain a constant heading angle, the fly often overshoots its mean or “goal” angle in either direction. Under these circumstances, one might interpret the P-EN2 signal, which occurs late during a turn and has the opposite sign as the P-EN1 signal, as one that is appropriate for returning the E-PG signal in anticipation of the fly making a second, corrective turn back towards the “goal” angle. In this interpretation, P-EN2s might be considered to carry a predictive signal to help rotate the E-PG bolus in the expected upcoming turn direction of the fly, perhaps to compensate for delays associated with updating based solely on sensory inputs like proprioception or optic flow.

Comments on the kinetics observed in E-PG, P-EN1 and P-EN2 neurons

Whereas E-PG, P-EN1, and P-EN2 all showed their peak turn-related activity a few hundred milliseconds after the animal’s turning behavior, their activity in relation to one another, and in relation to the rotation of the E-PG/P-EN phase signal, showed a clear, and tight, temporal structure (e.g., Figure 3.13a-d, Figure 3.12c-d). Specifically, P-EN1 asymmetries arise first, then the E-PG peak starts rotating, then the P-EN2 asymmetries arise as the E-PG peak stops rotating in the initial direction. All this happens a few hundred milliseconds after the fly (ball) moves.

Note that the phase measured from VT032906-Gal4 (P-EN1) was particularly sluggish in tracking the fly’s turning behavior (Figure 3.1h, Figure 3.5e, Figure 3.13a). Specifically, in VT032906>GCaMP6m flies, the phase signal

in the central complex updated (i.e., showed its peak cross-correlation time with behavior) only ~600 ms after the fly turned (see Methods), unlike the ~300 ms latency observed in P-EN2 and E-PG lines. This sluggishness is not interpreted to mean that P-EN1 neurons are physiologically delayed in their activation, by 300 ms, with respect to P-EN2 and E-PG neurons, since when I imaged P-EN1 and E-PG neuron types simultaneously in the same fly (Figure 3.9), the P-EN1 activity peak actually leads the E-PG activity peak during turns (Figure 3.9m,o, Figure 3.12c). Rather, I interpret the slow P-EN1 phase kinetics in our GCaMP6m imaging experiments as supporting a model in which P-EN1 cells normally function to drive the movement of the heading signal in the central complex, but where P-EN1 synaptic kinetics are slowed down due to the calcium buffering effects of high GCaMP6m levels; I had to use multiple copies of GCaMP6m in the P-EN1 recordings, specifically, to visualize their signals (see Methods). The added GCaMP load in P-EN1s could then slow down the movement of the heading phase, leading to a longer delay between behavior and phase updating. It is expected that in the VT032906>GCaMP6m flies, the E-PG and P-EN2 phases are similarly delayed with respect to behavior. Note that in Figure 3.13c, where I show that the P-EN1 bridge asymmetry arises early and the P-EN2 asymmetry arises late, during turns, I align these asymmetries to the movement of the GCaMP phase, a neuronal signal, not the fly's behavior, minimizing concerns related to the behavioral latency just mentioned. Moreover, I also found that the P-EN1 asymmetry is early and the P-EN2 asymmetry is late

when imaging in the ellipsoid body, where P-ENs expressed a different calcium indicator, jRGECO1a.

Comments on P-ENs and E-PGs not overlapping in the innermost and outermost glomeruli of the protocerebral bridge

P-ENs innervate the outer eight glomeruli on either side of the protocerebral bridge, whereas E-PGs innervate the inner eight glomeruli on either side. If P-ENs and E-PGs are to form an integration circuit, how would an activity peak carried by E-PGs and P-ENs cross the “gap”, where P-ENs and E-PGs do not overlap in the bridge, to rotate around this circuit indefinitely (as I observe it to do)?

First, I note that, while the two cell types do not overlap completely in the bridge, they do overlap in the ellipsoid body. If P-ENs output (directly or indirectly) to E-PGs in the ellipsoid body (Wolff, Iyer, and Rubin 2015; Lin et al. 2013) (Figure 3.6e-f), every P-EN neuron innervating a tile in the ellipsoid body has two matching E-PG neurons innervating the two wedges within that tile. However, there is a gap when information flows back to the bridge: how do P-ENs receive inputs in the outermost glomeruli in the bridge (1L and 9R, using our numbering scheme) from the current heading estimate, if not from E-PGs (which do not project to 1L or 9R)?

A possibility I favor is that a cell type identified by Wolff et al. 2015 as distinct from, but very similar to, E-PGs connects wedges 1L and 1R in the

ellipsoid body to glomeruli 1L and 9R in the bridge (ie. the outermost glomeruli not innervated by E-PGs). This cell is depicted in Figure 3J of Wolff et al. 2015 and is perfectly suited for 'closing the gap' between E-PGs and P-EN1s in the outermost glomeruli of the bridge. This cell type is not labeled in the Gal4 driver line I used for imaging E-PGs.

Second, the interaction between E-PGs and P-EN2s in the bridge is likely indirect because the P-EN2 peaks are anti phase relative to the E-PG peaks. Indeed, there exists a set of local neurons in the protocerebral bridge (PB18.s-GxΔ7Gy.b, or "Δ7" neurons in Figure 18B in Wolff et al. 2015), whose anatomy suggests that they might link the activation of E-PGs to that of P-EN2s. If one closely examines the anatomy of the Δ7 neurons, it becomes clear that if Δ7 neurons were to receive direct inputs from E-PGs, Δ7 neurons would be perfectly poised to have maximal transmitter release at the anti-phase locations in the bridge, which is where P-EN2's are maximally active. Because Δ7's tile the entire bridge, if they were to receive inputs from E-PGs and output to P-EN2s, they too could help explain how E-PG output influences P-EN2 physiology in the outermost glomeruli.

That P-ENs and E-PGs do not overlap in the innermost glomeruli does not, in principle, present an obstacle for the circuit model proposed here, if P-ENs output to E-PGs in the ellipsoid body (where there is complete overlap) and if E-PGs output to P-ENs in the bridge, with the additional neurons mentioned above to complete the overlap in the outermost glomeruli. In this scenario, the circuit

can continue to rotate indefinitely, and the E-PGs innervating the innermost glomeruli may interact with other neurons in this circuit (such as the Δ7 neurons mentioned above, *$PB_{G1\text{-}8}$.s-EBt.b-D/Vgall.b* neurons, and other neurons innervating the innermost glomeruli (Wolff, Iyer, and Rubin 2015)).

Similarities between angular integration in *Drosophila* and rodents

The physiology of E-PGs closely resembles that of rodent head-direction cells in the presubiculum and other areas (Taube, Muller, and Ranck 1990a; Taube 2007), whereas the physiology of left and right P-ENs resembles that of head-direction and angular head velocity-sensitive cells in the left and right lateral mammillary nucleus (Stackman and Taube 1998; Blair, Cho, and Sharp 1998). Whereas the fine scale anatomy for the rodent head-direction system is unknown, the models proposed to account for its physiological properties (Skaggs et al. 1995; K. Zhang 1996; Redish, Elga, and Touretzky 1996; Sharp, Blair, and Brown 1996; McNaughton et al. 2006) bear a strong resemblance to the anatomically-inspired model proposed here (compare Figure 3 in Skaggs et al.1995 with Figure 3.16j-l), suggesting that insects and mammals may use common mechanisms to update their sense of heading. Although apparently hard-wired to integrate turning velocities, the essential features of this circuit are general enough to integrate other variables (including two- or more-dimensional variables (McNaughton et al. 2006)) over time, and may therefore appear in other integrating neural systems such as the mammalian grid cell system (Hafting et al.

2005; McNaughton et al. 2006; Sargolini et al. 2006), among others (Robinson 1989; Major and Tank 2004; Pastor, la Cruz, and Baker 1994; Aksay et al. 2001).

Table 3.1 | Characterization and classification of individual neurons identified by multi color flip out in three P-EN Gal4 lines.

These tables show a summary of the entire multi color flip out data sets used in generating Figure 3.6g-l. Each row represents an individual neuron. Information about the glomerulus, tile, and nodulus to which each neuron projects is shown in the PB (protocerebral bridge), EB (ellipsoid body) and Noduli columns, respectively, as well as a fourth column (Other Neuropil) for other structures. The revised numbering scheme is shown (see Figure 3.6a-d). PB glomerulus numbers are preceded by 'L' for left or 'R' for right. NI: Not identifiable because the signal was too weak or the density of labeled neurites was too high. Asterisks mark tiles that were assigned to a neuron based on color and not by tracing the axon, either because the axonal signal was too weak or because the density of labeled neurites was too high. FLPL and FLPG5 refer to the flippase transgenes used for high and low density neuron labeling, respectively (Nern, Pfeiffer, and Rubin 2015). Note that the vast majority of neurons identified by multicolor flip out, in all Gal4 lines, were consistent with the known anatomy of P-ENs. 2/41 neurons imaged in R12D09 were consistent with being PB local neurons instead of P-ENs.

Gal4 Line	Cell #	Brain	PB glomerulus #	EB tile #	Nodulus	Other Neuropil	consistent with PEN	unambiguously PEN
VT032906	1	1 (FLPL)	L1	2	NI		✓	
VT032906	2	1 (FLPL)	L2	3	right, NO1		✓	✓
VT032906	3	1 (FLPL)	L3	4	right, NO1		✓	✓
VT032906	4	1 (FLPL)	R7	6	left, NO1		✓	✓
VT032906	5	1 (FLPL)	R8	7	left, NO1		✓	✓
VT032906	6	2 (FLPL)	L1	2	right, NO1		✓	✓
VT032906	7	2 (FLPL)	L2	3	right, NO1		✓	✓
VT032906	8	2 (FLPL)	L3	4	right, NO1		✓	✓
VT032906	9	2 (FLPL)	L4	5	NI		✓	
VT032906	10	2 (FLPL)	L5	6	right, NO1		✓	✓
VT032906	11	2 (FLPL)	L6	7	right, NO1		✓	✓
VT032906	12	2 (FLPL)	L7	8	right, NO1		✓	✓
VT032906	13	2 (FLPL)	R3	NI	NI		✓	
VT032906	14	2 (FLPL)	R4	3	left, NO1		✓	✓
VT032906	15	2 (FLPL)	R5	4	left, NO1		✓	✓
VT032906	16	2 (FLPL)	R6	5	left, NO1		✓	✓
VT032906	17	2 (FLPL)	R7	6	left, NO1		✓	✓
VT032906	18	2 (FLPL)	R8	7	left, NO1		✓	✓
VT032906	19	3 (FLPL)	L1	2	right, NO1		✓	✓
VT032906	20	3 (FLPL)	L1		right NO2V	FB		
VT032906	21	3 (FLPL)	L3	4	right, NO1		✓	✓
VT032906	22	3 (FLPL)	L4	5	right, NO1		✓	✓
VT032906	23	3 (FLPL)	L5	6	right, NO1		✓	✓
VT032906	24	3 (FLPL)	L6	7	right, NO1		✓	✓
VT032906	25	3 (FLPL)	R3	NI	NI			
VT032906	26	3 (FLPL)	R4	3	left, NO1		✓	✓
VT032906	27	3 (FLPL)	R6	5	left, NO1		✓	✓
VT032906	28	3 (FLPL)	R6	5	left, NO1		✓	✓
VT032906	29	3 (FLPL)	R8		left, NO2V	FB		
VT032906	30	4 (FLPL)	L2	3	right, NO1		✓	✓
VT032906	31	4 (FLPL)	L3	4	right, NO1		✓	✓
VT032906	32	4 (FLPL)	L4	5	right, NO1		✓	✓
VT032906	33	4 (FLPL)	L5	6	right, NO1		✓	✓
VT032906	34	4 (FLPL)	L7	8	right, NO1		✓	✓
VT032906	35	4 (FLPL)	R4	3	left, NO1		✓	✓
VT032906	36	4 (FLPL)	R6	5	left, NO1		✓	✓
VT032906	37	4 (FLPL)	R8	7	left, NO1		✓	✓
VT032907	38	4 (FLPL)	R9	8	left, NO1		✓	✓

VT032906	39	5 (FLPG5)	L6	7	right, NO1		✓	✓
VT032906	40	5 (FLPG5)	R9	8	left, NO1		✓	✓
VT032906	41	6 (FLPG5)	L7	8	right, NO1		✓	✓
VT032906	42	7 (FLPG5)	L3	4	right, NO1		✓	✓
VT032906	43	7 (FLPG5)		5		FB		
VT032906	44	8 (FLPG5)	R4	3	left, NO1		✓	✓
VT032906	45	8 (FLPG5)	R8	7	NI		✓	
total	**45**						**41/45**	**37/45**

Gal4 Line	Cell #	Brain	PB glomerulus #	EB tile #	Nodulus	Other Neuropil	consistent with PEN	unambiguously PEN
VT020739	1	1 (FLPL)	L3	NI	NI		✓	
VT020739	2	1 (FLPL)	L4	5	right, NO1		✓	✓
VT020739	3	1 (FLPL)	L4	5	right, NO1		✓	✓
VT020739	4	1 (FLPL)	R5	4	left, NO1		✓	✓
VT020739	5	1 (FLPL)	R6	5	left, NO1		✓	✓
VT020739	6	2 (FLPL)	L6	7	right, NO1		✓	✓
VT020739	7	2 (FLPL)	L6	7	right, NO1		✓	✓
VT020739	8	2 (FLPL)	L7	NI	NI		✓	
VT020739	9	2 (FLPL)	R5	4	left, NO1		✓	✓
VT020739	10	2 (FLPL)	R9	8	NI		✓	
VT020739	11	2 (FLPL)	R9	8	NI		✓	
VT020739	12	3 (FLPL)	L4	5	right, NO1		✓	✓
VT020739	13	3 (FLPL)	L4	5	right, NO1		✓	✓
VT020739	14	3 (FLPL)	R4	3	left, NO1		✓	✓
VT020739	15	3 (FLPL)	R5	4	left, NO1		✓	✓
VT020739	16	3 (FLPL)	R6	5	left, NO1		✓	✓
VT020739	17	3 (FLPL)	R6	5	left, NO1		✓	✓
VT020739	18	3 (FLPL)	R8	7*	NI		✓	
VT020739	19	4 (FLPL)	L1	2	right, NO1		✓	✓
VT020739	20	4 (FLPL)	L1	2	right, NO1		✓	✓
VT020739	21	4 (FLPL)	L1	2	right, NO1		✓	✓
VT020739	22	4 (FLPL)	L5	6*	NI		✓	
VT020739	23	4 (FLPL)	L7	8	right, NO1		✓	✓
VT020739	24	4 (FLPL)	L7	8	right, NO1		✓	✓
VT020739	25	4 (FLPL)	R2	1*	left, NO1		✓	
VT020739	26	4 (FLPL)	R5	4	left, NO1		✓	✓
VT020739	27	4 (FLPL)	R6	5	left, NO1		✓	✓
VT020739	28	4 (FLPL)	R8	7*	NI		✓	
VT020739	29	4 (FLPL)	R8	7*	NI		✓	

VT020739	30	4 (FLPL)	R9	8	NI		✓	
VT020739	31	5 (FLPL)	L2	3	right, NO1		✓	✓
VT020739	32	5 (FLPL)	L3	4	right, NO1		✓	✓
VT020739	33	5 (FLPL)	L6	7*	right, NO1		✓	
VT020739	34	5 (FLPL)	R2	1	left, NO1		✓	✓
VT020739	35	5 (FLPL)	R4	3	left, NO1		✓	✓
VT020739	36	5 (FLPL)	R6	5	left, NO1		✓	✓
VT020739	37	5 (FLPL)	R6	5	left, NO1		✓	✓
VT020739	38	5 (FLPL)	R8	7	left, NO1		✓	✓
VT020739	39	6 (FLPG5)	R2	1	left, NO1		✓	✓
VT020739	40	6 (FLPG5)	R4	3	left, NO1		✓	✓
VT020739	41	7 (FLPG5)	L2	3	right, NO1		✓	✓
VT020739	42	7 (FLPG5)	L4	5	right, NO1		✓	✓
VT020739	43	7 (FLPG5)	R9	8	left, NO1		✓	✓
total	**43**						**43/43**	**32/43**

Gal4 Line	Cell #	Brain	PB glomerulus #	EB tile #	Nodulus	Other Neuropil	consistent with PEN	unambiguously PEN
R12D09	1	1 (FLPL)	L1	2	right, NO1		✓	✓
R12D09	2	1 (FLPL)	L3	4	right, NO1		✓	✓
R12D09	3	1 (FLPL)	L4	5	right, NO1		✓	✓
R12D09	4	1 (FLPL)	L4	5	right, NO1		✓	✓
R12D09	5	1 (FLPL)	L6, R5					
R12D09	6	1 (FLPL)	R3	2	left, NO1		✓	✓
R12D09	7	1 (FLPL)	R4	3	left, NO1		✓	✓
R12D09	8	1 (FLPL)	R5	4	left, NO1		✓	✓
R12D09	9	1 (FLPL)	R9	8	left, NO1		✓	✓
R12D09	10	2 (FLPL)	L5	6	right, NO1		✓	✓
R12D09	11	2 (FLPL)	L6	7	right, NO1		✓	✓
R12D09	12	2 (FLPL)	L8	1	right, NO1		✓	✓
R12D09	13	2 (FLPL)	R3	2	left, NO1		✓	✓
R12D09	14	2 (FLPL)	R4	3	left, NO1		✓	✓
R12D09	15	2 (FLPL)	R6	5	left, NO1		✓	✓
R12D09	16	2 (FLPL)	R6	5	left, NO1		✓	✓
R12D09	17	3 (FLPL)	L1	2	NI		✓	
R12D09	18	3 (FLPL)	L2	3	right, NO1		✓	✓
R12D09	19	3 (FLPL)	L4	5	right, NO1		✓	✓
R12D09	20	3 (FLPL)	L4	5	right, NO1		✓	✓
R12D09	21	3 (FLPL)	L6	7	right, NO1		✓	✓
R12D09	22	3 (FLPL)	L6	7	right, NO1		✓	✓

R12D09	23	3 (FLPL)	R2	1	left, NO1	✓	✓
R12D09	24	3 (FLPL)	R3	2	left, NO1	✓	✓
R12D09	25	3 (FLPL)	R5	4	left, NO1	✓	✓
R12D09	26	3 (FLPL)	R8	7	left, NO1	✓	✓
R12D09	27	3 (FLPL)	R9	8	left, NO1	✓	✓
R12D09	28	4 (FLPL)	L1	2	right, NO1	✓	✓
R12D09	29	4 (FLPL)	L3, R2				
R12D09	30	4 (FLPL)	L4	3	NI	✓	
R12D09	31	4 (FLPL)	L7	8	right, NO1	✓	✓
R12D09	32	4 (FLPL)	R6	5	left, NO1	✓	✓
R12D09	33	4 (FLPL)	R8	7	left, NO1	✓	✓
R12D09	34	4 (FLPL)	R8	7	left, NO1	✓	✓
R12D09	35	5 (FLPG5)	R8	7	left, NO1	✓	✓
R12D09	36	5 (FLPG5)	R8	7	left, NO1	✓	✓
R12D09	37	5 (FLPG5)	L1, L9				
R12D09	38	6 (FLPG5)	R3	2	left, NO1	✓	✓
R12D09	39	6 (FLPG5)	R6	5	left, NO1	✓	✓
R12D09	40	7 (FLPG5)	R4	3	left, NO1	✓	✓
R12D09	41	7 (FLPG5)	R9	8	left, NO1	✓	✓
total	**41**					**38/41**	**36/41**

Chapter 4 | Flexibly learning angular landmark positions.

When the fly navigates in the dark, the E-PG heading signal, or *phase*, tracks the fly's heading with an accumulating drift over time (Figure 3.3). When the fly navigates with a closed-loop bar that simulates a distant, static landmark, however, the E-PG phase tracks the fly's heading much more faithfully over time (Figure 4.1, reproduced for convenience from Figure 3.1g and Figure 3.2j). With a closed-loop bar, the E-PG phase does not perfectly match the position of the bar at all moments in time—there still appears to be small errors in the mapping between the bar position and E-PG phase—however, the E-PG phase does not *accumulate* errors over time. This observation strongly suggests that the bar imparts positional information to the E-PG neurons (i.e. which angle the E-PG bolus should reside at), thus correcting for errors in the angular integration process. In other words, a mapping exists between each bar position on the arena and each phase value of the E-PG heading signal, preventing drift between the two. This chapter deals with the possible mechanisms for how this mapping is determined.

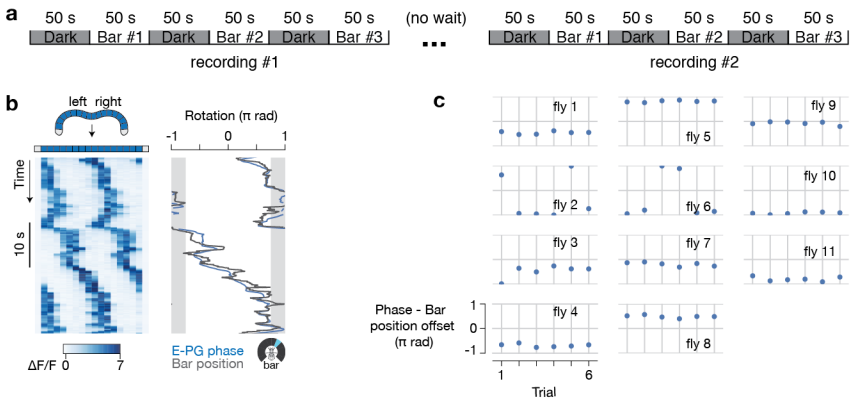

Figure 4.1 | E-PG properties during closed-loop bar

a, Trial structure. **b**, (Left) E-PG bridge activity during closed-loop bar. (Right) E-PG phase and bar position. The gap in the arena behind the fly where the bar is not visible is highlighted in grey. **c**, Offsets between the E-PG phase and bar position for each trial in each fly. Offsets are only computed when the bar is visible. Data reproduced for convenience from Figure 3.1g and Figure 3.2j.

Two models for mapping landmark positions

The space of possible mechanisms for mapping the angular position of a landmark in the world relative the fly's head (i.e. the angular position of the blue bar on our panoramic display) to the position of the E-PG phase in the central complex can be divided into two broad classes: one where the mapping is permanent and hardwired during development, and a second where the mapping is flexible, and learned or modified during the lifetime of the fly. These two classes – permanent and flexible – can also be considered from the point of view of circuitry (Figure 4.2). In the first model, where the bar-phase mapping is permanently set, a "bar" neuron, tuned to respond to a bar at specific retinal positions, synapses onto one tile in the ellipsoid body (or glomerulus in the bridge) (Figure 4.2a, upper panel). The next "bar" neuron connects bar positions 45º over on the retina to the next tile 45º over in the ellipsoid body (Figure 4.2a, lower panel). This mapping would have to be shifted by a constant angle during development to produce the different bar-phase offsets observed in different flies (Figure 4.1c).

In the second model, where the bar-phase mapping is flexible, each neuron weakly connects one range of bar positions to all wedges (and E-PGs) in the ellipsoid body. However, the strength of each connection is then modulated over time, with the connections in some wedges becoming stronger, and others weaker, allowing the "bar" neuron to drive activity in only some wedges (E-PGs) and thus impart positional information onto the system. A simple model might

work as follows. Even when the bar is not present, there is always an E-PG activity peak in the bridge (Figure 3.5g) and ellipsoid body (Figure 3.9i,j, Seelig and Jayaraman 2015, and shown schematically in Figure 4.2c). If the strength of a synapse between a “bar” neuron and an E-PG neuron increases as a function of coincident activity in these two cells, then when the bar first appears (Figure 4.2d), the “bar” cell that responds to this bar position will become associated specifically with the E-PG neurons that are already active (Figure 4.2e). When the fly turns left, the E-PG activity peak rotates clockwise in the ellipsoid body, while the bar rotates clockwise on the retina; a new “bar” neuron that responds to this bar position now becomes associated with the new set of active E-PG neurons (Figure 4.2f). Over time, each “bar” neuron becomes associated with specific E-PG neurons, generating the bar-phase mapping across all bar and heading positions. This model is analogous to (and inspired by) the model presented by Skaggs et al. 1995.

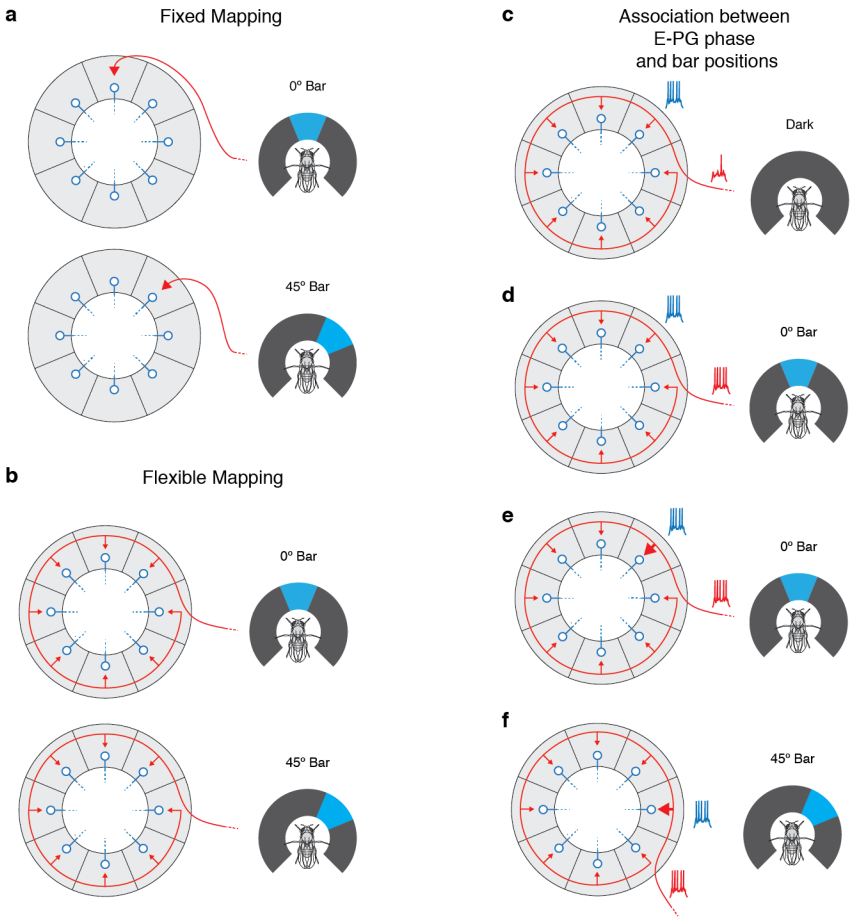

Figure 4.2 I Circuit architectures for mapping landmarks to a heading signal

a, Model for permanent mapping between landmark positions and E-PG neurons. Each neuron tuned to a specific bar position maps to one tile in the ellipsoid body. **b,** Model for a flexible mapping between landmark positions and E-PG neurons. Each neuron tuned to a specific bar position maps to all tiles in the ellipsoid body. **c-f**, Model for how a flexible mapping is set dynamically over time. **c**, An E-PG activity peak in the dark. **d**, A bar appears, driving activity in a “bar” neuron responsive to this bar position. **e**, Coincident activity in the active “bar” neuron and the active E-PG neurons strengthens synapses between the two. **f**, As the fly turns left, the bar rotates clockwise on the retina, and the E-PG peak rotates clockwise in the ellipsoid body, strengthening the pair of newly active “bar” and E-PG neurons in the clockwise direction.

Stability of the mapping between a landmark and the E-PG phase

To simulate a distant, static landmark, I presented a single bright blue bar that rotated in closed-loop with the fly (see Methods). Whereas the real world contains many nearby objects and distant landmarks, I used this reduced visual stimulus to simplify the sensory inputs to the fly as much as possible. The effect of multiple visual features on E-PG activity is also briefly discussed below.

To distinguish between the permanent and flexible models, I analyzed whether the mapping between bar positions and the E-PG phase can change within the same fly. Since the mapping between the E-PG phase and bar position is approximately linear, I used the mean offset between the E-PG phase and the bar position as a metric to quantify this mapping (the mean offset is defined as the circular mean of the difference between the E-PG phase and the bar position for a given trial or time period). In a permanent bar-phase mapping model, this offset can never change over time within a single fly, whereas in a flexible model it can change. I only computed the offset between the E-PG phase and bar position for sample points in which the bar was visible on the LED display (i.e. not during times when the bar resided in the 90º gap in the arena, directly behind the fly). In the initial experiments described in Chapter 3, each fly was presented with six 50 s "trials" in which the arena was completely dark, interleaved with six 50 s trials in which a closed-loop bar was present (Figure 4.1a). In these conditions, the offset between the E-PG phase and bar position was typically relatively constant from trial to trial within a fly (Figure 4.1c), even though each fly

experienced 50 s of darkness in between each closed-loop bar trial (which is enough time for the E-PG phase to drift away from the bar position). This result shows that the bar-phase mapping can be stored for at least 50 s without the bar. However, the offset was also clearly different from fly to fly (Figure 4.1c). If the mapping is permanently set during development, then the circuit would have to be wired differently in each fly.

To test whether the bar-phase mapping is truly permanent, or if it can be reset within the same fly, I imaged each fly twice, waiting for 32 minutes in between each recording as the fly walked in constant darkness. Each fly was presented with the following six trials prior to the 32 minute break: 30 s dark, 60 s closed-loop bar, 30 s dark, 30 s closed-loop bar, 30 s dark, and 30 s closed loop bar. After waiting 32 minutes, I repeated the same six trials (Figure 4.3a). For most flies, the offset was constant for the first three bar trials, which were separated by 30 s of darkness (Figure 4.3b,d). However, for several flies, the offset was also consistently different in the last three trials after 32 minutes in darkness, compared to the first three trials (Figure 4.3c,d, obvious flies in which this was the case are highlighted with a red box), showing that a relatively stable offset can be reset after 32 minutes in the dark. These results indicate that the bar-phase mapping is not permanently set during development, but rather learned as the fly experiences visual features in its environment. Indeed, the first time that the fly is placed in the experimental setup and exposed to the closed-loop bar likely represents such a “learning” event.

One can also consider whether the stability of the offset increases as the fly is exposed to the bar for longer times. From this perspective, it is interesting to note that the flies in Figure 4.1 (from Chapter 3) were exposed to the bar for longer times overall than the flies in Figure 4.3, which might explain why the offsets in Figure 4.1c appear more stable from trial to trial than in Figure 4.3d. Moreover, I was careful to not present the fly with a bar during the setup period for the experiments analyzed for Figure 4.3 (i.e. when aligning the fly and finding the central complex for imaging), whereas in the experiments analyzed in Figure 4.1 the flies sometimes saw a bar in closed-loop before the first trial. The experiments in Figure 4.1 and 4.3 also differed in the length of dark trials (50 s vs. 30 s), further complicating any comparison across data sets. Systematic experiments, where only one variable is changed at a time, should be used in the future to rigorously test whether the offset is more stable if the fly is exposed to the bar for longer periods of time.

Associating landmark positions for the first time

The flexible model described in Figure 4.2b-f predicts that the E-PG phase should respond differently to the bar during the first instance it appears on the screen, before any bar-phase mapping has been learned by the system, compared to subsequent exposures to the bar in closed loop, after a bar-phase mapping has been learned. I therefore compared the first dark-to-bar transition to the second and third transitions in each experiment. In the first transition, the E-

PG phase sometimes continued integrating the fly's heading from the position it happened to be in when the bar first appeared (e.g. Figure 4.3e), consistent with the hypothesis that the mapping, in these cases, was initialized by the conjoined activity of E-PGs and the visual inputs to the system at the moment the bar first appeared on the screen. During subsequent bar appearances (after 30 s dark periods), however, the E-PG phase often jumped to a specific location in the bridge, whose offset to the bar's position on the visual display often matched the bar-phase offset from the previous bar trial (Figure 4.3f), suggesting that the mapping was learned in the first trial(s) and was being recalled in subsequent trials. To quantify this effect, I computed the absolute distance between the bar-phase offset at each time point and the average bar-phase offset in a 5 s window, starting 5 s after the start of a bar trial (Figure 4.3g), when the bar-phase mapping is likely to be set. This metric quantifies, at each time point before and after the bar appears, how many degrees the E-PG phase offset is from the offset measured 5 s after the bar appears. I refer to this angular value as the mapping error, or simply *error*, for short. In the first dark-to-bar transition, the error seems to gradually approach near zero at 5-10 s (Figure 4.3g, upper panel), consistent with the bar-phase mapping being gradually formed over time via the circuit's intrinsic integrative process. Note that the error values in the 5-10 s window in Fig. 4.3g are typically a little above zero, instead of at zero, because if the bar-phase offset fluctuates above and below its mean, the *absolute* distance between the offset and its mean (i.e. the error as defined above) will be,

on average, non-zero (whereas the *signed* distance from the mean is, on average, zero by definition). During subsequent dark-to-bar transitions, however, this error quickly drops to near zero at the start of the bar trial (Figure 4.3g), consistent with the system "recalling" the bar-phase mapping and correcting its phase immediately. Put another way, the bar immediately imparts positional information to the E-PG neurons during the 2nd and 3rd trials, but has a less immediate effect during the 1st trial.

In the extreme case where the bar-phase mapping is immediately set the instant the bar first appears, then one would have expected the blue curve in Fig. 4.3g to reach near zero at the *start* of the bar trial after gradually decreasing to this level in the seconds in the dark immediately before. That is, if all flies behaved like the example fly in Figure 4.3e, where the phase faithfully followed the bar starting from where the phase was already located immediately prior to the bar's appearance, then the mean error (the thick blue line) would have been near zero at the start of the first bar trial in Figure 4.3e (top panel). The fact that we did not observe this effect , but rather observed higher initial error values that approached to near zero at later time points, suggests that perhaps the mapping takes several seconds, and that the fly's heading system is still effectively relying on its error-prone angular integration process for these several seconds before the mapping is fully set. Another caveat is that I did not have full control over whether the bar was visible in these experiments: even during a closed-loop bar trial, the bar was invisible to the fly when it passed through the 90^{o} gap in the

back of the arena. To alleviate this concern, only trials where the bar was visible for at least 80% of the time during the first 5 seconds of the bar trial are shown in Figure 4.3g. In addition, I also excluded showing sample points during which the bar was invisible to the fly.

Put quantitatively, the initialization model would predict that the y-axis error signal for the blue curve in Fig. 4.3g would be closer to zero than chance prior to the bar's appearance. The average error for a uniform distribution of offsets is 90º (shown with a dotted line in Figure 4.3g), which is roughly the mean error value observed during dark trials (i.e. -10 s to -5 s in Figure 4.3g). A lower-than-chance error is not immediately apparent in the blue mean curve in Figure 4.3g, where the error at time zero in the first dark-to-bar transition is roughly similar to that in the subsequent dark-to-bar transitions. There is, however, a trend for the error in the first transition to dip below 90º chance levels a few seconds before the start of the bar trial, whereas for subsequent transitions the error tends to remain close to chance levels until the start of the bar trial. These results might point to an initialization process, but more data would be required to properly test this prediction.

Figure 4.3 | Stability of the mapping between E-PG phase and bar position

a, Trial structure (note differences from Figure 4.1a). **b**, Entire first recording of E-PG neurons. For display, the E-PG phase is shifted by a constant offset to best match the bar position in trial 1. This offset is shown below the panel. The gap in the arena behind the fly where the bar is not visible is highlighted in grey. **c**, Same as **b**, for the second recording. Note the different offset compared to **b**. **d**, Bar-phase offsets for each trial in each fly. The circular mean and circular s.d. for each trial are shown. Note trials 4-6 were performed 32 min after trials 1-3. The fly was in the dark during these 32 min. Red boxes highlighted flies where the offset is consistently different in the first three trials compared to the last three trials. **e**, First dark-to-bar transition in **c** (fly #1, recording #2). The gap in the arena where the bar is not visible is highlighted in grey. During the dark trial, the entire arena is highlighted in grey. The “virtual” bar position (or ball position) is shown for the dark trial. **f**, Third dark-to-bar transition in **c**. Note the jump in the E-PG phase when the bar first appears. **g**, Absolute difference in the offset at each time point and the mean offset 5-10 seconds after the start of the bar trial, for the first dark-to-bar transition (top panel) and the second and third dark-to-bar transitions (bottom panel) (referred to as the *error*, see text for details). Thin lines represent single trials, thick lines represent the mean across trials. Only trials where the bar was visible for at least 80% of the time during the first 5 s of the bar trial are shown. In addition, errors are not shown for when the bar is not visible. Note the sharp drop in the error at the start of the bar trial in the second and third transitions compared to the first transition.

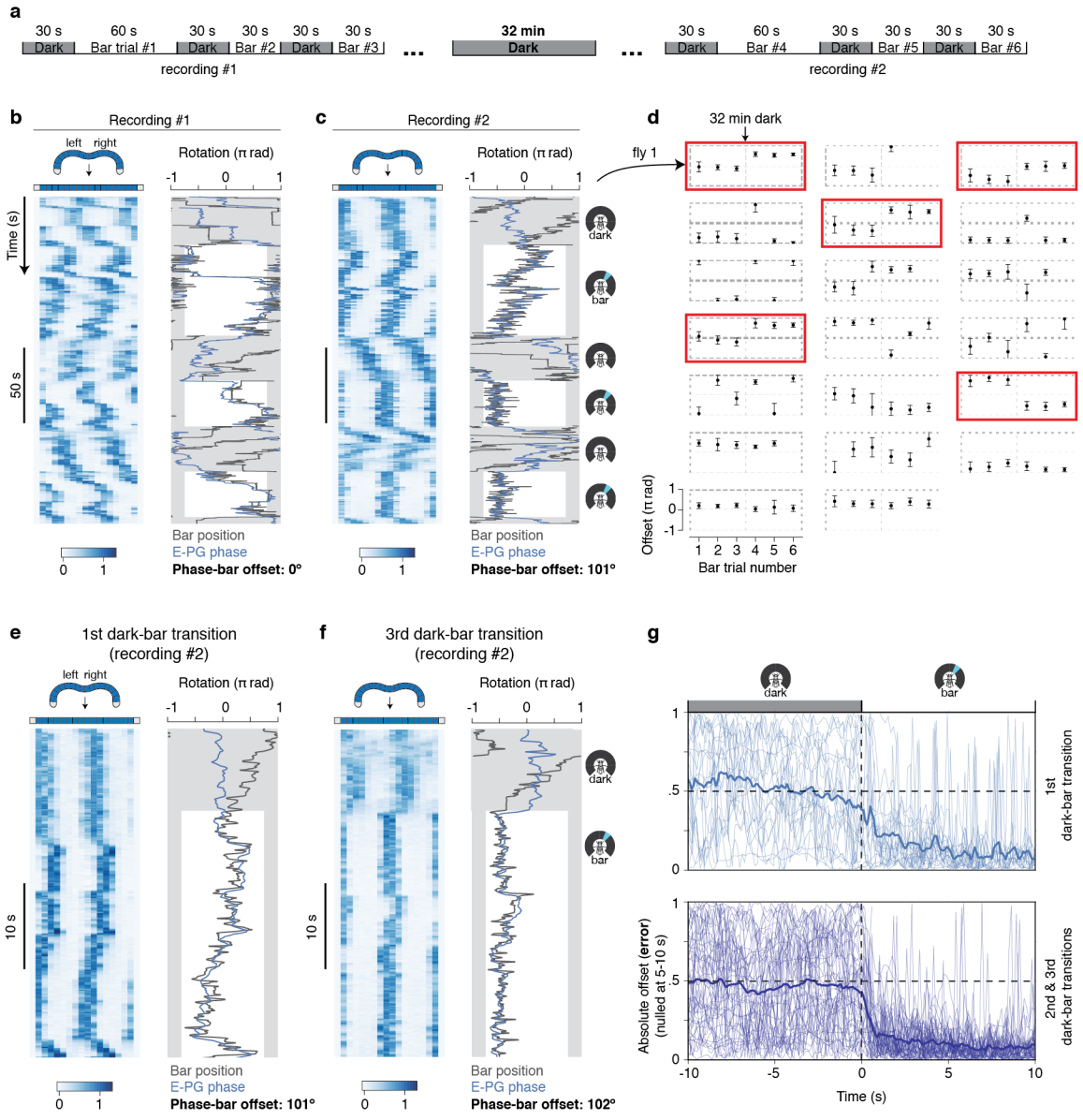
a
30 s
Dark
60 s
Bar trial #1
30 s
Dark
30 s
Bar #2
30 s
Dark
30 s
Bar #3
recording #1
32 min
Dark
30 s
Dark
60 s
Bar #4
30 s
Dark
30 s
Bar #5
30 s
Dark
30 s
Bar #6
recording #2
b
Recording #1
left right
Rotation (π rad)
Time (s)
50 s
Bar position
E-PG phase
Phase-bar offset: 0°
c
Recording #2
Rotation (π rad)
dark
bar
Bar position
E-PG phase
Phase-bar offset: 101°
d
32 min dark
fly 1
Offset (π rad)
Bar trial number
e
1st dark-bar transition
(recording #2)
left right
Rotation (π rad)
10 s
Bar position
E-PG phase
Phase-bar offset: 101°
f
3rd dark-bar transition
(recording #2)
Rotation (π rad)
dark
bar
10 s
Bar position
E-PG phase
Phase-bar offset: 102°
g
dark
bar
1st
dark-bar transition
Absolute offset (error)
(nulled at 5-10 s)
2nd & 3rd
dark-bar transitions
Time (s)

Discussion

I propose the following model for how landmark positions are associated with different E-PG neurons, or, equivalently, internal heading estimates. An activity peak always exists in E-PG neurons, whether visual stimuli are present or not (Figure 3.3). At the time a visual feature first appears, it drives activity in a "feature detector" neuron, which synapses weakly onto all E-PG neurons. The coincident activity in this feature detector neuron and the subset of E-PG neurons that are currently active specifically strengthens synaptic connections between these two cell populations. When the fly turns left, the visual feature rotates clockwise on the retina, and the E-PG activity peak rotates clockwise in the ellipsoid body. The synaptic connections between these two new sets of active feature detector and E-PG neurons also become strengthened. As the fly explores its environment, each visual feature position becomes associated with a subset of E-PG neurons, completing the mapping between different retinal positions of this visual feature and the fly's sense of heading. Every time the visual feature appears at a specific position on the fly's retina, specific E-PG neurons become activated, yoking the fly's internal sense of heading to this visual feature.

This model, if true, explains why the offset is different from fly to fly because the initialization conditions (i.e. the initial E-PG phase and the initial bar position) are not controlled. The model also explains how multiple visual features (of which there are presumably many in the fly's natural environment) become

associated with a single, coherent heading signal (data not shown, Seelig and Jayaraman 2015) because each visual feature is independently mapped to the same E-PG phase. The preliminary data shown here provide initial support for two more fundamental predictions of the flexible-mapping model: (1) that the landmark mapping is not permanent, and (2) that the mapping may be initialized the first time the fly is exposed to the landmark.

One reason for the weak effects in the E-PG phase "predicting" the eventual bar-phase offset (i.e., why the blue curve in Fig. 4.3g is not near zero prior to the bar's appearance) may be that the visual feature neuron system is not perfectly naïve when the bar is first displayed, in that some synapses between visual feature detectors and E-PGs may have already been strengthened relative to others prior to the experiment (due to each fly's idiosyncratic visual experience prior to the experiment). This caveat may be addressed by "resetting" synaptic strengths by waiting for longer times in the dark before starting the experiment. Another caveat is that I did not have full control over whether the bar was visible in the experiments to date (the fly controlled the position of the bar which could, in some trials, reside in the back of the arena). This concern was addressed to some degree by selecting for trials where the bar was present for greater than 80% of the time in the first 5 s after the bar trial started (see above). In future experiments, it would be convenient to experimentally ensure that the bar is always visible to the fly, either by having it jump between the two edges of the arena at -135º and +135º as the fly rotates the ball, or by having it be ~90˚ in

width, or bigger, so that at least one edge is always visible. These experiments are currently in progress.

A third prediction of the flexible-mapping model, not tested here, is that E-PGs should become most strongly associated with features that consistently move in lock step with the fly's heading. These would be fixed features of a room or an outdoor environment, like a distant mountain, rather than other nearby insects that are moving around. One way to test this prediction in our controlled setup is to add random noise to the position of the bar, simulating an independently moving agent/animal in the real world, and vary the relative contributions of the fly's heading vs. the external noise contribution to the position of the bar. One would expect that the bar-phase association becomes poorer as the weight of the noise component is increased. Such a result would argue that the fly's heading signal emphasizes static landmarks over objects that move independently of the fly. This would make sense since static objects are a more reliable source of information for one's orientation in the world in comparison to moving objects, like other animals. A fourth prediction of this model is that visual neurons sensitive to the same visual feature (i.e., vertical bars) but with receptive fields in different positions of the arena are independently associated with the E-PGs. Similarly, neurons tuned to different bar orientations, but with receptive fields in overlapping regions of the arena are also independently associated to the E-PG phase location (to the degree that the fly's visual system can discriminate between such features). To test this prediction, one might make the

bar visible in only one 90˚ quadrant of the arena (while keeping track of the bar as it rotates outside of this 90º quadrant) during the first trial and then, in the second trial, present the bar in a non-overlapping 90˚ quadrant to test if the bar-phase mapping is independently learned in the two quadrants (i.e. if the bar-phase offset in the second quadrant is determined by the bar-phase offset in the first quadrant). One can then present the bar in both quadrants at the same time in a third trial, to determine if and how these two learned bar-phase associations are merged together (i.e. if the mappings, or offsets, are initially different in each quadrant, how do they eventually become the same, as is expected for a continuous linear mapping between bar positions and E-PG phases). Similarly, one can show a vertical bar in the first trial, and a 45º bar (or another visual feature) in the second trial, performing the same analyses as with the quadrant experiments.

Of the known neurons that innervate the *Drosophila* central complex, the ellipsoid *ring neurons* represent the best candidates for the "feature detector" neurons described above. First, each ring neuron outputs to the entire ellipsoid body, as in Figure 4.2. Second, ring neurons are visually responsive and have relatively small receptive fields, and collectively respond to different feature orientations and positions on the retina (Seelig and Jayaraman 2013). Third, ring neurons have been implicated in place (Ofstad, Zuker, and Reiser 2011) and orientation (Neuser et al. 2008) learning in *Drosophila*, consistent with a role in associating landmark positions with the fly's heading signal. Fourth, ring neurons

strongly express both NMDA receptor subtypes (Wu et al. 2007), a synaptic receptor that is thought to serve a central role in implementing the detection of coincident activity in pre- and postsynaptic cells. NMDA receptors in ring neurons specifically are also required for an olfactory learning task that requires navigating to one of two odor sources (Wu et al. 2007).

One wrinkle with regard to NMDA-receptor expression is that one would expect these receptors, in the simplest implementation of the proposed model, to be expressed in E-PGs because the typical location of NMDA receptors is in the postsynaptic cell (and in the above model, ring neurons would synapse onto E-PGs). NMDA receptors open only if both glutamate is present at the synpase (i.e., if the presynaptic cell is active) *and* the membrane is depolarized (i.e, if the postsynaptic cell is simultaneously active); this feature is what allows for coincidence detection (Malenka et al. 1989). However, NMDA-receptor expression is not obviously detectable in E-PGs, the post-synaptic cells of interest here (Wu et al. 2007), suggesting that the model cannot work exactly as advertised (or coincidence detection occurs in E-PGs via a process that bypasses any need for NMDA receptors). If NMDA receptors do serve a role, one possibility is that each ring neuron additionally receives presynaptic inputs from E-PG neurons (or neurons with E-PG-like properties). In this configuration, the NMDA receptors are pre-synaptically localized in the ring neuron terminals, but are post-synaptic to an axo-axonic synapse made by an E-PG (or E-PG-like) neuron that carries a heading signal. Calcium influx through NMDA receptors in

ring neurons could then trigger an induction of potentiation in the ring neuron presynaptic terminal; the expression of the potentiation could then occur through a presynaptic change in the same terminal (e.g. in the probability of release or quantal size, etc.) or a post-synaptic change in E-PGs—like an insertion of new channels into the post-synaptic membrane triggered by the arrival of an anterograde signal from the ring neuron (Kuntz, Poeck, and Strauss 2017), or even a post-synaptic change in the ring neuron terminal (since in this case ring neurons are both pre- and post-synaptic to E-PGs).The possibility that pre-synaptic NMDA receptors mediate potentiation is not completely unreasonable, given that presynaptic NMDA receptors have been described in the mammalian brain, and are thought to underlie presynaptic plasticity (Corlew et al. 2008), although their role is not as well studied as for postsynaptically-localized NMDA receptors (Paoletti, Bellone, and Zhou 2013).

Pinning down the specific cells, synapses and molecules involved in landmark association will provide a handle to more directly test the association model described above. My current focus is on determining if and how ring neurons are involved in associating landmark positions.

Chapter 5 | Discussion

This thesis describes the discovery of a heading signal in the *Drosophila* central complex (Chapter 2), evidence for how this neuronal circuit integrates the fly's turns over time (Chapter 3), and evidence for how this heading signal uses visual landmarks to update its heading estimate (Chapter 4). The circuit models described in Chapter 3 and Chapter 4, however, were partial models in the sense that only a few cell types relevant to each feature (e.g. angular integration and landmark association) were discussed, while assuming other circuit properties were generated by other cell types. In this chapter, I discuss a more comprehensive model for how for the protocerebral bridge – ellipsoid body circuit builds a heading signal and updates that signal based on the fly's behavior and directional cues in the fly's environment. This work was done in collaboration with Christoph Kirst, who has implemented these qualitative models in quantitative neuronal network simulations (not shown here).

In the model described here, I focus on the protocerebral bridge and the ellipsoid body because (1) to date, the physiological evidence for a heading signal comes from imaging these two structures (although our lab has convincing, unpublished evidence for heading signals in the fan-shaped body), and (2) all the cell types that innervate the protocerebral bridge are likely known (Wolff, Iyer, and Rubin 2015), alongside the projection patterns between the bridge and the ellipsoid body. It remains possible that the heading signal is generated elsewhere, and then sent to the ellipsoid body and protocerebral bridge.

However, given that the P-ENs possess the appropriate properties for rotating the E-PG activity peak in the ellipsoid body and the bridge (Chapter 3), it seems likely that the heading signal is “operated on” within the bridge – ellipsoid body circuit, and that the other essential features of the heading signal are also generated within these two interconnected structures. Indeed, it turns out that reasonable models for generating the heading signal can be built using the known cell types in this circuit, which is the focus of this chapter. In any case, that the heading signal is built within the bridge – ellipsoid body circuit will be my assumption throughout this chapter.

Overview of the E-PG heading signal in the central complex

The protocerebral bridge is composed of a linear array of 18 glomeruli that straddle the brain's midline, with 9 glomeruli on each side. The ellipsoid body is composed of a circular array of 8 tiles (shaped like pizza slices), each of which contains 2 wedges (16 wedges total). A single E-PG neuron innervates a single glomerulus in the bridge and a single wedge in the ellipsoid body. E-PGs tile the ellipsoid body and bridge systematically such that each half of the bridge maps to every second wedge along the ellipsoid body. Put another way, E-PG neurons projecting to the left and right bridge innervate alternating wedges in the ellipsoid body.

When imaging E-PG neurons with a calcium indicator, only a fraction of E-PG neurons is active at any given time. These active neurons are positioned

close to each other, producing a single peak of activity in the ellipsoid body. This single E-PG activity peak is present at all times in our experiments. When the fly is stationary, the activity peak is present and stationary. When the fly turns right, the activity peak rotates counterclockwise in the ellipsoid body. The velocity with which the activity peak rotates in the ellipsoid body quantitatively matches the fly's turning velocity, even without landmark cues. In this way, the fly integrates its angular velocity into its angular position, or heading (Chapter 3, Seelig and Jayaraman 2015).

Because the fly has no absolute reference point in the dark, the position of the activity peak tends to drift apart from the fly's virtual orientation over time. However, if the fly is presented with a visual landmark, the position of the activity peak now tracks the angular position of the landmark, and therefore the fly's heading within this virtual environment, without drift over time. The offset between the landmark's angular position and the activity peak in the ellipsoid body differs from fly to fly. In other words, when the bar is directly in front, in one fly the E-PG peak might be at the top of the ellipsoid body whereas in the next fly it might be at the bottom; in both flies the peak would rotate clockwise when the fly turns left, just from a different starting point. In this thesis, I use a bright blue bar as a visual landmark, but the situation is obviously more complex in real life, where there are typically many nearby and distant objects that the system can use as reference points. Importantly, it has been shown that even if multiple landmarks are presented, there is only one stable E-PG activity peak in the

ellipsoid body (Seelig and Jayaraman 2015), arguing that the system's goal is to generate a single heading estimate based on all the available sensory or internally generated information.

E-PGs have very similar dynamics in the protocerebral bridge, except here, E-PG neurons have two activity peaks, one on each side of the bridge, that move to the left or right depending on whether the fly turns right or left, respectively. The same E-PG neurons that are active in the bridge are active in the ellipsoid body (Chapter 3).

Thus, in E-PG neurons alone, many important properties of this system are evident: (1) E-PG activity in the ellipsoid body takes the form of a single peak, with a relatively constant shape, (2) the activity peak persists when the fly is standing in the dark, (3) the activity peak rotates when the fly turns, and (4) the activity peak can be yoked to the angular position by means of a visual landmark. This chapter outlines a framework for how the known cell types in the protocerebral bridge – ellipsoid body circuit might contribute to these properties, based on knowledge of their anatomy and E-PG and P-EN physiology. Many details of this circuit remain unknown – in particular, the connections between cells, and the physiology of the cell types beyond E-PGs and P-ENs. This framework is therefore largely untested, but is presented with the hope of guiding future experiments and analyses. Indeed, it has proven useful so far in guiding my own experiments.

Persistent activity

In “building” the E-PG signal, a good starting point is to ask how E-PG activity is generated – this activity can then be modified in various ways to produce the observed moving activity peak that correlates with the fly’s heading. E-PG activity seems to persist at all times: in the dark, where there is no visual input, and when the fly is standing still, where there are no changing proprioceptive or motor inputs. These observations suggest (but do not unambiguously prove) that E-PG activity is generated as an intrinsic property of the central complex circuit. A simple circuit mechanism to achieve this property is for E-PGs to excite E-PGs at the same locus, either directly or indirectly, thereby creating a positive feedback loop that generates E-PG activity. This could occur through two known anatomical paths. First, E-PGs seem to have both dendrites and axon terminals in the ellipsoid body (Atsuko Adachi, personal communication and Lin et al. 2013), which may allow E-PGs to directly excite each other at the same locus (Figure 5.1a). It is also worth noting that the E-PG arbor in the ellipsoid body is not perfectly contained within a single wedge, but in fact bleeds into neighboring wedges (Figure 10 in Wolff et al. 2015). This anatomical spread might allow E-PGs to not only excite (or be excited by) E-PGs in the same wedge but also neighboring wedges, reinforcing activity in a cluster of wedges rather than in a single, self-contained wedge. A second anatomical path for explaining persistent activity in E-PGs is based on the description of another cell class by Wolff et al. (2015), called P-EGs (protocerebral-bridge-ellipsoid-body-gall

neurons) that interconnect the bridge and ellipsoid body (Figure 5.1b). Like E-PGs, a single P-EG neuron innervates a single glomerulus in the bridge, but unlike E-PGs, a P-EG neuron innervates an entire tile (or 2 wedges) in the ellipsoid body. Furthermore, P-EGs likely receive inputs from the bridge and send outputs to the ellipsoid body (Wolff, Iyer, and Rubin 2015), the opposite flow of information predicted for E-PGs. If one follows an E-PG neuron and a P-EG neuron innervating the same glomerulus in the bridge, the two neurons also overlap in the ellipsoid body, with the E-PG neuron innervating one wedge within the same tile innervated by the P-EG neuron (Figure 5.1b). For example, E-PGs in wedge L5 in the ellipsoid body project to glomerulus 5 in the left bridge. P-EGs innervating glomerulus 5 in the left bridge project to tile 5 in the ellipsoid body, which includes wedges L5 (the starting point for the E-PG neuron) and R5. If E-PGs and P-EGs reciprocally excite each other, a positive feedback loop would maintain an activity peak in the absence of external inputs. A third possibility for recurrent excitation is through P-EN1s. Although P-ENs from the left- and right-bridge project to either side of the E-PG activity peak (Figure 3.9), the sum of their activities in the ellipsoid body remains centered on the E-PG activity peak, provided the fly is not turning (Figure 3.9). Although the projection of P-EN activity to the ellipsoid body is broader than the original E-PG peak (Figure 3.9), the E-PG activity may be reshaped by inhibitory feedback in the ellipsoid body (see below). One reason to discount the relative importance of this mechanism is that P-EN1s are particularly weak when the fly is not turning, and thus may only play a strong

role as the fly turns. On the other hand, when P-ENs were inhibited with *shibire*^{ts}, E-PG activity tended to decrease when the fly was in the dark, particularly at higher temperatures (Figure 3.12). This effect may be due to the E-PG activity peak becoming unstable because of a lack rotational control from the integration system, or it may be due to generally lower levels of activity because of a loss of an excitatory input. A fourth possibility is that E-PGs or P-EGs (or both) are intrinsically active without synaptic inputs. On its own, however, this mechanism would not explain why only one E-PG active peak is observed, because E-PGs with a tendency to be persistently active would mean that each E-PG neuron is active independent of the activity of all the other E-PG neurons. If intrinsic membrane properties of E-PGs mediated the persistent activity, then the rule that only one bolus of activity is observed in the ellipsoid body would have to be achieved by other means, like structured inhibition in the form of lateral inhibition (see below) or structured excitation in the form of recurrent excitation acting on local and neighboring wedges (e.g. P-EGs, P-ENs, E-PG arbors that bleed into neighboring wedges). These four options for explaining persistent activity are also not mutually exclusive, and may each play a part in fine-tuning the shape and general levels of activity in this highly recurrent circuit.

Figure 5.1 | A framework for building a heading signal with known cell types.

a, Persistent activity in E-PG neurons through E-PG↔E-PG local excitation, within and across wedge boundaries. **b**, Persistent activity in E-PG neurons through E-PG→P-EG excitation in the bridge, and the return P-EG→E-PG excitation in the ellipsoid body. **c**, Lateral inhibition through the local neurons, or "Δ7" neurons, in the bridge. Δ7 neurons output anti-phase (or 4 glomeruli) relative to where they receive inputs. "Δ7" refers to the 7-glomerulus spacing in between synaptic outputs in a single neuron. These outputs thus have a periodicity of 8, closely matching the periodicity in E-PG and P-EN activity. **d**, Global inhibition through the ring neurons in the ellipsoid body. Each ring neuron takes input from one microglomerulus in the lateral triangle, and outputs to all angles in the ellipsoid body. **e**, Integration through an asymmetry in P-EN activity, driving a directional shift in the E-PG peak. **f**, Turning-related asymmetric input into P-EN neurons through SPS-P neurons that each output to one half of the bridge. Only P-EN neurons that are also excited by the E-PG neurons (directly or indirectly) fire due to an asymmetric input. **g**, Landmark association through ring neurons innervating all angles in the ellipsoid body. Ring neurons receive inputs from one microglomerulus, each of which responds to a specific feature at a specific retinal position (Seelig and Jayaraman 2013). Synapses between ring neurons and E-PGs are modulated over time to "associate" visual features at specific retinal positions to specific E-PG neurons, or internal heading estimates. Solid lines delineate glomeruli in the protocerebral bridge and tiles in the ellipsoid body. Dashed line delineate wedges (half-tiles) in the ellipsoid body.

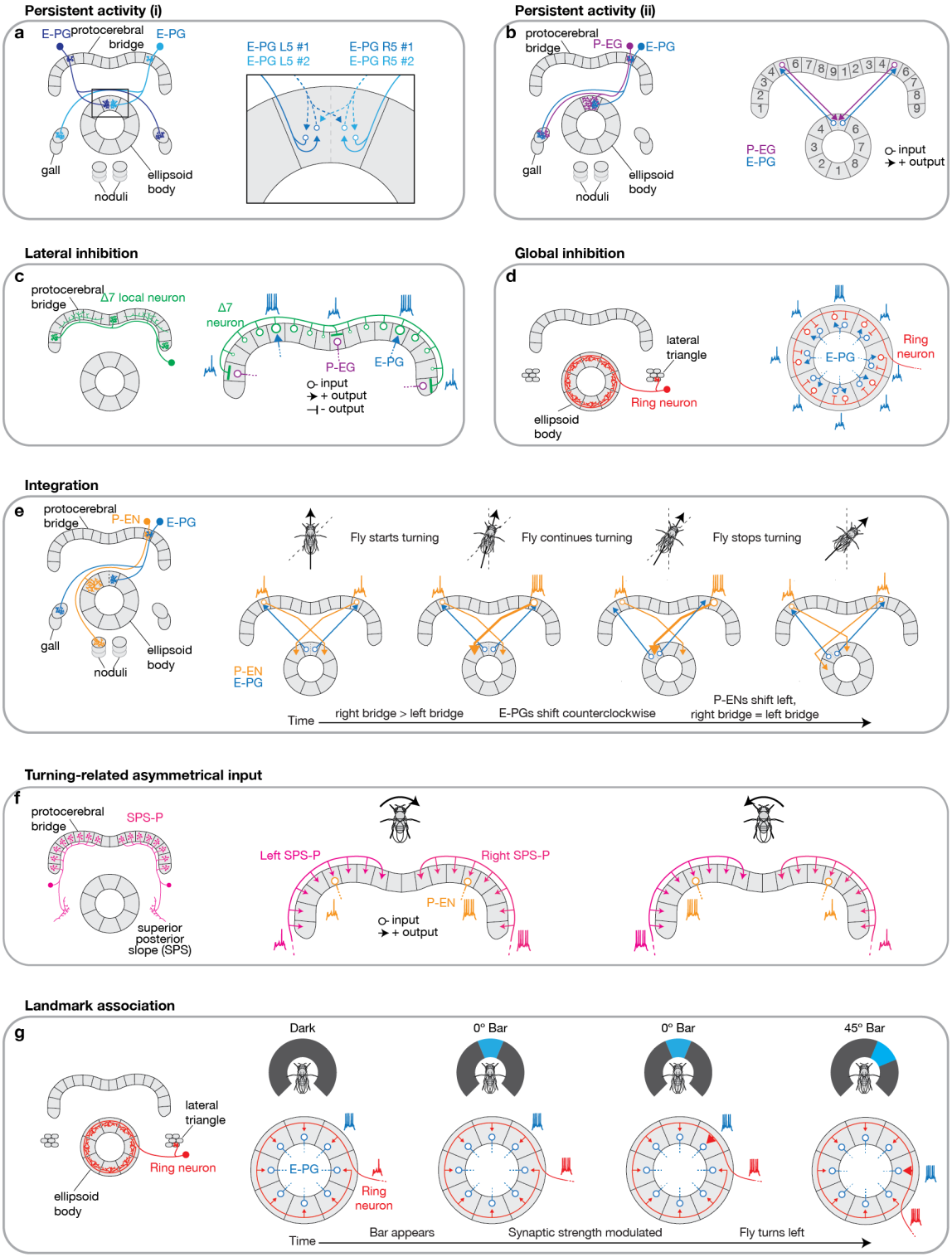
Persistent activity (i)
a
E-PG
protocerebral bridge
E-PG
gall
noduli
ellipsoid body
E-PG L5 #1
E-PG L5 #2
E-PG R5 #1
E-PG R5 #2
Persistent activity (ii)
b
protocerebral bridge
P-EG
E-PG
gall
noduli
ellipsoid body
P-EG
E-PG
input
+ output
Lateral inhibition
c
protocerebral bridge
Δ7 local neuron
Δ7 neuron
P-EG
E-PG
input
+ output
- output
Global inhibition
d
lateral triangle
Ring neuron
ellipsoid body
E-PG
Ring neuron
Integration
e
protocerebral bridge
P-EN
E-PG
gall
noduli
ellipsoid body
Fly starts turning
Fly continues turning
Fly stops turning
P-EN
E-PG
Time
right bridge > left bridge
E-PGs shift counterclockwise
P-ENs shift left, right bridge = left bridge
Turning-related asymmetrical input
f
protocerebral bridge
SPS-P
superior posterior slope (SPS)
Left SPS-P
Right SPS-P
P-EN
input
+ output
Landmark association
g
lateral triangle
Ring neuron
ellipsoid body
Dark
0° Bar
0° Bar
45° Bar
E-PG
Ring neuron
Time
Bar appears
Synaptic strength modulated
Fly turns left

Shaping activity through lateral or global inhibition

While E-PG neurons in one locus in the ellipsoid body are active, all other E-PG neurons are inactive. When the fly turns, some E-PG neurons that were previously inactive become active and vice versa. A feedback mechanism seems to constrain the number of active E-PG neurons, and furthermore to ensure that these active E-PG neurons are all clustered at the same position in the ellipsoid body and protocerebral bridge. One mechanism to achieve this property is for active E-PG neurons to suppress all *other* E-PG neurons, a process known as lateral inhibition (Figure 5.1c). A second mechanism is for active E-PG neurons to suppress *all* E-PG neurons, including the active subset, which is called global inhibition (Figure 5.1d). Lateral inhibition could be achieved through the protocerebral bridge local neurons (PB18.s-GxΔ7Gy.b), which appear to send outputs anti phase (i.e. glomerulus i+4) with respect to where they receive inputs (i.e. glomerulus i) in the bridge (Figure 5.1c, Figure 18B in Wolff et al. 2015). Collectively, the bridge local neurons output to the entire bridge. Lateral inhibition through local neurons might work in the following way. If local neurons were excited by E-PGs and inhibited P-EGs, then an E-PG activity peak at glomerulus 2 in the bridge would suppress P-EG activity at glomerulus 6 in the bridge through the action of local neurons. If E-PGs and P-EGs reciprocally excite each other (as described above), inhibiting one cell type would effectively inhibit both, and suppress E-PG activity anti phase with respect to the E-PG activity peak. Alternatively, local neurons could also directly inhibit E-PGs at glomerulus 6, if E-

PGs were to also receive inputs in the bridge. That the local neuron inputs are fairly broad (Figure 18B in Wolff et al. 2015) suggests that their collective output is considerably broader than the width of the E-PG activity peaks in the bridge, which might be necessary for restricting the E-PG activity to its observed width.

A second possibility is that active E-PGs suppress *all* E-PGs, including the active E-PGs, through global inhibition via neurons that innervate the entire protocerebral bridge or the entire ellipsoid body (Figure 5.1d). Several candidates may fill this role based on their anatomy. For example, dopaminergic neurons innervate the entire bridge (Wolff, Iyer, and Rubin 2015) or the entire ellipsoid body (Kong et al. 2010). A second set of possibilities are the ellipsoid body ring neurons, which innervate single microglomeruli in the lateral triangle and concentric rings in the ellipsoid body (Seelig and Jayaraman 2013). Many ring neurons are immunopositive for the generally inhibitory neurotransmitter GABA (Z. Zhang et al. 2013), and are therefore poised to globally inhibit ellipsoid body-innervating neurons. For example, if ring neurons are excited by E-PGs from each wedge and, in turn, inhibit E-PGs in all wedges, an E-PG activity peak in one locus would inhibit E-PG activity everywhere, including itself. The recurrent activity of E-PGs within the active locus (see persistent activity), would necessarily have to exceed the inhibition from the ring neurons at the location of the activity peak for this mechanism to work in explaining persistent activity. It is worth noting that such a mechanism would not in itself enforce a single peak, like the bridge local neurons would. However, if combined with local recurrent excitation between

neighboring wedges, for example through E-PG arbors that bleed into neighboring ellipsoid body wedges (see above), a single E-PG activity peak could be enforced.

Integration

Once the shape and persistence of the E-PG activity peak is established, it has to be moved around the protocerebral bridge and ellipsoid body to track the fly's heading. When the fly turns right, the E-PG activity peak rotates counter-clockwise in the ellipsoid body and leftward in the protocerebral bridge with a velocity that matches the fly's turning velocity (Figure 3.13g). How does the activity peak rotate in the correct direction with the correct velocity? The cell type that likely mediates this property is the P-EN cell class (Figure 5.1e and Chapter 3). A single P-EN neuron takes input from a single glomerulus in the bridge and outputs to a single tile in the ellipsoid body. P-ENs are different from E-PGs and P-EGs, however, in that left P-ENs project clockwise and right P-ENs project counter-clockwise from the bridge to the ellipsoid body. For example, whereas an E-PG neuron from wedge L5 in the ellipsoid body projects to glomerulus 5 in the left bridge, a P-EN neuron from glomerulus 5 in the left bridge projects to tile 6 in the ellipsoid body, thus projecting clockwise. The opposite is true for right-bridge P-ENs: a P-EN neuron from glomerulus 5 in the right bridge projects to tile 4 in the ellipsoid body, thus projecting counterclockwise. No other known cell type has this crucial anatomical property. If E-PGs and P-ENs reciprocally excite each

other, an E-PG activity peak can propagate clockwise or counterclockwise in the ellipsoid body through an asymmetry in the activity of these clockwise- and counterclockwise-projecting P-EN neurons. Such an asymmetry exists in the P-EN neurons, and is time-locked to moments when the fly turns, with the correct sign to rotate the E-PG activity peak in the expected direction. This asymmetry quantitatively matches the fly's turning velocity, as expected if such an asymmetry is to quantitatively integrate the fly's turns (Chapter 3).

A twist is that P-EN neurons exist in two subtypes, which can be differentiated based on their physiology. The first (P-EN1) has an asymmetry in its activity that is biased to the leading edge of a moving E-PG activity peak in the ellipsoid during a turn, and comes on at the beginning of each turn. The second (P-EN2) has an asymmetry that is biased to the trailing edge, and comes on at the end of each turn. These physiological properties suggest a role for P-EN1s and P-EN2s in starting and stopping the E-PG activity peak at the beginning and end of a turn, respectively. Yet, it is not obvious whether the E-PG activity peak requires a stopping mechanism, which would imply that the E-PG activity peak would otherwise continue rotating and overshooting the correct position. Future experiments will be needed to fully clarify the roles of the two P-EN subtypes (especially P-EN2s).

How do P-ENs receive an asymmetric input when the fly turns? Since clockwise- and counterclockwise-projecting P-ENs are segregated in the left and right bridge, the neuron delivering an asymmetric input could innervate the entire

left or the entire right bridge. Indeed, neurons projecting from the superior posterior slope (SPS) to the protocerebral bridge, called SPS-P neurons, fit this criterion (Figure 5.1f). One would predict that during a right turn, the right-bridge-innervating SPS-P neuron becomes more active than its counterpart on the left, and vice versa during a left turn (assuming excitatory interactions between SPS-Ps and P-ENs).

Landmark tracking

When the fly is in the dark, the E-PG phase drifts apart from the fly's heading over time, because the fly has no feedback as to its absolute heading. When a visual feature is presented to the fly in closed-loop, as if it were a stationary object in the real world, the E-PG activity peak matches the angular position of this visual cue (Figure 3.1), with an offset that is typically constant from trial to trial, but that can change if the cue is absent for long periods of time (Figure 4.3). This offset is also different from fly to fly (Figure 4.1). Furthermore, multiple visual features do not produce multiple E-PG activity peaks – only a single E-PG activity peak is ever present (Seelig and Jayaraman 2015).

How do these properties arise? One potential solution is that each landmark position sends an input to a specific locus in the bridge or ellipsoid body. Since different flies have different mappings between the position of the landmark and the E-PG activity peak, this wiring would have to be different for

each fly. This mechanism is also inconsistent with the observation that the offset can change over time within a fly (Figure 4.3).

A second potential solution is that each landmark position sends inputs to the entire bridge or ellipsoid body, and these inputs are modified as the fly explores its environment and associates different visual features with different internal heading estimates (Figure 5.1g). A specific mechanistic model for how this association might work is as follows. Since an E-PG activity peak is present at all times, the activity peak will happen to be at some position the moment a visual feature appears. At that moment, two sets of neurons are simultaneously active: the “visual feature” neuron that responds to that position of the visual feature on the retina, and the set of active E-PG neurons that make up the E-PG activity peak. The synapses from the active visual feature neuron that connect to the active E-PGs then become strengthened, effectively associating this visual feature at that retinal position with that heading estimate (or E-PG neurons). The next time this visual feature appears at this position on the retina, the visual feature neuron will drive activity in the same E-PG neurons. As the fly changes its heading, the E-PG activity peak rotates in the ellipsoid body, and the visual feature rotates on the retina; the connections between these co-active pairs of E-PG neurons and visual feature neurons in turn become strengthened. The range of visual feature positions can thus be mapped to the range of E-PG neurons. In this way, the offset, or mapping, between the position of the landmark and the E-PG activity peak is initialized when the landmark is first presented to the fly;

indeed, the E-PG phase interacts differently with the bar during its first presentation compared to subsequent presentations, after the mapping is set (Figure 4.3).

This mechanism would explain why the mapping is different in each fly, since when the bar first appears, its location is random, both on the arena (because the bar is controlled by the fly), and with respect to the fly's internal heading estimate. This mechanism also explains how multiple visual features (of which there are presumably many in the fly's natural environment) can be mapped to a single, coherent heading estimate, since each visual feature, and each visual feature position, is mapped independently to the same heading estimate. Another feature of this model is that visual features that are not well correlated with the fly's heading are not strongly mapped to the E-PG heading estimate. This simple property would allow the fly to ignore moving objects, like other animals, while at the same time using static landmarks in its environment to calibrate its internal heading estimate.

The main candidate cell class to implement these properties are the ellipsoid body ring neurons (Figure 5.1g). Each ring neuron innervates one ring with a specific radius, spanning the entire range of angles in the ellipsoid body. Importantly, ring neurons respond to visual features with small receptive fields that tile azimuthal and vertical space. They are numerous, which could provide support for different visual (or other) features at many azimuthal positions. Ring neurons have been implicated in place (Ofstad, Zuker, and Reiser 2011) and

orientation (Neuser et al. 2008) memories, consistent with a role in learning the orientations of landmarks. Finally, ring neurons express both NMDA receptor subunits (Wu et al. 2007), which are implicated in coincidence detection (Malenka et al. 1989), the fundamental learning rule in the association model described above.

One issue with this model is that NMDA receptors are expected to be localized on the postsynaptic cell, which, in the model above, is the E-PG neuron and not the ring neuron. One way to resolve this issue is for ring neurons to receive an additional presynaptic input from E-PG, or E-PG-like, neurons (this configuration is described in more detail in the Chapter 4 Discussion). This circuit diagram is incidentally very similar to the one for global inhibition, where E-PGs both output to and receive inputs from (directly or indirectly) ring neurons. If the same ring neurons are used for both landmark association and global inhibition, the inhibition may no longer be strictly global, since the landmark association model assumes that synaptic strengths are modulated along the ring. I also note that, if the visual feature neuron is inhibitory, as this specific model would suggest, the ring neuron-to-E-PG synapse should *decrease* in strength as a function of coincident activity between the two cells to achieve the same property – in other words, less inhibition (and therefore more excitation) where the visual feature neuron and the E-PG neuron are co-active.

Similarities in physiology between the fly and rat head direction system

The physiological properties of E-PG neurons are remarkably similar to that of head direction cells in rats. E-PGs from a single glomerulus and single head-direction cells respond to a specific range of bar, or cue, positions with a roughly Gaussian-shaped response curve (Figure 3.4, Taube, Muller and Ranck 1990a). If the cue is rotated, the preferred firing direction of E-PGs and head-direction cells follows the rotation of the cue (data not shown, Seelig and Jayaraman 2015, Taube, Muller and Ranck 1990b). The heading signal in E-PGs and head direction cells persists in the dark, although it drifts over time relative to the animal's absolute position in its environment (Figure 3.3, Figure 3.7, Seelig and Jayaraman 2015, McNaughton and Chen 1991, Mizumori and Williams 1993). Moreover, the preferred firing directions of E-PGs from different glomeruli and of different head direction cells are maintained relative to each other across environmental perturbations – in other words, if two E-PG neurons or head direction cells have preferred firing directions that are 90º apart in one environment, they will continue to have the same relative separation of 90º in a second environment, even though their mapping with respect to the environment is seemingly arbitrary (Figure 4.3, Seelig and Jayaraman 2015, Taube, Muller and Ranck 1990b). These results indicate that E-PG and head-direction cells rotate their preferred firing directions coherently as a unit.

In turn, the physiological properties of P-EN neurons strongly resemble that of head direction cells located in the lateral mammillary nucleus (LMN). P-ENs in the left- and right-bridge are asymmetrically active when the fly turns left or right. Similarly, two studies have shown that head direction cells in the left and right LMN are differentially active when the rat's head turns left or right (Stackman and Taube 1998; Blair, Cho, and Sharp 1998). Both studies observe a shift in the preferred firing direction of head direction cells in the LMN during right and left head turns. These shifts are reminiscent of the shifts in the P-EN1 or P-EN2 activity peak relative to the E-PG activity peak in the ellipsoid body when the fly turns, and perhaps serve the same function to shift the head direction system in the correct direction with the correct speed. Stackman and Taube 1998 also observed differences in the peak firing rate of head direction cells when the rat's head turned right vs. left, which is also consistent with the different calcium activity levels observed in left and right P-ENs (defined as P-ENs whose cell bodies are in the left or right hemisphere) during turns. Moreover, the LMN appears to be the only area where both angular head velocity cells and head direction cells have been observed (although the entire mammalian brain has not been explored in this regard, comprehensively), and is therefore likely where angular head velocity is integrated into head direction (Taube 2007). Consistent with this idea, an intact LMN appears to be required for the head direction signal in downstream areas, like the anteriodorsal thalamic nuclus (ATN) (Blair, Cho, and Sharp 1998). The fine-scale anatomy for how angular

head velocity signals are combined with head direction signals remains unknown in the rodent head direction system.

Similarities between models for the heading system in flies and rodents

The core model for rat head direction cells is outlined in Figure 3 in Skaggs et al. 1995, adapted in Figure 5.2a. “Classical” head direction cells, which respond selectively to the animal’s head direction, are arranged in a circular network – although there is no known anatomical basis for this arrangement in rodents. Head direction cells excite each other locally, and inhibit each other distally (i.e. everywhere else around the ring). Given the correct tuning of synaptic weight parameters, these two properties ensure that only one peak of activity along the ring is stable over time. These two properties might in practice be implemented by two or more different cell types in *Drosophila*, as outlined above in this Discussion. For example, local excitation might be implemented by direct connections between E-PGs, or positive feedback from P-EGs and even P-ENs (see Persistent activity, Figure 5.2b). Lateral inhibition would most likely be implemented by the protocerebral bridge local neurons (or “Δ7” neurons). A second option is for global inhibition to be implemented by a cell type such as the ellipsoid body ring neurons (see Shaping activity through lateral or global inhibition) (Figure 5.2b).

In order for the activity peak to rotate in response to the animal turning, thus shifting the animal's internal heading estimate, Skaggs et al. add a set of rotation cells, which receive inputs from head direction cells at a given position in the ring and project clockwise or counterclockwise to the neighboring head direction cells in the ring (Figure 5.2a). When the rat's head turns right, the clockwise-projecting rotation cells at the activity peak become more active than their counterclockwise-projecting counterparts, thus shifting the head direction cell activity peak clockwise. In *Drosophila*, P-ENs are the strongest (and perhaps the only) candidate to implement this function, given their physiology and anatomy (Figure 5.2b). The balance of activity between clockwise- and counterclockwise-projecting rotation cells is determined by inputs that are sensitive to the animal's angular head (or body) velocity (called vestibular cells in Figure 5.2a): one input innervates all clockwise-projecting rotation cells, and the second input innervates all counterclockwise-projecting rotation cells. In *Drosophila*, this asymmetric input might be carried by the SPS-P neurons (Figure 5.1f), each of which innervates one side of the bridge (specifically, the outer 8 glomeruli innervated by P-ENs), and therefore either all clockwise- or all counterclockwise-projecting P-EN neurons (Figure 5.2b). This asymmetric input may, however, also be carried by other neurons that provide input to the protocerebral bridge and that are modulated in a left/right manner.

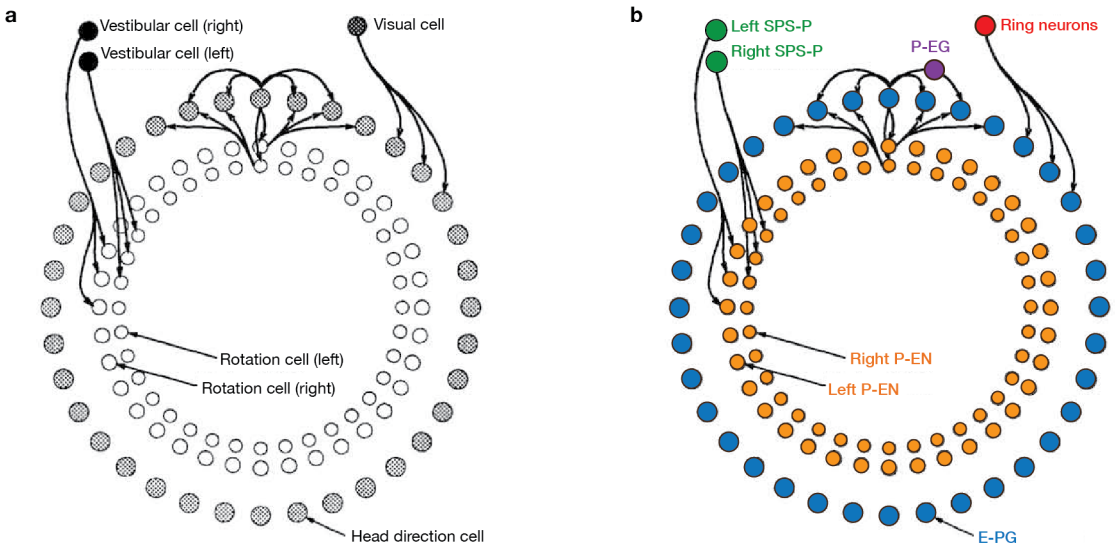

Adapted from Skaggs et al. 1995 Figure 3

Matching central complex cell types with Skaggs model

Figure 5.2 | Similarities between models for the fly and rat heading systems

a, Adapted from Figure 3 in Skaggs et al. 1995. Model for how the rat head direction signal is built, based on head-direction cell physiology. **b**, Mapping the cell types in the *Drosophila* protocerebral bridge – ellipsoid body circuit onto the model from Skaggs et al. 1995. The physiology for E-PGs and P-ENs is presented here and in Seelig and Jayaraman 2015, while the physiology for the other cell types remains unknown. The anatomy of the *Drosophila* cell types in **b**, are discussed in Figure 5.1.

Finally, in order for the head direction system to respond to visual landmarks, Skaggs et al. proposed a set of "visual cells" that send synaptic outputs to all head direction cells. Each visual cell responds to a particular feature at a particular retinal position (Figure 5.2a). Visual cells collectively respond to the range of relevant visual features and tile retinal space. The visual cell → head direction cell connections are then modulated as a function of coincident activity between the two cells, such that a coherent mapping is generated between the animal's visual environment and its internal heading estimate over time as the animal explores its environment. Because of their number, anatomy and physiology, ellipsoid body ring neurons seem the best poised to fulfill this role (Figure 5.2b, see Chapter 4 and Landmark tracking in this Chapter)

Perhaps it should be no surprise that if the physiological properties of heading-sensitive cells in *Drosophila* are so similar to those of head direction cells in rats, then the models proposed to account for these properties should also be similar. I note, however, that the *Drosophila* model was arrived at independently by analyzing the physiological and anatomical properties of P-EN and E-PG cells (I was fairly ignorant of rodent head direction cell models before realizing that the *Drosophila*- and rodent-inspired models were so similar, thanks to Christoph Kirst). That an independently-derived and anatomically-inspired model for the *Drosophila* heading system happens to match, at its core, the models proposed for the rat head direction system seems to support the

hypothesis that mammals and flies compute an internal heading estimate in a fundamentally similar way. However, it should be noted that the *Drosophila* model is not yet fully verified, and that even more work is needed to independently assess this claim in the rodent head direction system. Nevertheless, these results provide unprecedented similarities, and, most provocatively, hint at potential homologies, between the mammalian and insect navigational systems.

Extending the heading model to compute other variables

Another interesting point is that the core features of this circuit model may apply to other neuronal processes other than computing one's heading. In a sense, heading is one of the simplest variables to compute, since it is one-dimensional and only takes on a fixed range of values because it is periodic. But the simple framework of shifting a peak of activity to encode a variable may also apply to computing other variables, such as one's position in space, a two- (or three-) dimensional variable which, in principle, can take on ever-increasing values. Indeed, attractor models for grid cells are fundamentally two-dimensional extensions of the one-dimensional head direction cell model (McNaughton et al. 2006). Grid cells are periodically active, forming a hexagonal pattern of activity over two-dimensional space (Hafting et al. 2005). A simple model for this hexagonal structure is to suppose that grid cells excite each other within short distances, but inhibit each other further out in a ring, with few or no connections

past a certain distance (similar to head direction cells, except that the inhibition is limited to a certain distance). This arrangement of connections can lead to multiple activity peaks, and various patterns of activity, including alternating stripes of activity and inhibition (like ocular dominance columns in visual cortex) and the hexagonal grid of activity peaks seen in grid cells (McNaughton et al. 2006). The activity peaks can be shifted across the two-dimensional network through two orthogonally projecting sets of shifting neurons (analogous to the one set of "rotation" or P-EN neurons in the heading system models described above) – in other words, one for moving in x and one for moving in y. The relative activity between these right/left and up/down shifting neurons would be related to the animal's heading and speed. Consistent with this notion, grid cells are intermingled with head direction and speed cells, suggesting that the animal's 2D velocity vector is used to compute its position. In this way, an activity peak could move in two dimensions in response to the animal's two-dimensional displacements.

Computing on the heading signal to produce behaviorally meaningful signals

One can go even further, and speculate how these activity peaks can be computed on to generate behaviorally meaningful signals. It is one thing to generate a neuronal heading signal, but this signal is of no use if it just sits in the middle of the brain without in some way informing the animal's behavior. The

immediate, proximal motor decisions made by a navigating animal are how much to turn left or right, or go straight at each point in time – whether it is randomly searching for food or migrating across an ocean. Heading and position signals are abstractions that are useful as *feedback* to these primary turning motor decisions, but without this link to behavior they are of no use in themselves. This section describes one idea for how this link could be made.

In thinking about mechanisms for how an abstract heading signal is converted into a turning signal, it is useful to differentiate between one's *current* heading and one's *target* heading. The *target* heading is the heading that the animal attempts to maintain, and that presumably directs it along the shortest path towards its target location (like its home, or food, see Chapter 1). The goal of the animal in this case is to match its *current* heading estimate with its *target* heading. Taking the fly circuit as a concrete example, a target heading signal could be "layered" onto the ellipsoid body as a second activity peak, carried by a different set of "target" neurons. The "target" activity peak's angular position is within the same frame of reference as the current heading estimate signal (i.e. the E-PG activity peak), since it is overlaid on the same structure. The goal of the animal is then to turn left or right in order to match the E-PG phase (which is controlled by turning) with the target phase (which is *not* controlled by turning). The output of this circuit could be a simple "turning drive" signal that drives the fly to turn left or right as a quantitatively varying function of the relative offset between the E-PG and target phases. If the E-PG phase is positioned

counterclockwise relative to the target phase, then the fly should turn left to move the E-PG phase clockwise, towards the target phase, and vice versa if the E-PG phase is positioned clockwise relative to the target phase. The further the E-PG phase is from the target phase, the stronger the “turning drive” might be; one would want to turn slower as one nears the target in order to not overshoot it. Such an arrangement effectively creates a closed-loop system that controls the fly’s heading. To change its heading, the fly would simply move the position of the target activity peak, and the system then attempts to turn the fly towards this new target heading. How this target heading is computed in the first place is not yet known, but might be derived from the position of the animal relative to a target location, as described in Chapter 1. This idea is consistent with the observation in Chapter 3 (Figure 3.19) that the fly turns in response to a stimulated change in the E-PG phase, and in a direction that would return the E-PG phase back to its original position, consistent with the central complex having a “target” heading signal.

How could the target heading signal and the current heading signal interact to produce a “turning drive” signal? As described above, the turning drive signal should change sign (i.e. from “turn left” to “turn right”) when the E-PG phase appears clockwise or counterclockwise relative to the target phase. One implementation of this computation is to effectively run P-ENs “backwards”. P-ENs effectively copy the E-PG peak twice, one for each side of the bridge, projecting each peak to either side of the original E-PG peak in the ellipsoid body

(Figure 3.9). Taking P-EN2s as an example, the P-EN2 peak in the left bridge projects to the counterclockwise side of the E-PG peak in the ellipsoid body, and vice versa for the right bridge P-EN2 peak (Figure 5.3a-b). If, then, the E-PG peak appears counterclockwise relative to the target peak in the ellipsoid body, the P-EN2s receiving phase inputs from the right bridge, but not the left bridge, overlap with the target peak (Figure 5.3c). If P-EN2s were to receive excitatory inputs from the target cells in the ellipsoid body, then the right P-EN2s would become more active than the left P-EN2s (Figure 5.3c). Conversely, the left P-EN2s would become more active if the E-PG peak appears clockwise relative to the target peak (Figure 5.3e). If the E-PG and target peaks are aligned, P-EN2s would not be asymmetrically active (Figure 5.3d). In this way, the right-left asymmetry in P-EN2s would satisfy the properties for the “turning drive” signal described above, and would in effect compute this signal given a target phase in the ellipsoid body. Interestingly, P-ENs (both P-EN1 and P-EN2) output to a third structure, the noduli, which pool the left and right P-ENs separately. The turning drive toward the goal could be easily extracted from comparing the summed activity in the left and right noduli. Unlike the model described in Chapter 3, this model predicts that the P-EN2 asymmetry arises from intrinsic interactions within the ellipsoid body and not from an external asymmetric input to the bridge.

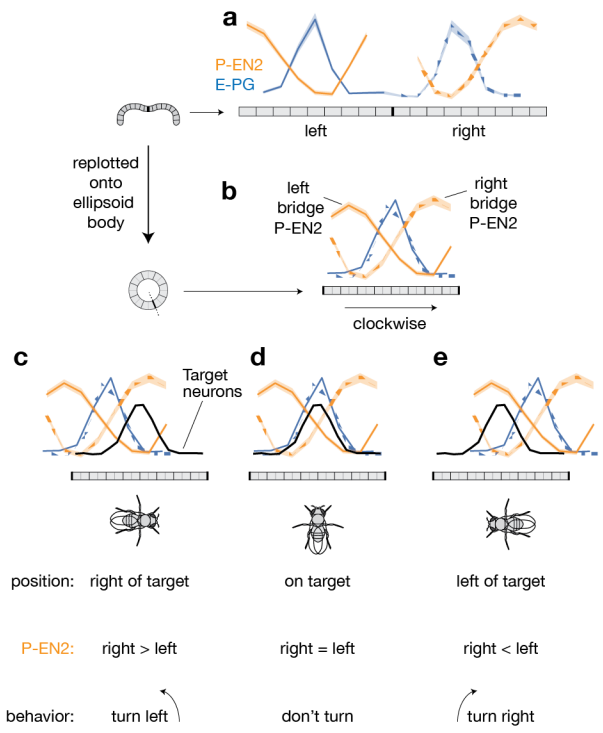

Figure 5.3 | Model for behavioral control of heading

a, Phase-nulled E-PG and P-EN2 signals in the bridge, averaged over time. **b**, Bridge data from **a** replotted onto the ellipsoid body using each cell type's anatomical projection pattern (Wolff, Iyer, and Rubin 2015). **a-b** reproduced from Figure 3.9. **c**, Same as **b**, with activity in postulated "target neurons" in black. E-PG phase is offset 90º counterclockwise relative to the target phase, meaning the fly is oriented 90º clockwise relative to its target heading. The target activity peak overlaps with the right P-EN2 peak. Supposing the target cells excite P-EN2s in the ellipsoid body, the right P-EN2s will become more active than the left P-EN2s. The fly should turn left to reach its target heading. **d**, Same as **c**, except the E-PG and target phases are aligned. P-EN2s are not asymmetric, and the fly should not turn. **e**, Same as **c**, except the E-PG phase is offset 90º clockwise relative to the target phase. The target peak overlaps with the left P-EN2 peak, and the left P-EN2s become more active than the right P-EN2s. The fly should turn right.

This model makes some predictions that are consistent with P-EN2 properties, including the late timing of their asymmetry (the turning drive should increase as the fly moves away from its goal, late during a turn) and the fact that (unphysiologically) strong stimulations can drive the fly to turn in the expected direction based on this model (Figure 2.2).

This turning drive model is difficult to validate, however, without experimental access to the postulated "target" neurons. One way to bypass this issue is to analyze times when the fly maintains a constant heading, and therefore where the "target" heading angle can be inferred from the fly's behavior. At first glance, it appeared to me that the P-EN2 asymmetry might be consistent with the turning drive model in that the P-EN2 asymmetry changed sign as the fly's heading oscillated on either side of the inferred target heading (e.g. the behavior in Figure 3.15a-b). However, during longer behavioral deviations from the inferred target angle, I found that the P-EN2 asymmetry resolved quickly, sometimes seconds before the animal behaviorally corrected itself and returned its heading toward the goal, which is inconsistent with the P-EN2s carrying an error-from-goal signal in their [Ca^{2+}] levels. Moreover, the P-EN2 asymmetry reappeared during the return turn of the fly to the inferred target, where one would have expected an already present asymmetry to disappear. These interpretations are limited by the fact that we are inferring the fly's target heading from its behavior. One may be able to test these ideas more rigorously

by discovering the cells that carry the target heading angle (perhaps residing in the ellipsoid body or fan-shaped-body).

Even if this model does not apply to P-EN2s, it is presented as a possible framework that may apply to other cell types, or other neuronal systems, to mediate goal directed navigation. More generally, this model introduces the idea of multiple “layers” of activity peaks that can move independently of each other with respect to environmental, behavioral or internal variables, but that can also interact with each other to produce new and potentially behaviorally meaningful signals, such as whether to turn left or right, and by how much.

Conclusions

This thesis describes the discovery of an internal sense of heading in the fruit fly, *Drosophila melanogaster*, and how this internal heading estimate rotates when the fly turns. Further experiments argue that visual landmarks are associated with this internal heading estimate over time, and a model for how this process could work is presented. The proposed neuronal circuit architectures for the fly heading system share fundamental similarities with those proposed for head direction cells in mammals, and point to mechanistic links between spatial navigation in mammals and insects.

Methods

Fly stocks

Flies were raised with a 12 hour light, 12 hour dark cycle at 25ºC. All physiological experiments were performed with 1-3 day old females. In Chapter 3 each fly had at least one wild-type white allele. Flies were selected randomly for all experiments. I was not blind to the flies' genotypes. For the behavioral stimulation experiments (Figure 2.2) I used w ; NP0212-Gal4 / UAS-mCD8GFP ; + / UAS-P2X2 flies. For the initial imaging experiments (Figure 2.3), I used w ; NP0212-Gal4 / + ; + / UAS-GCaMP6f (Bloomington Drosophila Stock Center, BDSC #52869) flies. For experiments imaging one cell type (Figure 3.1, Figure 3.5e-m, Figure 3.13a-d, Figure 3.2, Figure 3.3, Figure 3.4, Figure 3.7, Figure 3.8, Figure 3.11a-f, Figure 3.13, Figure 3.19, Figure 4.3), I used + (Canton S, Heisenberg Lab) / w ; UAS-GCaMP6m (Bloomington Drosophila Stock Center, BDSC #42748) ; VT032906-Gal4 (Vienna Drosophila Resource Center, VDRC #202537) for P-EN1, + / w ; 60D05-LexA (BDSC #52867) / LexAop-tdTomato (Ruta Lab) ; VT020739-Gal4 (VDRC #201501) / UAS-GCaMP6m (BDSC #42750) for P-EN2, and + / w ; + ; 60D05-Gal4 (BDSC #39247) / UAS-GCaMP6m flies for E-PG. For imaging P-EN1 or P-EN2 simultaneously with E-PGs (Figure 3.9, Figure 3.12), I used + / w ; 60D05-LexA / LexAop-GCaMP6f (BDSC #44277) ; VT032906-Gal4 / UAS-jRGECO1a (BDSC #63794), and + / w ; 60D05-LexA / LexAop-GCaMP6f; VT020739-Gal4 / UAS-jRGECO1a flies, respectively. As a control for differences in calcium indicator kinetics, I imaged

GCaMP6f and jRGECO1a in the same cell type (Figure 3.11g-j), E-PGs, using + / w ; UAS-GCaMP6f (BDSC #42747) / + ; 60D05-Gal4 / UAS-jRGECO1a flies. For the *shibire*^{ts} experiments (Figure 3.14, Figure 3.15a-d), I used three Gal4 lines to drive *shibire*^{ts} in P-ENs: VT032906-Gal4 (P-EN1), VT020739-Gal4 (P-EN2), and 12D09-Gal4 (P-EN2, BDSC #48503). I used pJFRC99-20XUAS-IVS-Syn21-Shibire-ts1-p10 inserted at VK00005 (referred to here as UAS-*shibire*^{ts}) to drive *shibire*^{ts} (Rubin Lab). For each 'X-Gal4' line, I used + / w ; 60D05-LexA / LexAop-GCaMP6f ; X-Gal4 / UAS-*shibire*^{ts}, and + / w ; 60D05-LexA / LexAop-GC6aMPf ; X-Gal4 / + flies as a control. I also used + / w ; 60D05-LexA / LexAop-GCaMP6f ; + / UAS-*shibire*^{ts} flies as a control without Gal4. For P-EN stimulations (Figure 3.16, Figure 3.17), I used + / w ; 60D05-LexA / LexAop-GCaMP6f ; X-Gal4 / UAS-P2X$_2$ (Ruta Lab), where X was either VT032906 (P-EN1) or VT020739 (P-EN2). I used + / w ; 60D05-LexA / LexAop-GCaMP6f ; + / UAS-P2X$_2$ as a control without Gal4. For multicolor flip out experiments (Table 3.1, Figure 3.6g-l), I used 57C10-FLP / + ; + ; 10xUAS-FRT.stop-myr::smGdP-HA, UAS-FRT.stop-myr::smGdP-V5-THS-10xUAS-FRT.stop-myr::smGdP-FLAG / X-Gal4, where X was VT032906, VT020739 or 12D09. I used either 57C10-FLPL (BDSC #64087) or 57C10-FLPG5 (BDSC #64088) to label more or fewer neurons, respectively. To label putative axon terminals with synaptotagmin-GFP (Figure 3.6e-f), I used + / w ; + / UAS-syt-GFP (BDSC #6925) ; X-Gal4 / UAS-tdTomato (BDSC #32221) flies, where X was VT032906 or VT020739. To co-label different P-EN driver

lines, I used + / w ; 12D09-LexA (BDSC #54419) / LexAop-myrGFP (BDSC #32210) ; X-Gal4 / UAS-tdTomato, where X was VT032906 or VT020739.

Immunohistochemistry

We dissected fly brains in S2 medium at room temperature, and fixed them in 1% paraformaldehyde at 4ºC overnight. Fixed brains were washed 3 times for 30-60 min with PAT3 (0.5% Triton X-100 and 0.5% Bovine Serum Albumin in Phosphate Buffered Saline), then blocked with 3% NGS in PAT3 for 1.5 hours at room temperature. I incubated brains with primary and secondary antibodies as previously described (Nern, Pfeiffer, and Rubin 2015), and mounted them in VectaShield (Vector Labs). To analyze the neurotransmitter composition of P-ENs (Figure 3.18), Atsuko incubated separate brains with the following antibodies: anti-VGLUT (a gift from A. DiAntonio) at 1:10,000, anti-GABA (Sigma) at 1:200, anti-VGAT (a gift from D. Krantz) at 1:300, anti-ChAT (Developmental Studies Hybridoma Bank, or DSHB) at 1:100, or anti-tyrosine hydroxylase (Millipore) at 1:500. For each neurotransmitter, Atsuko co-stained with anti-GFP (Rockland) at 1:1,000 to label P-ENs driven by each Gal4 line, and nc82 antibody (DSHB) at 1:50, where possible, to label neuropil. For co-labeling tdTomato with GFP (Figure 3.6e-f, Figure 3.10), Atsuko used anti-DsRed antibody (Clontech) at 1:1,000. For the multicolor flip out experiments (Figure 3.6g-l, Table 3.1), Atsuko used antibodies as previously described (Nern, Pfeiffer, and Rubin 2015). I

imaged the central complex using a 40x 1.20NA objective on a Zeiss LSM780 confocal microscope with 0.58 or 1.0 μm separating each optical slice.

Tethered walking setup

The tethered-walking preparation was based on Seelig et al. 2010. The ball was 6.35 mm (1/4 inch) in diameter, had a mass ranging from 42 to 46 mg, and was shaped from Last-A-Foam FR-4618 (General Plastics). To shape the ball from raw foam, we (Kunal and I) machined a steel concave file with the same diameter as the ball, with sharp edges to cut the foam. The ball rested in an aluminum base with a concave hemisphere 6.75 mm (17/64 inch) in diameter. A 1 mm channel was drilled through the bottom of the hemisphere and connected to air flowing at approximately 260 mL/min.

Behavioral imaging

For all walking experiments, I imaged the fly and ball from the front under 850 nm illumination with a Prosilica GE680 camera (Allied Vision Technologies) externally triggered at 50 Hz, with a zoom lens (MLM3X-MP, Computar) set at 0.3X. For all flying experiments (Figure 2.2, Figure 2.3), I imaged the fly from below under 850 nm illumination, with a Prosilica GE680 camera triggered at 100 Hz. The lens also held an OD4 875 nm shortpass filter (Edmund Optics) to block the two-photon excitation laser (925 nm or 1035-1040 nm). The camera was

used both to position the fly and to track the ball for walking experiments, or to track the fly's wings for flying experiments.

Wing tracking

I tracked the angle of the fly's wings with respect to its body axis in real time using software developed by Andrew Straw (Maimon, Straw, and Dickinson 2010) (Figure 2.3).

Ball tracking and closed-loop experiments

I tracked the ball using FicTrac software (Moore et al. 2014). The ball was marked with irregular black spots, which allowed a single camera (see Behavioral Imaging) facing the fly to track all three rotational axes of the ball in real time at 50 Hz. Pablo verified the accuracy of the FicTrac software using a servo motor rotating a ball at known velocities. A plastic square was laser-cut with a hole at the center so that it fit as a sleeve on the ball holder, under the ball. The plastic square was aligned to the fly, such that its side edges were parallel to the fly's body axis. This plastic square was then used to calibrate the FicTrac tracking system to the fly's frame of reference (in other words, to determine which rotational axis represented forward, heading, and sideways walking). Pablo modified FicTrac to output analog voltages corresponding to the angular position of the ball along each axis through a digital to analog converter (USB-3101, Measurement Computing). In closed loop experiments, I used the heading axis

voltage output to control the azimuthal position of a bar displayed on the LED arena. That is, when the fly turned left, the bar rotated right, and vice versa, simulating the natural visual input a turning fly would experience due to a prominent, stationary, visual landmark at infinity.

LED arena and visual stimuli

We used a cylindrical LED arena (Reiser and Dickinson 2008), spanning 270º in azimuth, and 81º in height. Pixels were spaced by 1.875º. The empty quadrant of the arena was positioned directly behind the fly. I used blue LEDs (BM-10B88MD, Betlux Electronics), covered by five sheets of blue filter (Tokyo Blue, Rosco) to reduce detection of the blue LEDs by the two-photon's photomultiplier tubes. For all experiments, the microscope was surrounded by a black shroud to block light from the monitors, and all light-emitting sources inside the shroud other than the LED arena were covered with black tape. For the expanding disc stimulus (Figure 2.3), I presented a bright blue disc that expanded over 400 ms, simulating a disc approaching the fly at constant speed, until the height of the disc reached the height of the arena (the fly tended to turn in the last 100 ms of this expansion). For the bar stimulus, I presented a single bright bar, 6 pixels wide (11º) and spanning the height of the arena. The bar did not jump across the 90º gap in the arena behind the fly; rather, I kept track of the bar position behind the fly without displaying it. For the dark stimulus, all LEDs were turned off. For the moving dots stimulus (Figure 3.8), I generated a series of frames – one for

each azimuthal pixel (spaced by 1.875º) – where single-pixel (1.875º pitch) dots appear at a random location, travel for 4 pixels, and then reappear at a new random location. I chose this stimulus to separate the contributions of position and velocity of a moving object (like a bar), since here the fly cannot track the position of any single dot for more than 7.5º (4 frames). In the last 4 frames before the stimulus wraps around (ie. rotates 360º), the new pixels appear at a location that would disappear 4 frames over when the stimulus begins to wrap around. In this way, the optic flow proceeds uninterrupted for an infinite number of rotations. The total number of dots remains constant, and the same number of dots disappear (and reappear) each frame (including those not shown behind the fly). In Figure 3.8, I presented this stimulus in closed-loop, which I interrupted with 1 s open-loop rotations of the moving dots stimulus (45º and 90º to the left or right) every 6 s.

Fly tethering and preparation

Flies were anesthetized at 4ºC. Files were tethered to a custom holder that was identical to that used in previous studies (Maimon, Straw, and Dickinson 2010) for tethered flight experiments. For tethered walking experiments, the holder was the same except that the back wall was pitched to 45º instead of 90º, allowing more light to reach the objective (Figure 3.1c, the fly's wings required the space taken up by the 45º back wall to go back and forth during tethered flight). Flies were fixed to the holder by gluing the thorax and the front of the head between

the eyes with glue cured by blue light (Bondic). Additional glue was applied to the posterior side of the head in order to stabilize the head for the dissections. The head was pitched forward during tethering to provide a posterior view of the central complex. I cut a window in the cuticle immersed in saline at the centre of the posterior side of the head to gain optical and pipette access to the central complex. The holder to which each fly was tethered was placed in a base at the center of the LED arena, under the objective. The holder was stabilized by magnets in the holder and the base. The ball holder was mounted on a manipulator to adjust the position of the ball under each fly.

Calcium imaging

We used a two-photon microscope with a movable objective (Bruker) and custom stage (ThorLabs, Siskiyou). For two-photon excitation I used a Chameleon Ultra II Ti:Sapphire femtosecond pulsed laser (Coherent). For imaging GCaMP6m or GCaMP6f alone, I tuned the laser to 925nm, while for dual imaging of GCaMP6f and jRGECO1a, I used 1035-1040nm light, to excite both fluorophores simultaneously. Emitted light was split by a 575 nm dichroic mirror. I used a 490-560 nm bandpass filter (Chroma) for the green channel in single indicator experiments (Figure 3.1, Figure 3.5e-m, Figure 3.13, Figure 3.14, Figure 3.15). For dual imaging of GCaMP6f and jRGECO1a (Figure 3.9, Figure 3.11g-j, Figure 3.12) I used a 500-550nm bandpass filter for the green channel, and a 585-635nm bandpass filter for the red channel, except for dual imaging of E-PGs and

P-EN2 in the bridge (Figure 3.9b,d), where I used a 490-560nm bandpass filter for the green channel. I detected light signals with GaAsP detectors (Hamamatsu). I used a 40x 0.8 NA objective (Olympus) for imaging the brain. I perfused the brain with extracellular saline composed of, in mM: 103 NaCl, 3 KCl, 5 N-Tris(hydroxymethyl) methyl-2-aminoethanesulfonic acid (TES), 10 trehalose, 10 glucose, 2 sucrose, 26 $NaHCO_3$, 1 NaH_2PO_4, 1.5 $CaCl_2$, 4 $MgCl_2$, and bubbled with 95% O_2 / 5% CO_2. The saline had a pH of 7.3-7.4, and an osmolarity of 280±5 mOsm. The temperature of the bath was controlled by flowing the saline through a Peltier device, with feedback from a thermistor in the bath (Warner Instruments). This thermistor measurement was used to set the bath to 22ºC or 32ºC for the *shibire^{ts}* experiments. To image the protocerebral bridge, I selected a region framing the bridge, about 140 x 50 pixels in size. For Figure 2.3, I imaged a single plane, which did not sample the entire protocerebral bridge (e.g. not the medial glomeruli). For all other protocerebral bridge imaging, I scanned through 2 or 3 z-planes separated by 7-9 μm using a Piezo motor to achieve a volumetric scanning rate of 5-7 Hz. To image the ellipsoid body, I selected a region 64 x 64 pixels in size and scanned through 3 z-planes separated by 7-9 μm at 5-7 Hz.

Trial structure

For all experiments in Chapter 3, except the *shibire^{ts}* experiments, I interleaved closed-loop bar (1.0x gain) and dark screen trials. For single cell type GCaMP6m

imaging in the bridge (Figure 3.1, Figure 3.5e-m and Figure 3.13a-d), I presented each fly with six 50 s trials of each visual stimulus. For single cell type GCaMP6m imaging in the bridge and ellipsoid body (Figure 3.11a-f), I presented each fly with two 50 second trials of each visual stimulus. For dual cell type GCaMP6f and jRGECO1a imaging (Figure 3.9, Figure 3.11g-j, Figure 3.12), I presented each fly with one to two 20-30 second trials of each visual stimulus. For imaging E-PGs with P-EN-*shibire*^{ts} (Figure 3.14), I presented each fly with two 50 s trials each of closed-loop bar and a dark screen (and other stimuli not analyzed here) for each temperature. For the optic flow stimuli (Figure 3.8), I presented 16 blocks of the four stimuli (-45°/s, +45°/s, -90°/s, +90°/s open loop optic flow) to each fly. The order of the four open loop stimuli was randomized within each block. Half of the 1 s open loop stimuli were separated by 5 s of 0.5x gain closed loop optic flow, and half by 5 s of 1.0x gain closed loop optic flow. For the experiments in Chapter 4, I again interleaved dark and closed-loop bar experiments, with the first trial always dark (this was randomized in Chapter 3). In addition, the offset between the bar and the ball was randomized for each trial in order to ensure a random starting position for the bar at the start of each trial. The trial order was 30 s dark, 60 s bar, 30 s dark, 30 s bar, 30 s dark, 30 s bar for each recording. Two recordings were performed in each fly, with 32 min in the dark in between.

Data acquisition and alignment

All data were digitized at 10 kHz using a Digidata 1440 (Axon Instruments), except for the two-photon scanning images, which were acquired using PrairieView (Bruker). Behavioral, stimulus and two-photon scanning data were aligned using triggers acquired on the same Digidata 1440. For the stimulation experiments in Figure 2.2, an LED flashed onto the camera during stimulation to align the video with the stimulation time.

Comparing data acquired at different sampling rates

When comparing two-photon imaging (~5-7 Hz) and behavioral data (50 Hz) within a fly on a time-point-by-time-point basis (Figure 3.1j-l, Figure 3.5k-m, Figure 3.13c-d, Figure 3.2j-l, Figure 3.4, Figure 3.12e-f, Figure 3.15c-d), I subsampled behavioral data to the imaging frame rate by computing its mean during each volumetric imaging time point. Because different flies were imaged at slightly different frame rates depending on the size of the region of interest, when averaging across flies or across turns (Figure 3.5h-j, bottom row, Figure 3.13c,d, thick lines, Figure 3.7, Figure 3.8, Figure 3.12a-d), I linearly interpolated each time series to a common time base of 10 Hz, and then averaged over these interpolated time series.

Data analysis

Two photon images were first registered using python 2.7 (see Image registration). These images were then manually parsed in Fiji (Schindelin et al. 2012) (see Parsing imaging data). All subsequent data analysis was performed in python 2.7. I did not exclude flies from any analysis, except for the jRGECO1a experiments, where a few recordings were excluded because the red signal was too weak (0/20 flies for Figure 3.9c, 1/12 flies for Figure 3.9d, 8/22 flies for Figure 3.9k, 0/11 flies for Figure 3.9l). In analyzed jRGECO1a flies, I also sometimes excluded the second of two sets of stimuli because of jRGECO1a bleaching. If I do not exclude any data, our conclusions are unaltered. No statistical method was used to choose the sample size.

Image registration

Two-photon imaging frames were computationally registered by translating each frame in x and y to best match the time-averaged frame for each z-plane. I registered multiple recordings from the same fly to the same time-averaged template for each z-plane, unless a significant shift was introduced in between recordings. Rarely, time points were discarded from analysis if the registration failed because the signal in a particular frame was too weak. I did not register dual cell type imaging data from the ellipsoid body, but rather just analyzed the raw data directly.

Processing imaging data

Regions of interest were manually defined in Fiji (Schindelin et al. 2012). For the protocerebral bridge, I manually defined regions delineating each glomerulus from the registered time-average of each z-plane (Figure 3.1d-f, left). Note that E-PGs do not innervate the outer two glomeruli of the bridge, and P-ENs do not innervate the inner two glomeruli (Wolff, Iyer, and Rubin 2015), and thus no region was defined for these glomeruli for the respective cell type. In P-EN2 GCaMP experiments, tdTomato was expressed in E-PGs, which helped us parse glomeruli. For P-EN1 GCaMP experiments, two copies of UAS-GCaMP and VT032906-Gal4 were required to produce enough signal, and therefore tdTomato was not used for parsing glomeruli. For the ellipsoid body recordings, I first smoothed the imaging data with a 2-pixel (~ 2 μm) gaussian. I manually defined an ellipsoid body region of interest from the time-average of each z-plane. I then subdivided these regions into 16 equal wedges radiating from a manually selected center, as done previously (Seelig and Jayaraman 2015). Note that while E-PGs tile the ellipsoid body in 16 wedges, and P-ENs tile the ellipsoid body in half the number of tiles (Wolff, Iyer, and Rubin 2015), I used the same 16 wedge analysis for both as an equal means of comparing the two signals. I calculated the mean pixel value for each glomerulus or wedge across z-planes for each time point, producing a matrix of raw mean intensity values for each region over time. I then calculated $\Delta F/F$ values for each glomerulus or wedge independently, by defining F as the mean of the lower 5% of raw values in a

given glomerulus or wedge over time. I also normalized each glomerulus or wedge independently with a z-score, which measures how many standard deviations each time point is from the mean. I used this metric to estimate bridge asymmetries (Figure 3.5e-m, Figure 3.13a-d), since it tended to better normalize constant, absolute differences in intensity across glomeruli, which may arise due to differences in the number of cells per glomerulus targeted by each Gal4 line, or the amount of GCaMP in each cell. I observed the same asymmetries in the bridge using ΔF/F, but with more variability (Figure 3.7).

Analysis of periodicity and phase

To analyze the protocerebral bridge signal, I started with a matrix of ΔF/F values, where each row represents a time point, and each column represents a glomerulus. I took the Fourier transform of each row, or time point, independently, and observed a consistent peak at a periodicity of ~8 glomeruli for each cell type (the peak periodicity of the power spectrum averaged over time is shown in Figure 3.2g-i for closed-loop bar and Figure 3.3g-i for dark conditions). Given that this periodicity was relatively constant over time (Figure 3.2a-f, Figure 3.3a-f), I extracted the phase from the Fourier component with a period of 8 glomeruli for each time point independently. When overlaid on the protocerebral bridge GCaMP time series, this phase accurately tracks the shift in the protocerebral bridge over time (Figure 3.2a-f, Figure 3.3a-f). For the ellipsoid body, I computed the population vector average, as previously described (Seelig

and Jayaraman 2015). For summary analyses, and for the dual-imaging sample traces (Figure 3.9a-b, i-j), the phase was filtered with a 3-point moving average. To calculate the offset between the phase and bar position (Figure 3.2j-l), I computed the circular mean of the difference between the phase and bar position during time points when the bar was visible to the fly. I shifted the phase by this constant offset in Figure 3.1g-i, Figure 3.2b,d,f, and Figure 3.15a-b. In Figure 3.5e-g, Figure 3.13a-b, I nulled the accumulated phase and ball position at time zero, and applied a gain to the ball heading to best match the phase: 1.0 for Figure 3.5e (P-EN1), 1.40 for Figure 3.5f (P-EN2) and 0.75 for Figure 3.5g (E-PG), 1.0 for Figure 3.13a (P-EN1), 0.89 for Figure 3.13b (P-EN2). I interpret these different gains measured in different flies to be the result of experimental variability rather than the three cell types operating under different gains. Indeed, when I imaged E-PGs and P-ENs simultaneously in the same fly (Figure 3.9), their peaks moved in unison (ie. with the same gain) along the bridge and ellipsoid body.

Correlation analysis

For closed-loop bar experiments, I computed the circular correlation (Fisher and Lee 1983) between GCaMP phase and bar position (Figure 3.1j-l, “position”). For experiments in the dark, I computed the Pearson correlation between GCaMP phase velocity and ball velocity (Figure 3.1j-l, “velocity”, Figure 3.14c-d). I correlated velocities instead of position for dark screen data since the phase

tended to drift away from the ball's heading without a visual landmark. I calculated these correlations for different time lags between the phase and ball signals, and in each figure I report the correlation at the time lag where the correlation was highest. Specifically, the phase was delayed by 300 ms relative to the ball for E-PG and P-EN2 neurons in Figure 3.1j,l, and by 600 ms for P-EN1 neurons in Figure 3.1k. The sign of these delays suggests that the heading system updates in response to the fly turning, not vice versa, although more experiments are needed (see Supplemental Discussion). The longer delay for P-EN1 compared to P-EN2 and E-PG was likely an artifact of over-expressing GCaMP6m in P-EN1 rather than reflecting a genuine biological difference among cell types (see Discussion). For example, in other imaging experiments where I measured P-EN1 activity side-by-side with E-PG activity, I observed that the P-EN1 peak actually leads the E-PG peak (Figure 3.9m,o). In Figure 3.14c-d, the time lag where the correlation was highest between E-PG GCaMP phase- and ball-velocity was 200 ms (rather than 300 ms), which was the time lag used for the correlation values reported in this figure; this shorter delay was likely due to the fact that in Figure 3.1 I used GCaMP6m, and in Figure 3.14c-d I used GCaMP6f. For the P-EN>*shibire*^{ts} experiments (Figure 3.14), I computed the difference between the velocity correlations at 22ºC and 32ºC for each fly. I then used a two-sided Wilcoxon rank-sum test to reject the null hypothesis that this difference was the same in each of the three P-EN-Gal4, UAS-*shibire*^{ts} fly populations and in the respective P-EN-Gal4- or UAS-*shibire*^{ts}-only populations

($p<0.01$ for all individual comparisons). For all phase correlations, I only included data where the fly was walking with a speed of at least 1 mm/s. I also required the peak activity (the mean of the top two values in the bridge) to be greater than 0.8 ΔF/F, to ensure the phase was properly estimated.

Computing the bridge asymmetry or total activity as a function of turning velocity or speed

For each time point, I subtracted the mean z-score normalized signal in the left bridge from that in the right bridge (referred to as the *bridge asymmetry*). I binned these bridge asymmetries based on the turning velocity of the fly in 30°/s bins, and computed the mean asymmetry in each bin (Figure 3.5k-m). I repeated this process for different time lags between the bridge asymmetry and the fly's turning behavior, to find the lag at which the slope (measured between -200°/s and +200°/s) was the steepest. The curve computed at this time lag (bridge asymmetry lagging by +400 ms with respect to behavior for P-EN1 and P-EN2) is shown in Figure 3.5k,l. (Many other lags, before and after +400 ms, also show a significant positive slope for P-EN1 and P-EN2.) The time lag chosen does not affect the E-PG curve, whose slope is always near zero. The same approach was taken to plot the bridge asymmetry vs. speed, as well as total bridge activity vs. turning velocity and speed in **Figure 3.20**.

Culling individual turns or phase shifts

To isolate individual turns (Figure 3.5h-j) or phase shifts in the bridge (Figure 3.13c,), I detected peaks in the turning velocity or phase velocity signal, respectively. In both cases, I first smoothed the velocity signal by convolving it with a gaussian (300 ms s.d.). From this smoothed velocity signal, I isolated peaks with a minimum peak height of 30°/s and a minimum peak width of 0.5 s for the turns and the phase shifts. I further required that each peak be isolated from other peaks with a minimum distance of 1.5 s. I aligned the turning velocity or phase velocity and bridge asymmetry signals to the start of each turn or phase shift.

Phase nulling

To compute the average GCaMP signal in the bridge or ellipsoid body independent of phase (Figure 3.9c-d, k-p), I computationally shifted the GCaMP signals at each time point so that the phase was the same across all time points. To achieve this phase nulling, I first interpolated the GCaMP signal at each time point to 1/10 of a glomerulus or wedge with a cubic spline. I then shifted this interpolated signal by the phase estimate at that time point. In the ellipsoid body, this shift is naturally circular. In the protocerebral bridge, I wrapped the signal around the same side of the bridge, such that values shifted past the left edge of the left bridge would return on the right edge of the left bridge, and so on, in order to preserve left and right asymmetries. This was possible since each side of the

bridge innervated by a given cell type consisted of 8 glomeruli, which matched the period of the signals. Once I nulled the phase, I computed the mean signal over time when the fly was walking straight (Figure 3.9c-d,k-l, computed for 0°/s ±30°/s). For the ellipsoid body, I also averaged the phase-nulled signal over times when the fly turned at 300°/s ±30°/s to the left (negative) or right (positive). In Figure 3.9k-p, I show these phase nulled plots at the time lag where the P-EN1 or P-EN2 ellipsoid body asymmetry (see below) and the fly's turning velocity showed a maximum correlation (Figure 3.12e-f, black arrows). In Figure 3.9 I nulled both the P-EN and E-PG signals using the E-PG phase. In Figure 3.11a-f, I nulled both the bridge and ellipsoid body signals using the ellipsoid body phase. In Figure 3.11g-j, I nulled both the GCaMP6f and jRGECO1a signals using the GCaMP6f phase (analogous to Figure 3.9). In Figure 3.16h-i, and Figure 3.17, I nulled both the GCaMP6f and Alexa594 signals using the position of the pipette.

Computing the ellipsoid body asymmetry in P-ENs

To compute the *ellipsoid body asymmetry* in P-ENs (Figure 3.12c-f), I integrated the P-EN signal 180° clockwise and counter-clockwise from the E-PG phase, and subtracted the integrated counter-clockwise (left on the linearized plots) signal from the integrated clockwise (right on the linearized plots) signal. I used a two-sided Wilcoxon rank-sum test to reject the null hypothesis that the ellipsoid body asymmetry in P-ENs was the same when the fly was turning to the left at –300˚/s (Figure 3.9m-n) vs. walking straight (Figure 3.9k-l), and turning to the right at

+300˚/s (Figure 3.9o-p) vs. walking straight (Figure 3.9k-l). All p values were < 0.02 when analyzing either z-score normalized data (not shown) or ΔF/F normalized data (shown in Figure 3.9k-p). The null hypothesis that the ellipsoid body asymmetry in P-ENs was the same when the fly turned left (Figure 3.9m-n) vs. turned right (Figure 3.9o-p) was rejected for both P-EN1 and P-EN2 ($p<0.01$), using a two-sided Wilcoxon rank-sum test with either z-score or ΔF/F normalized data.

P-EN stimulation

To stimulate one-side of the bridge in Figure 2.2, I expressed mCD8-GFP (to localize the bridge) and the ATP-gated cation channel $P2X_2$ driven by NP0212-Gal4. I dissolved Na_2ATP (A7699, Sigma) in extracellular saline at 10 mM. This ATP solution was loaded into a pipette and released onto one side of the bridge with brief (50 ms – 200 ms) pressure pulses in the pipette using a Pneumatic PicoPump (PV820, World Precision Instruments).

To measure the effect of stimulating P-ENs on E-PGs, I expressed GCaMP6f in E-PGs and the ATP-gated cation channel $P2X_2$ in either P-EN1 or P-EN2 cells (see Fly Stocks). Na_2ATP (A7699, Sigma) was dissolved in extracellular solution (see Calcium imaging) at 1mM, and stored in aliquots at -80^{o}C. Working solutions of 0.5 mM ATP for VT032906-Gal4 or 0.1 mM ATP for VT020739-Gal4, with 20 μM Alexa594 were prepared the same day as the experiment, and loaded into a pipette with a bore <1 μm in diameter. I adjusted the concentration of ATP to

provide as gentle a perturbation as possible, as measured by the E-PG signal shapes remaining the same, and the E-PG phase returning to following the fly's' movements a few seconds after the stimulation. 0.5 mM ATP was used for the controls without Gal4. The pressure in the pipette was controlled using a Pneumatic PicoPump (PV820, World Precision Instruments), and the pressure recorded using a Pressure Monitor (PM 015R, World Precision Instruments). I applied pressure pulses ranging from 5-20 psi with a 20 ms duration. The pipette was controlled using a PatchStar micro manipulator (Scientifica). To access the bridge, I locally applied 0.5 mg/mL collagenase type 4 (Worthington) through a pipette, while keeping the bath at ~30ºC, to breach the sheath above the bridge. For dual imaging of GCaMP6f and Alexa594, I used a 500-550nm bandpass filter for the green channel, and a 585-635nm bandpass filter for the red channel. I computed $\Delta F/F$ values for Alexa594 by defining the baseline, F_0, as the mean of the lowest 5% of values in the entire bridge, rather than independently for each glomerulus, since the glomerulus-independent normalization is meant to compensate for varying GCaMP baselines across glomeruli, presumably due to varying levels of GCaMP expression, or the amount of innervation within each glomerulus. In Figure 3.16h-i and Figure 3.17, both channels were nulled using the position of the pipette, which differed from fly to fly. In Figure 3.16h-i, I averaged the E-PG signal 0.7-1.0 s after stimulation, and the Alexa594 (ATP) signal during the first frame after stimulation. In Figure 3.17, I computed the change in each phase-nulled signal by subtracting the average over 0.3 s before

stimulation from the averages in Figure 3.16h-i for each channel. The examples in Figure 3.16d-g highlight events where I stimulated P-ENs at the glomerulus where I expected P-EN1 or P-EN2 peak activity immediately prior to stimulation based on the measured E-PG phase (see Figure 3.9). All stimulations are included in the phase-nulled averages in Figure 3.16h-i. All stimulation experiments were performed in the dark.

References

Aksay, E, G Gamkrelidze, H S Seung, R Baker, and D W Tank. 2001. “In Vivo Intracellular Recording and Perturbation of Persistent Activity in a Neural Integrator..” *Nature Neuroscience* 4 (2): 184–93. doi:10.1038/84023.

Aronov, Dmitriy, Rhino Nevers, and David W Tank. 2017. “Mapping of a Non-Spatial Dimension by the Hippocampal–Entorhinal Circuit.” *Nature* 543 (7647). Nature Publishing Group: 719–22. doi:10.1038/nature21692.

Berg, H C, and D A Brown. 1972. “Chemotaxis in Escherichia Coli Analysed by Three-Dimensional Tracking..” *Nature* 239 (5374): 500–504.

Blair, Hugh T, Jeiwon Cho, and Patricia E Sharp. 1998. “Role of the Lateral Mammillary Nucleus in the Rat Head Direction Circuit.” *Neuron* 21 (6): 1387–97. doi:10.1016/S0896-6273(00)80657-1.

Block, Steven M, Jeffrey E Segall, and Howard C Berg. 1982. “Impulse Responses in Bacterial Chemotaxis.” *Cell* 31 (1): 215–26. doi:10.1016/0092-8674(82)90421-4.

Boccara, Charlotte N, Francesca Sargolini, Veslemøy Hult Thoresen, Trygve Solstad, Menno P Witter, Edvard I Moser, and May-Britt Moser. 2010. “Grid Cells in Pre- and Parasubiculum.” *Nature Neuroscience* 13 (8). Nature Publishing Group: 987–94. doi:10.1038/nn.2602.

Bostock, E, R U Muller, and J L Kubie. 1991. “Experience-Dependent Modifications of Hippocampal Place Cell Firing..” *Hippocampus* 1 (2). Wiley Subscription Services, Inc., A Wiley Company: 193–205. doi:10.1002/hipo.450010207.

Chen, Tsai-Wen, Trevor J Wardill, Yi Sun, Stefan R Pulver, Sabine L Renninger, Amy Baohan, Eric R Schreiter, et al. 2013. “Ultrasensitive Fluorescent Proteins for Imaging Neuronal Activity.” *Nature* 499 (7458): 295–300. doi:10.1038/nature12354.

Corlew, Rebekah, Daniel J Brasier, Daniel E Feldman, and Benjamin D Philpot. 2008. “Presynaptic NMDA Receptors: Newly Appreciated Roles in Cortical Synaptic Function and Plasticity.” *The Neuroscientist* 14 (6). SAGE PublicationsSage CA: Los Angeles, CA: 609–25. doi:10.1177/1073858408322675.

Dana, Hod, Boaz Mohar, Yi Sun, Sujatha Narayan, Andrew Gordus, Jeremy P Hasseman, Getahun Tsegaye, et al. 2016. “Sensitive Red Protein Calcium Indicators for Imaging Neural Activity..” *eLife* 5 (March): 413. doi:10.7554/eLife.12727.

Egevang, Carsten, Iain J Stenhouse, Richard A Phillips, Aevar Petersen, James W Fox, and Janet R D Silk. 2010. “Tracking of Arctic Terns Sterna Paradisaea Reveals Longest Animal Migration..” *Proceedings of the National Academy of Sciences of the United States of America* 107 (5). National Acad Sciences: 2078–81. doi:10.1073/pnas.0909493107.

Eichenbaum, Howard, and Neal J Cohen. 2014. “Can We Reconcile the Declarative Memory and Spatial Navigation Views on Hippocampal Function?.” *Neuron* 83 (4): 764–70. doi:10.1016/j.neuron.2014.07.032.
Finkelstein, Arseny, Dori Derdikman, Alon Rubin, Jakob N Foerster, Liora Las, and Nachum Ulanovsky. 2015. “Three-Dimensional Head-Direction Coding in the Bat Brain.” *Nature* 517 (7533). Nature Research: 159–64. doi:10.1038/nature14031.
Fisher, N I, and A J Lee. 1983. “A Correlation Coefficient for Circular Data.” *Biometrika* 70 (2). Oxford University Press: 327–32. doi:10.1093/biomet/70.2.327.
Flood, Thomas F, Michael Gorczyca, Benjamin H White, Kei Ito, and Motojiro Yoshihara. 2013. “A Large-Scale Behavioral Screen to Identify Neurons Controlling Motor Programs in the Drosophila Brain..” *G3 (Bethesda, Md.)* 3 (10). G3: Genes, Genomes, Genetics: 1629–37. doi:10.1534/g3.113.006205.
von Frisch, Karl. 1967. *The Dance Language and Orientation of Bees.* Harvard University Press.
Fuxjager, Matthew J, Brian S Eastwood, and Kenneth J Lohmann. 2011. “Orientation of Hatchling Loggerhead Sea Turtles to Regional Magnetic Fields Along a Transoceanic Migratory Pathway.” *The Journal of Experimental Biology* 214 (15). The Company of Biologists Ltd: 2504–8. doi:10.1242/jeb.055921.
Fyhn, Marianne, Sturla Molden, Menno P Witter, Edvard I Moser, and May-Britt Moser. 2004. “Spatial Representation in the Entorhinal Cortex..” *Science* 305 (5688). American Association for the Advancement of Science: 1258–64. doi:10.1126/science.1099901.
Fyhn, Marianne, Torkel Hafting, Alessandro Treves, May-Britt Moser, and Edvard I Moser. 2007. “Hippocampal Remapping and Grid Realignment in Entorhinal Cortex..” *Nature* 446 (7132): 190–94. doi:10.1038/nature05601.
Goodridge, Jeremy P, and Jeffrey S Taube. 1997. “Interaction Between the Postsubiculum and Anterior Thalamus in the Generation of Head Direction Cell Activity.” *The Journal of Neuroscience* 17 (23). Society for Neuroscience: 9315–30.
Hafting, Torkel, Marianne Fyhn, Sturla Molden, May-Britt Moser, and Edvard I Moser. 2005. “Microstructure of a Spatial Map in the Entorhinal Cortex..” *Nature* 436 (7052): 801–6. doi:10.1038/nature03721.
Hargreaves, Eric L, Geeta Rao, Inah Lee, and James J Knierim. 2005. “Major Dissociation Between Medial and Lateral Entorhinal Input to Dorsal Hippocampus..” *Science* 308 (5729). American Association for the Advancement of Science: 1792–94. doi:10.1126/science.1110449.
Hayashi, Shigeo, Kei Ito, Yukiko Sado, Misako Taniguchi, Ai Akimoto, Hiroko Takeuchi, Toshiro Aigaki, et al. 2002. “GETDB, a Database Compiling Expression Patterns and Molecular Locations of a Collection of Gal4 Enhancer Traps.” *Genesis* 34 (1-2): 58–61. doi:10.1002/gene.10137.
Heinze, S, and U Homberg. 2007. “Maplike Representation of Celestial E-Vector

Orientations in the Brain of an Insect." *Science* 315 (5814): 995–97. doi:10.1126/science.1135531.
Homberg, U, S Heinze, K Pfeiffer, M Kinoshita, and B el Jundi. 2011. "Central Neural Coding of Sky Polarization in Insects." *Philosophical Transactions of the Royal Society B: Biological Sciences* 366 (1565). Wiley Subscription Services, Inc., A Wiley Company: 680–87. doi:10.1002/cne.21842.
Homberg, Uwe. 2004. "In Search of the Sky Compass in the Insect Brain." *Naturwissenschaften* 91 (5). Springer-Verlag: 199–208. doi:10.1007/s00114-004-0525-9.
Homberg, Uwe. 2008. "Evolution of the Central Complex in the Arthropod Brain with Respect to the Visual System." *Arthropod Structure & Development* 37 (5): 347–62. doi:10.1016/j.asd.2008.01.008.
Kong, Eric C, Katherine Woo, Haiyan Li, Tim Lebestky, Nasima Mayer, Melissa R Sniffen, Ulrike Heberlein, Roland J Bainton, Jay Hirsh, and Fred W Wolf. 2010. "A Pair of Dopamine Neurons Target the D1-Like Dopamine Receptor DopR in the Central Complex to Promote Ethanol-Stimulated Locomotion in Drosophila." *PLoS ONE* 5 (4): e9954. doi:10.1371/journal.pone.0009954.s009.
Kuntz, Sara, Burkhard Poeck, and Roland Strauss. 2017. "Visual Working Memory Requires Permissive and Instructive NO/cGMP Signaling at Presynapses in the Drosophila Central Brain." *Current Biology*, February. doi:10.1016/j.cub.2016.12.056.
Lavenex, P, and D G Amaral. 2000. "Hippocampal-Neocortical Interaction: a Hierarchy of Associativity.." *Hippocampus* 10 (4). John Wiley & Sons, Inc.: 420–30. doi:10.1002/1098-1063(2000)10:4<420::AID-HIPO8>3.0.CO;2-5.
Leutgeb, Stefan, Jill K Leutgeb, Carol A Barnes, Edvard I Moser, Bruce L McNaughton, and May-Britt Moser. 2005. "Independent Codes for Spatial and Episodic Memory in Hippocampal Neuronal Ensembles.." *Science* 309 (5734). American Association for the Advancement of Science: 619–23. doi:10.1126/science.1114037.
Lin, Chih-Yung, Chao-Chun Chuang, Tzu-En Hua, Chun-Chao Chen, Barry J Dickson, Ralph J Greenspan, and Ann-Shyn Chiang. 2013. "A Comprehensive Wiring Diagram of the Protocerebral Bridge for Visual Information Processing in the Drosophila Brain.." *Cell Reports* 3 (5): 1739–53. doi:10.1016/j.celrep.2013.04.022.
Maimon, Gaby, Andrew D Straw, and Michael H Dickinson. 2010. "Active Flight Increases the Gain of Visual Motion Processing in Drosophila.." *Nature Neuroscience* 13 (3): 393–99. doi:10.1038/nn.2492.
Major, Guy, and David Tank. 2004. "Persistent Neural Activity: Prevalence and Mechanisms." *Current Opinion in Neurobiology* 14 (6): 675–84. doi:10.1016/j.conb.2004.10.017.
Malenka, R C, J A Kauer, D J Perkel, and R A Nicoll. 1989. "The Impact of Postsynaptic Calcium on Synaptic Transmission — Its Role in Long-Term Potentiation." *Trends in Neurosciences* 12 (11): 444–50. doi:10.1016/0166-

2236(89)90094-5.
McNaughton, B L, and L Chen. 1991. "'Dead Reckoning,' Landmark Learning, and the Sense of Direction: a Neurophysiological and Computational Hypothesis." *Neuroscience*.
McNaughton, Bruce L, Francesco P Battaglia, Ole Jensen, Edvard I Moser, and May-Britt Moser. 2006. "Path Integration and the Neural Basis of the 'Cognitive Map'.." *Nature Reviews Neuroscience* 7 (8): 663–78. doi:10.1038/nrn1932.
Mizumori, S J, and J D Williams. 1993. "Directionally Selective Mnemonic Properties of Neurons in the Lateral Dorsal Nucleus of the Thalamus of Rats." *The Journal of Neuroscience* 13 (9). Society for Neuroscience: 4015–28.
Moore, Richard J D, Gavin J Taylor, Angelique C Paulk, Thomas Pearson, Bruno van Swinderen, and Mandyam V Srinivasan. 2014. "FicTrac: a Visual Method for Tracking Spherical Motion and Generating Fictive Animal Paths." *Journal of Neuroscience Methods* 225. Elsevier B.V.: 106–19. doi:10.1016/j.jneumeth.2014.01.010.
Moser, May-Britt, David C Rowland, and Edvard I Moser. 2015. "Place Cells, Grid Cells, and Memory." *Cold Spring Harbor Perspectives in Biology* 7 (2). Cold Spring Harbor Lab: a021808. doi:10.1101/cshperspect.a021808.
Mouritsen, Henrik, Rachael Derbyshire, Julia Stalleicken, Ole Ø Mouritsen, Barrie J Frost, and D Ryan Norris. 2013. "An Experimental Displacement and Over 50 Years of Tag-Recoveries Show That Monarch Butterflies Are Not True Navigators." *Proceedings of the National Academy of Sciences of the United States of America* 110 (18). National Acad Sciences: 7348–53. doi:10.1073/pnas.1221701110.
Muir, Gary M, Joel E Brown, John P Carey, Timo P Hirvonen, Charles C Della Santina, Lloyd B Minor, and Jeffrey S Taube. 2009. "Disruption of the Head Direction Cell Signal After Occlusion of the Semicircular Canals in the Freely Moving Chinchilla.." *The Journal of Neuroscience* 29 (46): 14521–33. doi:10.1523/JNEUROSCI.3450-09.2009.
Muller, R U, and J L Kubie. 1987. "The Effects of Changes in the Environment on the Spatial Firing of Hippocampal Complex-Spike Cells." *The Journal of Neuroscience* 7 (7). Society for Neuroscience: 1951–68.
Nern, Aljoscha, Barret D Pfeiffer, and Gerald M Rubin. 2015. "Optimized Tools for Multicolor Stochastic Labeling Reveal Diverse Stereotyped Cell Arrangements in the Fly Visual System.." *Proceedings of the National Academy of Sciences of the United States of America* 112 (22). National Acad Sciences: E2967–76. doi:10.1073/pnas.1506763112.
Neuser, Kirsa, Tilman Triphan, Markus Mronz, Burkhard Poeck, and Roland Strauss. 2008. "Analysis of a Spatial Orientation Memory in Drosophila." *Nature* 453 (7199): 1244–47. doi:10.1038/nature07003.
Newsome, W T, and E B Pare. 1988. "A Selective Impairment of Motion Perception Following Lesions of the Middle Temporal Visual Area (MT)."

Journal of Neuroscience.
O'Keefe, J, and J Dostrovsky. 1971. “The Hippocampus as a Spatial Map. Preliminary Evidence From Unit Activity in the Freely-Moving Rat.” *Brain Research* 34 (1): 171–75. doi:10.1016/0006-8993(71)90358-1.
Ofstad, Tyler A, Charles S Zuker, and Michael B Reiser. 2011. “Visual Place Learning in Drosophila Melanogaster..” *Nature* 474 (7350): 204–7. doi:10.1038/nature10131.
Oh, Seung Wook, Julie A Harris, Lydia Ng, Brent Winslow, Nicholas Cain, Stefan Mihalas, Quanxin Wang, et al. 2014. “A Mesoscale Connectome of the Mouse Brain.” *Nature* 508 (7495). Nature Publishing Group: 207–14. doi:10.1038/nature13186.
Paoletti, Pierre, Camilla Bellone, and Qiang Zhou. 2013. “NMDA Receptor Subunit Diversity: Impact on Receptor Properties, Synaptic Plasticity and Disease.” *Nature* 14 (6). Nature Research: 383–400. doi:10.1038/nrn3504.
Pastor, A M, R R De la Cruz, and R Baker. 1994. “Eye Position and Eye Velocity Integrators Reside in Separate Brainstem Nuclei..” *Proceedings of the National Academy of Sciences of the United States of America* 91 (2): 807–11. doi:10.1073/pnas.91.2.807.
Poodry, Clifton A, and Lois Edgar. 1979. “Reversible Alteration in the Neuromuscular Junctions of Drosophila Melanogaster Bearing a Temperature-Sensitive Mutation, Shibire..” *The Journal of Cell Biology* 81 (3). Rockefeller Univ Press: 520–27.
Ranck, J B, Jr. 1984. *Head Direction Cells in the Deep Cell Layer of Dorsal Presubiculum in Freely Moving Rats*. Soc Neurosci Abstr.
Redish, A David, Adam N Elga, and David S Touretzky. 1996. “A Coupled Attractor Model of the Rodent Head Direction System.” *Network: Computation in Neural Systems* 7 (4). Taylor & Francis: 671–85. doi:10.1088/0954-898X_7_4_004.
Reiser, Michael B, and Michael H Dickinson. 2008. “A Modular Display System for Insect Behavioral Neuroscience.” *Journal of Neuroscience Methods* 167 (2): 127–39. doi:10.1016/j.jneumeth.2007.07.019.
Reppert, Steven M, Robert J Gegear, and Christine Merlin. 2010. “Navigational Mechanisms of Migrating Monarch Butterflies.” *Trends in Neurosciences* 33 (9). Elsevier Ltd: 399–406. doi:10.1016/j.tins.2010.04.004.
Robinson, D A. 1989. “Integrating with Neurons..” *Annual Review of Neuroscience* 12 (1): 33–45. doi:10.1146/annurev.ne.12.030189.000341.
Rossel, S, and R Wehner. 1982. “The Bee's Map of the E-Vector Pattern in the Sky..” *Proceedings of the National Academy of Sciences of the United States of America* 79 (14): 4451–55.
Rowland, D C, Y Roudi, and M B Moser. 2016. “Ten Years of Grid Cells.” *Annual Review of …*. doi:10.1146/annurev-neuro-070815-013824.
Ruta, Vanessa, Sandeep Robert Datta, Maria Luisa Vasconcelos, Jessica Freeland, Loren L Looger, and Richard Axel. 2010. “A Dimorphic Pheromone Circuit in Drosophila From Sensory Input to Descending Output.” *Nature* 468

(7324): 686–90. doi:10.1038/nature09554.
Sargolini, Francesca, Marianne Fyhn, Torkel Hafting, Bruce L McNaughton, Menno P Witter, May-Britt Moser, and Edvard I Moser. 2006. “Conjunctive Representation of Position, Direction, and Velocity in Entorhinal Cortex..” *Science* 312 (5774). American Association for the Advancement of Science: 758–62. doi:10.1126/science.1125572.
Schindelin, Johannes, Ignacio Arganda-Carreras, Erwin Frise, Verena Kaynig, Mark Longair, Tobias Pietzsch, Stephan Preibisch, et al. 2012. “Fiji: an Open-Source Platform for Biological-Image Analysis..” *Nature Methods* 9 (7): 676–82. doi:10.1038/nmeth.2019.
Seelig, Johannes D, and Vivek Jayaraman. 2013. “Feature Detection and Orientation Tuning in the Drosophila Central Complex..” *Nature* 503 (7475): 262–66. doi:10.1038/nature12601.
Seelig, Johannes D, and Vivek Jayaraman. 2015. “Neural Dynamics for Landmark Orientation and Angular Path Integration.” *Nature* 521 (7551): 186–91. doi:10.1038/nature14446.
Seelig, Johannes D, M Eugenia Chiappe, Gus K Lott, Anirban Dutta, Jason E Osborne, Michael B Reiser, and Vivek Jayaraman. 2010. “Two-Photon Calcium Imaging From Head-Fixed Drosophila During Optomotor Walking Behavior.” *Nature Methods* 7 (7): 535–40. doi:10.1038/nmeth.1468.
Sharp, P E, H T Blair, and M Brown. 1996. “Neural Network Modeling of the Hippocampal Formation Spatial Signals and Their Possible Role in Navigation: a Modular Approach..” *Hippocampus* 6 (6): 720–34. doi:10.1002/(SICI)1098-1063(1996)6:6<720::AID-HIPO14>3.0.CO;2-2.
Skaggs, W E, J J Knierim, H S Kudrimoti, and B L McNaughton. 1995. “A Model of the Neural Basis of the Rat's Sense of Direction..” *Advances in Neural Information Processing Systems* 7: 173–80.
Solstad, Trygve, Charlotte N Boccara, Emilio Kropff, May-Britt Moser, and Edvard I Moser. 2008. “Representation of Geometric Borders in the Entorhinal Cortex..” *Science* 322 (5909). American Association for the Advancement of Science: 1865–68. doi:10.1126/science.1166466.
Squire, Larry R, Craig E L Stark, and Robert E Clark. 2004. “The Medial Temporal Lobe..” *Annual Review of Neuroscience* 27: 279–306. doi:10.1146/annurev.neuro.27.070203.144130.
Stackman, R W, and J S Taube. 1998. “Firing Properties of Rat Lateral Mammillary Single Units: Head Direction, Head Pitch, and Angular Head Velocity..” *The Journal of Neuroscience* 18 (21): 9020–37.
Stackman, Robert W, and Jeffrey S Taube. 1997. “Firing Properties of Head Direction Cells in the Rat Anterior Thalamic Nucleus: Dependence on Vestibular Input.” *The Journal of Neuroscience* 17 (11). Society for Neuroscience: 4349–58. doi:10.1016/0014-4886(77)90012-7.
Stensola, Hanne, Tor Stensola, Trygve Solstad, Kristian Frøland, May-Britt Moser, and Edvard I Moser. 2012. “The Entorhinal Grid Map Is Discretized..” *Nature* 492 (7427): 72–78. doi:10.1038/nature11649.

Strauss, R, and J Pichler. 1998. “Persistence of Orientation Toward a Temporarily Invisible Landmark in Drosophila Melanogaster..” *Journal of Comparative Physiology a: Sensory, Neural, and Behavioral Physiology* 182 (4): 411–23.

Swaney, Kristen F, Chuan-Hsiang Huang, and Peter N Devreotes. 2010. “Eukaryotic Chemotaxis: a Network of Signaling Pathways Controls Motility, Directional Sensing, and Polarity.” *Dx.Doi.org* 39 (1). Annual Reviews: 265–89. doi:10.1146/annurev.biophys.093008.131228.

Taube, J S, R U Muller, and J B Ranck. 1990a. “Head-Direction Cells Recorded From the Postsubiculum in Freely Moving Rats. I. Description and Quantitative Analysis..” *The Journal of Neuroscience* 10 (2): 420–35.

Taube, J S, R U Muller, and J B Ranck. 1990b. “Head-Direction Cells Recorded From the Postsubiculum in Freely Moving Rats. II. Effects of Environmental Manipulations..” *The Journal of Neuroscience* 10 (2). Society for Neuroscience: 436–47.

Taube, Jeffrey S. 2007. “The Head Direction Signal: Origins and Sensory-Motor Integration..” *Annual Review of Neuroscience* 30 (1): 181–207. doi:10.1146/annurev.neuro.29.051605.112854.

Tolman, Edward C, B F Ritchie, and D Kalish. 1946. “Studies in Spatial Learning. II. Place Learning Versus Response Learning..” *Journal of Experimental Psychology: General*.

Varga, Adrienn G, and Roy E Ritzmann. 2016. “Cellular Basis of Head Direction and Contextual Cues in the Insect Brain.” *Current Biology* 26 (14): 1816–28. doi:10.1016/j.cub.2016.05.037.

Wehner, R, and M Srinivasan. 2003. *The Neurobiology of Spatial Behaviour, Chapter Path Integration in Insects*.

Wehner, Rüdiger. 1989. “Neurobiology of Polarization Vision.” *Trends in Neurosciences* 12 (9): 353–59. doi:10.1016/0166-2236(89)90043-X.

Witter, M P, H J Groenewegen, F H Lopes da Silva, and A H Lohman. 1989. “Functional Organization of the Extrinsic and Intrinsic Circuitry of the Parahippocampal Region..” *Progress in Neurobiology* 33 (3): 161–253.

Wolff, Tanya, Nirmala A Iyer, and Gerald M Rubin. 2015. “Neuroarchitecture and Neuroanatomy of the Drosophila Central Complex: a GAL4-Based Dissection of Protocerebral Bridge Neurons and Circuits.” *The Journal of Comparative Neurology* 523 (7): 997–1037. doi:10.1002/cne.23705.

Wu, Chia-Lin, Shouzhen Xia, Tsai-Feng Fu, Huaien Wang, Ying-Hsiu Chen, Daniel Leong, Ann-Shyn Chiang, and Tim Tully. 2007. “Specific Requirement of NMDA Receptors for Long-Term Memory Consolidation in Drosophila Ellipsoid Body..” *Nature Neuroscience* 10 (12): 1578–86. doi:10.1038/nn2005.

Zemelman, Boris V, Nasri Nesnas, Georgia A Lee, and Gero MiesenbOck. 2003. “Photochemical Gating of Heterologous Ion Channels: Remote Control Over Genetically Designated Populations of Neurons..” *Proceedings of the National Academy of Sciences of the United States of America* 100 (3).

National Acad Sciences: 1352–57. doi:10.1073/pnas.242738899.
Zhang, K. 1996. “Representation of Spatial Orientation by the Intrinsic Dynamics of the Head-Direction Cell Ensemble: a Theory..” *The Journal of Neuroscience* 16 (6): 2112–26.
Zhang, Zhiping, Xiaoting Li, Jing Guo, Yan Li, and Aike Guo. 2013. “Two Clusters of GABAergic Ellipsoid Body Neurons Modulate Olfactory Labile Memory in Drosophila..” *The Journal of Neuroscience* 33 (12). Society for Neuroscience: 5175–81. doi:10.1523/JNEUROSCI.5365-12.2013.